Thermal properties of hot and dense matter with finite range interactions

Constantinos Constantinou,[1,*] Brian Muccioli,[2,†] Madappa Prakash,[2,‡] and James M. Lattimer[3,§]
[1]*Institute for Advanced Simulation, Institut für Kernphysik, and Jülich Center for Hadron Physics, Forschungszentrum Jülich, D-52425 Jülich, Germany*
[2]*Department of Physics and Astronomy, Ohio University, Athens, Ohio 45701, USA*
[3]*Department of Physics and Astronomy, Stony Brook University, Stony Brook, New York 11794-3800, USA*
(Received 15 April 2015; revised manuscript received 10 July 2015; published 5 August 2015)

We explore the thermal properties of hot and dense matter using a model that reproduces the empirical properties of isospin symmetric and asymmetric bulk nuclear matter, optical-model fits to nucleon-nucleus scattering data, heavy-ion flow data in the energy range 0.5–2 GeV/A, and the largest well-measured neutron star mass of $2M_\odot$. This model, which incorporates finite range interactions through a Yukawa-type finite range force, is contrasted with a conventional zero range Skyrme model. Both models predict nearly identical zero-temperature properties at all densities and proton fractions, including the neutron star maximum mass, but differ in their predictions for heavy-ion flow data. We contrast their predictions of thermal properties, including their specific heats, and provide analytical formulas for the strongly degenerate and nondegenerate limits. We find significant differences in the results of the two models for quantities that depend on the density derivatives of nucleon effective masses. We show that a constant value for the ratio of the thermal components of pressure and energy density expressed as $\Gamma_{\rm th} = 1 + (P_{\rm th}/\varepsilon_{\rm th})$, often used in simulations of proto-neutron stars and merging compact object binaries, fails to adequately describe results of either nuclear model. The region of greatest discrepancy extends from subsaturation densities to a few times the saturation density of symmetric nuclear matter. Our results suggest alternate approximations for the thermal properties of dense matter that are more realistic.

DOI: 10.1103/PhysRevC.92.025801 PACS number(s): 21.65.Mn, 21.30.Fe, 26.50.+x, 97.60.Bw

I. INTRODUCTION

The modeling of core-collapse supernovae, neutron stars from their birth to old age, and binary mergers of compact stars requires a detailed knowledge of the equation of state (EOS) of matter at finite temperature. For use in large-scale computer simulations of these phenomena, the EOS is generally rendered in tabular forms as functions of the baryon density n, temperature T, and the electron concentration $Y_e = n_e/n$, where n_e is the net electron density in matter. Examples of such tabulations can be found, e.g., in Refs. [1–10]. Entries in such tables include thermodynamic state variables such as the free energy, energy per baryon, pressure, entropy per baryon, specific heats, chemical potentials of the various species and their derivatives with respect to number densities, etc. The calculation of a thermodynamically consistent EOS over a wide range of densities (n of 10^{-7} to 1–2 fm^{-3}) and temperatures up to 100 MeV involves a detailed examination of inhomogeneous phases of matter (with neutron-rich nuclei, pastalike geometrical configurations, leptons) at subnuclear densities and low-enough temperatures, as well as homogeneous phases at supranuclear densities with possible non-nucleonic degrees of freedom (Bose condensates, strangeness-bearing particles, mesons, quarks, and leptons).

Constraints on the EOS are largely restricted to zero- or low-temperature matter from experiments involving nuclei and neutron star observations. Decades of experiments involving stable and radioactive nuclei have given us a wealth of data about nuclear masses, charge radii, neutron skin thicknesses, nucleon effective masses, giant resonances, dipole polarizabilities, etc., for isospin asymmetries $\alpha = (N - Z)/(N + Z) \simeq (0 - 0.3)$, N and Z being the neutron and proton numbers of nuclei. This reveals properties of the EOS up to the nuclear equilibrium density of $n_0 \simeq 0.16$ fm^{-3}. Through measurements of the collective flow of matter, momentum, and energy flow, heavy-ion collisions in the range $E_{\rm lab}/A =$ 0.5–2 GeV have shed light on the EOS up to about $3n_0$. Astronomical observations of neutron stars that have central densities and isospin asymmetries several times larger than those of laboratory nuclei have begun to compile accurate data on neutron star masses, rotation periods and their time derivatives, estimates of radii, cooling behaviors that shed light on nucleon superfluidity, etc.

In specific terms, several properties of nuclei, extrapolated to bulk matter, have yielded values for quantities that characterize the key properties of isospin-symmetric nuclear matter such as the equilibrium density n_0, energy per particle E_0 at n_0, compression modulus $K_0 = 9n_0^2(d^2E/dn^2)|_{n_0}$, and the Landau effective mass $m^*(n_0)$, with relatively small 1σ errors, although smaller errors would be desirable. For isospin-asymmetric bulk matter, nuclear data have yielded values for the bulk symmetry energy $S_v = S_2(n_0) = (1/2)(\partial E(n,\alpha)/\partial\alpha^2)|_{\alpha=0}$, where now the neutron excess parameter $\alpha = (n_n - n_p)/(n = n_n + n_p)$, n_n and n_p being the neutron and proton densities in bulk matter, respectively. Additionally, constraints on the derivatives of the symmetry energy at nuclear density, $L_v = 3n_0(dS_2(n)/dn)|_{n_0}$ and $K_v = 9n_0^2(d^2S_2(n)/dn^2)|_{n_0}$ are also beginning to emerge.

Heavy-ion collisions in the energy range $E_{\rm lab}/A =$ 0.5–2 GeV have shed light on the EOS at supra-nuclear

*c.constantinou@fz-juelich.de
†bm956810@ohio.edu
‡prakash@ohio.edu
§james.lattimer@stonybrook.edu

densities (up to $3n_0$–$4n_0$) through studies of matter, momentum, and energy flow of nucleons (see Ref. [11] for a clear exposition). Collective flow of nucleons has been characterized by (i) the mean transverse momentum per nucleon $\langle p_x \rangle / A$ versus rapidity $y/y_{\rm proj}$ [12], (ii) flow angle from asphericity analysis [13], (iii) azimuthal distributions [14], and (iv) radial flow [15]. Confrontation of data with theoretical calculations have generally been performed using Boltzmann-type kinetic equations. One such equation for the phase-space distribution function $f(\vec{r},\vec{p},t)$ of a nucleon that incorporates both the mean-field U and a collision term with Pauli blocking of final states is (see Ref. [11] for a lucid account):

$$\frac{\partial f}{\partial t} + \vec{\nabla}_p U \cdot \vec{\nabla}_r f - \vec{\nabla}_r U \cdot \vec{\nabla}_p f = -\frac{1}{(2\pi)^3} \int d^3p_2\, d^3p_{2'}\, d\Omega \frac{d\sigma_{NN}}{d\Omega} \times v_{12}\, \delta^3(\vec{p} + \vec{p}_2 - \vec{p}_{1'} - \vec{p}_{2'}) [f f_2 (1 - f_{1'})(1 - f_{2'}) - f_{1'} f_{2'} (1 - f)(1 - f_2)]. \quad (1)$$

In general, the mean-field U felt by a nucleon depends on both the local density n and the momentum $\vec{p}$ of the nucleon. Operationally, U is obtained as the functional derivative of the energy density $\mathcal{H}$ of matter *at zero temperature*: $U(n,p) \equiv \delta\mathcal{H}/\delta n$ and serves as an input. The other physical input is the nucleon-nucleon differential cross section $d\sigma_{NN}/d\Omega$, which depends on the relative velocity v_{12}. The *off-equilibrium* evolution of $f(\vec{r},\vec{p},t)$ is performed at a semiclassical level insofar as it is evolved in time classically (see Ref. [11] for a clear exposition) instead of the full quantum evolution of wave functions.

Early theoretical studies that confronted data used isospin averaged cross sections and mean fields of symmetric nuclear matter. The lesson learned was that the collective behavior observed stems from momentum-dependent forces at play during the early stages of the collision [14,16–20]. The conclusion that emerged was that as long $U(n,p)$ saturated at high momenta, as required in optical-model fits to nuclear data a symmetric matter compression modulus of $\simeq 240 \pm 20$ MeV, suggested by the analysis of the giant monopole resonance data [21–23], fits the heavy-ion data as well [24].

The prospects of rare-isotope accelerators (RIAs) that can collide highly neutron-rich nuclei has spurred further work to study a system of neutrons and protons at high neutron excess [25–27]. Generalizing Eq. (1) to a mixture, the kinetic equation for neutrons is

$$\frac{\partial f_n}{\partial t} + \vec{\nabla}_p U \cdot \vec{\nabla}_r f_n - \vec{\nabla}_r U \cdot \vec{\nabla}_p f_n = J_n = \sum_{i=n,p} J_{ni}, \quad (2)$$

where J_n describes collisions of a neutron with all other neutrons and protons. A similar equation can be written for protons with appropriate modifications. In these coupled equations, $U \equiv U(n_n, n_p; \vec{p}\,)$ depends explicitly on the neutron-proton asymmetry. The connection to the symmetry energy arises from U being now obtained from a functional differentiation of the Hamiltonian density $\mathcal{H}(n_n, n_p)$ of isospin-asymmetric matter. Examples of such mean fields may be found in Refs. [26–28]. Isospin asymmetry influences the neutron-proton differential flow and the ratio of neutron to proton multiplicity as a function of transverse momentum at midrapidity. Investigations of these signatures await the development of RIAs at GeV energies to shed light on the EOS at supranuclear densities.

On the astrophysical front, precisely measured neutron star masses and radii severely constrain the EOS of isospin-asymmetric matter. The recently well-measured neutron star masses $1.97 \pm 0.04 M_\odot$ [29] and $2.01 \pm 0.04 M_\odot$ [30] have served to eliminate many, but not all, EOSs in which a substantial softening of the neutron-matter EOS occurred due to the presence of Bose condensates, hyperons, quark matter, etc. [31]. A precise measurement of the radius of the same neutron star for which a mass has been well measured is yet lacking, but reasonable estimates have been made by analysis of x-ray emission from isolated neutron stars, intermittently quiescent neutron stars undergoing accretion from a companion star, and neutron stars that display type I x-ray bursts from their surfaces [32–34].

A common feature shared by the EOSs in Refs. [1–9] is that they fail to reproduce heavy-ion data. The reason is that in both zero range nonrelativistic and relativistic mean-field theoretical (MFT) models, the momentum dependence of $U(n,p)$ leads to a linear dependence on the energy [14,16–18] and [35,36] and is hence at odds with optical-model fits to nucleon-nucleus scattering data [19,20,37,38]. Potential models with finite range interactions (e.g., [39]) lead to a saturating $U(n,p)$ at high momenta and solve this problem [17], but with attendant changes in their thermal properties compared to zero range models, as we show in this work. For a similar resolution in field-theoretical approaches, see, e.g., Ref. [40], in which nonlinear derivatives in mean-field theoretical (MFT) models are employed (finite T results are yet to be calculated) and a forthcoming work in which two-loop effects beyond MFT models are explored [41].

Our first objective in this paper is to inquire whether the EOSs that have successfully explained heavy-ion flow data are able to support the largest well-measured neutron star mass and also if the radii of $1.4 M_\odot$ stars are in accord with bounds established by analyses of currently available x-ray data. We examine models in which finite range interactions are employed as they yield a momentum dependence of the mean-field U that differs significantly at high momenta from that of zero range Skyrme-like models. Specifically, we use the MDI model of Das *et al.* [25], in which the momentum dependence was generated through the use of a Yukawa-type finite range interaction to match the results of microscopic calculations and to reproduce optical-model fits to nucleon-nucleus scattering data. A revised parametrization of the MDI model [labeled MDI(A)] was found necessary to support a $2 M_\odot$ neutron star. We note that Danielewicz *et al.* show the EOS for pure neutron matter in Fig. 5 of Ref. [24], but the maximum mass of a β-stable neutron star was not quoted.

The second objective of this work is to contrast the thermal properties of models with finite range interactions with those of a zero range Skyrme model. For this purpose, we have chosen the SkO′ parametrization [42] of the Skyrme model that yields nearly identical $T = 0$ properties such as the energy density ϵ, pressure P, etc., as the MDI(A) model.

However, the single-particle potentials $U(n_n,n_p,p)$ differ substantially between these models, the MDI(A) model being constant at high momenta, in contrast to the quadratic rise of the SkO′ model. Consequently, the neutron and proton effective masses, m_n^* and m_p^*, also exhibit distinctly different density dependencies, although the isospin splitting of the effective masses is similar in that $m_n^* > m_p^*$ in neutron-rich matter in accordance with Brueckner-Hartree-Fock (BHF) and relativistic BHF calculations [43]. See also the discussion of effective masses in asymmetric matter, e.g., in Ref. [44]. Insofar as m_i^* and dm_i^*/dn control the thermal properties, attendant differences in several of the state variables become evident. Several of the Skyrme parametrizations exhibit a reversal in behavior of the isospin splitting so that $m_n^* < m_p^*$ in neutron-rich matter (see, e.g., Ref. [45] for a compilation, and [46]). This has led us to establish conditions on the strength and range parameters of the Skyrme and MDI models in which $m_n^* > m_p^*$. The exact numerical results of the models studied here are supplemented with analytical results in the limiting cases of degenerate and nondegenerate matter both as a check of our numerical evaluations and to gain physical insights.

An important issue is how experimental information on finite-sized nuclei can constrain the effective masses relevant for the thermal properties of bulk matter. For excitation energies corresponding to $T \leqslant 2$ to 3 MeV, thermal properties of nuclei involve several overlapping energy scales associated with shell and pairing effects, correlations, collective motion, etc. (see, e.g., [47]). The level densities of nuclei inferred from experiments [48] depend on $m_{n,p}^*$ that are determined by both the momentum and energy dependencies of the nucleon self-energy leading to the so-called k mass and ω mass [49–53]. For bulk matter at saturation, in which the predominant effect is from the k mass, $m_{n,p}^*/m = 0.7 \pm 0.1$, has been generally preferred. Prospects for constraining the uncertain effective masses and their density dependencies at nuclear densities and below from laboratory experiments will be addressed elsewhere.

Our third objective is to examine closely the thermal index, $\Gamma_{\rm th} = 1 + (P_{\rm th}/\epsilon_{\rm th})$ and the adiabatic index $\Gamma_S = (d\ln P/d\ln n)_S$ at constant entropy S of hot and dense matter containing leptons and photons for use in astrophysical simulations. The quantity $\Gamma_{\rm th}$ is often used in simulations of binary mergers to save computational time. In addition, in some cases, the implementation of finite-temperature effects is thermodynamically inconsistent. Furthermore, even in cases where thermodynamic consistency is achieved, the values of $\Gamma_{\rm th}$ employed are often taken to be constant and equal to ideal gas values, rather than the highly density-dependent functions suggested by the underlying cold-matter interactions. We therefore provide a detailed numerical and analytical study of $\Gamma_{\rm th}$ and Γ_S (which reflects the overall stiffness of the EOS) for the potential models chosen and contrast them with those of mean field-theoretical models. We demonstrate here that for all models the T and Y_e dependencies of $\Gamma_{\rm th}$ are relatively small, but its strong density dependence is primarily determined by the density dependence of the nucleon effective masses from subsaturation densities to a few times the symmetric matter nuclear saturation density. Inhomogeneous phases below subnuclear densities and exotic phases of matter at supranuclear densities are not considered here as they fall beyond the scope of this work, but will be taken up in a subsequent study.

The organization of this paper is as follows. Section II provides an overview of the role of thermal effects in core-collapse supernovae, evolution of proto-neutron stars, and binary mergers of compact stars. In Sec. III, we describe the finite range (and hence momentum-dependent) and zero range models used to study effects of finite temperature. For the extraction of effects purely thermal in origin, the formalism to evaluate the zero-temperature state variables (energies, pressures, chemical potentials, etc.) of both these models is also presented in Sec. III. Section IV presents an analysis of the zero-temperature results for the models chosen. Thereafter, differences in the momentum dependence of the single-particle potentials between these two models are highlighted. Particular emphasis is placed on the density and isospin dependencies of the Landau effective masses which mainly control the thermal effects discussed in subsequent sections. In Sec. V, results of the exact, albeit numerical, calculations of the thermal effects are presented. This section also contains comparisons with analytical results in the limiting cases of degenerate and nondegenerate matter. The thermal and adiabatic indices and the speed of sound in hot and dense matter of relevance to hydrodynamical simulations of astrophysical phenomena involving supernovae and compact stars are discussed in Sec. VI. Our conclusions are in Sec. VII. Formulas that are helpful in computing the various state variables of the MDI model at zero temperature are collected in Appendix A. In Appendix B, the analytical method by which the nondegenerate limit of the MDI model is addressed is presented. Details concerning the evaluations of the specific heats at constant volume and pressure for the MDI and Skyrme models are given in Appendix C.

II. THERMAL EFFECTS IN ASTROPHYSICAL SIMULATIONS

The effects of temperature in astrophysical simulations are most visible in gravitational collapse supernovae, the evolution of proto-neutron stars (PNSs), and mergers involving neutron stars, either neutron star-neutron star (NS-NS) or black hole-neutron star (BH-NS) mergers.

A. Thermal effects in supernovae and proto-neutron stars

The effects of temperature in supernovae and in PNSs remain largely unexplored in detail, but because for the most part matter in such environments is degenerate, uncertainties in the thermal aspects of the EOS do not play major roles in the early core-collapse phase. For example, maximum central densities at bounce are practically independent of the assumed EOS (see, e.g., [8]). The evolution of PNSs formed folldue core collapse will be more sensitive to thermal effects, as temperatures beyond 50 MeV are reached in the stellar cores and specific entropies S of order $10k_B$ are reached in the stellar mantles [54,55]. The maximum PNS mass and the evolution towards black-hole formation will be dependent upon thermal effects. While the relative stiffness of the EOS (defined

through the incompressibility at saturation) largely controls the time scale for black-hole formation, thermal effects are important in determining the highest central densities reached after bounce. Reference [8] found that the thermal behavior was more important than incompressibility in this regard, largely because of thermal pressure support in the hot, shocked mantles of PNSs. If black holes do not form and a successful explosion ensues, binding energy is largely lost due to neutrino emission and heating in the early evolution of PNSs, due to neutrino downscattering from electrons, and the total neutrino energy dwarfs the thermal energy reservoir. Nevertheless, the temperature at the neutrinosphere, which is located in semidegenerate regions, will be sensitive to thermal properties of the EOS. It remains largely unexplored how the resulting neutrino spectrum, including average energies and emission time scales, depends on thermal aspects of the EOS.

B. Thermal effects in mergers of binary stars

Thermal effects are not expected to play a major role in the evolution of inspiraling compact objects up to the point of merger. However, the evolution of the postmerger remnant and some of the mass ejected could be significantly affected by thermal properties of matter. Perhaps the most significant recent development is the emergence of a standard paradigm concerning mergers of neutron stars. This has been triggered by the discovery of pulsars with approximately two solar masses and strong indications that even larger-mass neutron stars exist from a series of studies of the so-called black-widow and red-back pulsar systems (for a review, see [34]). Most neutron stars in close binaries have measured gravitational masses in the range $1.3M_\odot$ to $1.5M_\odot$. The gravitational mass of the merger remnant will be less than twice as large, due to binding and the ejection of mass. It is unlikely that mass ejection will amount to more than a few hundredths of a solar mass, but binding energies will absorb larger masses. The binding energy fraction, the relative difference between baryon and gravitational masses, can be expressed by a relatively universal relation, i.e., independent of the neutron star EOS, involving only mass and radius [56]:

$$\frac{E_B}{M} \simeq (0.60 \pm 0.05)\frac{\beta}{1-\beta/2}, \tag{3}$$

where $\beta = GM/(Rc^2)$. EOSs capable of supporting $2M_\odot$ maximum masses have the property that, for intermediate-mass stars, the radii are nearly independent of the mass. Furthermore, a concordance of experimental nuclear physics data, theoretical neutron matter studies, and astrophysical observations suggests that this radius is about $R = 12 \pm 0.5$ km [34]. Thus, two equal-mass stars with gravitational masses of $1.3M_\odot$ will have a total baryon mass of $2.87M_\odot$. In a merger event with no mass loss, a remnant of gravitational mass $2.28M_\odot$ would form assuming its radius is also 12 km, representing an additional mass defect of $0.05M_\odot$ relative to the initial stars. Should its radius decrease to about 10 km, its gravitational mass would be approximately $1.9M_\odot$, and the additional mass defect would steepen to $0.43M_\odot$. This gravitational mass could well be below the cold maximum mass. Repeating the above estimates for two $1.5M_\odot$ gravitational mass stars, we find a combined gravitational mass in the range $2.16M_\odot$–$2.59M_\odot$, with mass defects larger than for the previous case. Therefore, it seems likely that the merged object will be close to its cold maximum mass.

Studies show that the merged star will be rapidly rotating, and the rotation may be highly differential [57–59]. Uniform rotation can increase the maximum mass by a few tenths of a percent (see, e.g., Ref. [60]), and differentially rotating objects can support further mass increases. In all likelihood, the merged object will be metastable. This possibility is enhanced if the stellar core is surrounded by a nearly Keplerian disk, a configuration with an even larger metastable mass limit. If the merged remnant mass is above the cold gravitational maximum mass, but less than what rotation is capable of supporting, it is said to be a "hypermassive" neutron star, or HMNS. For a uniformly rotating star, the maximum equatorial radius increase due to rapid rotation is about 50%, with a smaller change in the polar radius. The average density of an HMNS in that case would be less than half of its nonrotating value. As a result, thermal effects can be expected to play a much larger role in the stability of an HMNS than for ordinary neutron stars in which higher degeneracies exist. The maximum mass of the HMNS will decrease with time due to loss of thermal energy from neutrino emission and from loss of angular momentum due to uniformization of the differential rotation [61,62]. Early calculations, for example, those of Refs. [57,58], showed that collapse of the metastable HMNS to a black hole was induced by dissipation of differential rotation and subsequent loss of angular momentum. In contrast, the authors of Ref. [59] argued that thermal effects are much more important than rotation in determining the stability and eventual collapse of an HMNS. In either case, the HMNS lifetime will crucially depend on the relative difference between the HMNS mass and the value for the cold maximum mass for the same number of baryons. The HMNS lifetime, which can range from 10 ms to several seconds [59] is potentially measurable through the duration of short γ-ray bursts associated with neutron star mergers or the duration of gravitational-wave signals from these mergers. Such a measurement, therefore, has the potential of illuminating the EOS.

Kaplan *et al.* [63] have studied the thermal enhancement of the pressure comparing two tabulated hot EOSs, LS220 [1] and Hshen [64], often used in merger simulations. Generally, thermal enhancements above 3 times the nuclear saturation density $\rho_s \simeq 3 \times 10^{14}$ g cm^{-3} are less than about 5%, but at $\rho_s/3$–$\rho_s/2$ the pressure is 3 (for Hshen) or 5 (for LS220) times the cold value. As we will see, this difference is related to the behavior of the nucleon effective mass. In the stellar envelope, for densities from 10^{12} to 10^{14} g cm^{-3}, these enhancements are even larger, ranging from a factor of 10 (Hshen) to 20 (LS220) for a thermal profile in which the average temperature in this density range is about 10 MeV, similar to that found in the merger simulations from the authors of Ref. [59], who employed the Hshen EOS. In the envelope, temperatures are high enough that nuclear dissociation is virtually complete, and the thermal pressure differences can be traced to the behavior of the nucleon effective mass.

Thermal pressure alone is capable of increasing the maximum mass more than 10% above the cold, catalyzed value

for a given EOS [28]. For constant-temperature $T = 50$ MeV profiles studied in Ref. [63], the maximum mass of a hot Hshen star was increased by 15%, while that of a hot LS220 star was increased by approximately 5%. For thermal profiles similar to the simulations of Ref. [59], the increases were more modest: 3.5% and 1.8%, respectively.

Hot rotating configurations can show either an increase or a decrease in mass limits relative to cold rotating configurations [63]. When the central densities are less than about 10^{15} g cm^{-3}, thermal effects increase the masses supported at the mass-shedding rotational limit, and this effect reverses at higher densities. However, the rotational frequency and maximum mass at the mass-shedding limit always decrease due to thermal support: The mass-shedding limit is very sensitive to the equatorial radius, which increases with thermal support. Thermal effects essentially disappear in determining the maximum masses of extremely differentially rotating configurations because the outer regions are largely Keplerian and therefore centrifugally supported.

The analysis in Ref. [63] concludes that thermal pressure support plays little role during the bulk of the evolution of an HMNS, but contributes to the increase of its lifetime by affecting its initial conditions. As hot configurations with central densities less than about 10^{15} g cm^{-3} support larger masses than cold ones with the same central density, those remnants with lower thermal pressure evolve to higher central densities to achieve metastability.

In the case of BH-NS mergers, although the remnant will always involve a black hole, simulations indicate the temporary existence of a remnant disk. While the disk is likely differentially rotating and largely supported by centrifugal effects, and its evolution controlled by angular momentum dissipation, thermal effects will be important for dissipation due to various neutrino processes and emission mechanisms.

Many early simulations of BH-NS mergers employed cold Γ-law EOSs with thermal contributions that were, unfortunately, thermodynamically inconsistent. For example, it has sometimes been assumed that

$$P = \kappa n^{\Gamma} + \frac{3k_B T n}{2m} + f(T) a T^4, \quad \varepsilon = P/(\Gamma - 1), \tag{4}$$

where κ and Γ are constants and $f(T)$ is a temperature-dependent factor reflecting the fraction of relativistic particles in the gas, ranging from 1 at low temperatures to 8 at high temperatures. However, not only should f also be density-dependent, but moreover it can be shown from the above expression for ε that, even if it is treated as being density independent,

$$P = \kappa n^{\Gamma} + aT \int f(T) T^2 dT\,. \tag{5}$$

Obviously, Eqs. (4) and (5) for the pressure are incompatible. Therefore, interpreting the thermal behaviors of merger calculations with Γ-law EOSs is problematic.

Direct comparisons of BH-NS merger simulations with tabulated, temperature-dependent EOSs have yet to be made. Individual simulations with tabulated EOSs have been performed in Ref. [65] with the Hshen EOS and in Ref. [66] with the LS220 EOS. Most focus has been on the properties of the remnant disk formed from the disrupted neutron star which survives on time scales ranging from tens of ms to several s. Typically, densities in the early evolution of the disk range from 1 to 4×10^{11} g cm^{-3}, proton fractions are around $Y_e \sim 0.1$, and specific entropies range from $7k_B$ to $9k_B$. As is the case with HMNS evolutions, the thermal properties control neutrino emissions and the ultimate disk lifetimes.

III. MODELS WITH FINITE AND ZERO RANGE INTERACTIONS

A. Finite range interactions

We adopt the model of Das *et al.* [25], who have generalized the earlier model of Welke *et al.* [14] to the case of isospin-asymmetric nuclear matter. In this model, exchange contributions arising from finite range Yukawa interactions between nucleons give rise to a momentum-dependent mean field. Boltzmann-Uehling-Uhlenbeck (BUU) calculations performed with such a mean field have been able to account for data from nuclear reactions induced by neutron-rich nuclei [67]. Recently, Ref. [68] reported results of thermal properties of asymmetric nuclear matter. The model's predictions for the structural properties of neutron stars and thermal effects for conditions of relevance to astrophysical situations have not been investigated so far and are undertaken here. Explicitly, the MDI Hamiltonian density is given by [25]

$$\mathcal{H} = \frac{1}{2m}(\tau_n + \tau_p) + V(n_n, n_p, T), \tag{6}$$

where

$$n_i = \int d^3 p_i f_i(\vec{r}_i, \vec{p}_i) \quad \text{and} \quad \tau_i = \int d^3 p_i p_i^2 f_i(\vec{r}_i, \vec{p}_i) \tag{7}$$

are the number densities and kinetic energy densities of nucleon species $i = n, p$, respectively. The potential energy density $V \equiv V(n_n, n_p, T)$ is expressed as

$$\begin{aligned} V = {} & \frac{A_1}{2n_0}(n_n + n_p)^2 + \frac{A_2}{2n_0}(n_n - n_p)^2 \\ & + \frac{B}{\sigma + 1}\frac{(n_n + n_p)^{\sigma+1}}{n_0^{\sigma}}\left[1 - y\frac{(n_n - n_p)^2}{(n_n + n_p)^2}\right] \\ & + \frac{C_l}{n_0}\sum_i \int d^3 p_i d^3 p_i' \frac{f_i(\vec{r}_i, \vec{p}_i) f_i'(\vec{r}_i', \vec{p}_i')}{1 + \left(\frac{\vec{p}_i - \vec{p}_i'}{\Lambda}\right)^2} \\ & + \frac{C_u}{n_0}\sum_i \int d^3 p_i d^3 p_j \frac{f_i(\vec{r}_i, \vec{p}_i) f_j(\vec{r}_j, \vec{p}_j)}{1 + \left(\frac{\vec{p}_i - \vec{p}_j}{\Lambda}\right)^2}; \quad i \neq j. \end{aligned} \tag{8}$$

Above, $n_0 \simeq 0.16$ fm^{-3} is the equilibrium density of isospin-symmetric matter. We discuss the choice of the strength parameters A_1, A_2, B, y, C_l, C_u, the parameter σ that captures the density dependence of higher-than-two-body interactions, and of the finite range parameter Λ in subsequent sections. For simplicity, the finite range parameter Λ is taken to be the same for both like and unlike pairs of nucleons, but the strength parameters, C_l and C_u, are allowed to be different. Accounting for 2 spin degrees of freedom, the quantities

$$f_i(\vec{r}_i, \vec{p}_i) = \frac{2}{(2\pi\hbar)^3} f_{p_i} = \frac{2}{(2\pi\hbar)^3}\frac{1}{1 + e^{(\epsilon_{p_i} - \mu_i)/T}} \tag{9}$$

are the phase-space distributions of nucleons in a heat bath of temperature T, having an energy spectrum

$$\epsilon_{p_i} = p_i^2 \frac{\partial \mathcal{H}}{\partial \tau_i} + \frac{\partial \mathcal{H}}{\partial n_i} = \frac{p_i^2}{2m} + U_i(n_n, n_p, p_i), \tag{10}$$

where

$$U_i(n_i, n_j, p_i) = \mathcal{U}_i(n_i, n_j) + R_i(n_i, n_j, p_i); \quad i \neq j, \tag{11}$$

is the single-particle potential (or the mean field). The part that represents contributions arising from the densities alone is

$$\mathcal{U}_i(n_i, n_j) = \frac{A_1}{n_0}(n_i + n_j) + \frac{A_2}{n_0}(n_i - n_j) + B\left(\frac{n_i + n_j}{n_0}\right)^{\sigma}\left\{1 - y\left(\frac{\sigma - 1}{\sigma + 1}\right) \times \left(\frac{n_i - n_j}{n_i + n_j}\right)^2\left[1 + \frac{2}{\sigma - 1}\left(\frac{n_i + n_j}{n_i - n_j}\right)\right]\right\}. \tag{12}$$

The momentum dependence is contained in

$$R_i(n_i, n_j, p_i) = \frac{2C_l}{n_0}\frac{2}{(2\pi\hbar)^3}\int d^3p_i' \frac{f_{p_i'}}{1 + \left(\frac{\vec{p}_i - \vec{p}_i'}{\Lambda}\right)^2} + \frac{2C_u}{n_0}\frac{2}{(2\pi\hbar)^3}\int d^3p_j \frac{f_{p_j}}{1 + \left(\frac{\vec{p}_i - \vec{p}_j}{\Lambda}\right)^2}. \tag{13}$$

At finite temperature, the determination of $R_i(n_i, n_j, p_i)$ requires the knowledge of $R_i(n_i, n_j, p_i')$ for all values of p_i'. As in Hartree-Fock theory, a self-consistency condition must be fulfilled; this is achieved through an iterative procedure as in Ref. [18]. The initial guess is supplied by the zero-temperature $R_i(n_i, n_j, p_i)$ (analytical expressions are given in the next section), which may be used in Eq. (7) to obtain a starting chemical potential $\mu_i^{(0)}$ and energy spectrum $\epsilon_i^{(0)}(p_i)$. These are then used in Eqs. (10) and (7) to obtain $R_i(n_i, n_j, p_i)$ from Eq. (13). This, in turn, leads to $\epsilon^{(1)}(p_i)$, which is used in Eqs. (10) and (7) to find $\mu_i^{(1)}$. Upon repetition of the cycle, convergence is achieved in five or less iterations for most cases. The ensuing chemical potentials μ_i for a given density, temperature, and composition are then used in the standard statistical mechanics expression for the entropy density:

$$s = -\sum_i 2\int \frac{d^3p_i}{(2\pi\hbar)^3}[f_{p_i}\ln f_{p_i} + (1 - f_{p_i})\ln(1 - f_{p_i})]. \tag{14}$$

By integrating this expression twice by parts, s for the MDI model takes the form

$$s = \sum_i \frac{1}{T}\left\{\frac{5\tau_i}{6m} + n_i(\mathcal{U}_i - \mu_i) + 2\int \frac{d^3p_i}{(2\pi\hbar)^3} f_{p_i}\left[R_i(p_i) + \frac{p_i}{3}\frac{\partial R_i(p_i)}{\partial p_i}\right]\right\}. \tag{15}$$

The pressure is acquired through the thermodynamic identity

$$P = -\varepsilon + Ts + \sum_i \mu_i n_i, \tag{16}$$

where the energy density $\varepsilon = \mathcal{H}$. The result in Eq. (15) enables pressure to be cast in the form [18]

$$P = \frac{A_1}{2n_0}(n_n + n_p)^2 + \frac{A_2}{2n_0}(n_n - n_p)^2 + \frac{\sigma B}{\sigma + 1}\frac{(n_n + n_p)^{\sigma+1}}{n_0^{\sigma}}\left[1 - y\left(\frac{n_n - n_p}{n_n + n_p}\right)^2\right] + 2\sum_{i=n,p}\int \frac{d^3p_i}{(2\pi\hbar)^3} f_{p_i}\left\{\frac{p_i^2}{3m} + \frac{p_i}{3}\frac{\partial R_i}{\partial p_i} + \frac{R_i}{2}\right\}. \tag{17}$$

The same expression can also be obtained from Eq. (3.6) of Ref. [18].

We follow Ref. [69] to express the specific heat at constant volume as

$$C_V = \frac{1}{n}\frac{\partial \varepsilon}{\partial T}\bigg|_n \tag{18}$$

and the specific heat at constant pressure as [69]

$$C_P = C_V + \frac{T}{n^2}\frac{\left(\frac{\partial P}{\partial T}\big|_n\right)^2}{\frac{\partial P}{\partial n}\big|_T}. \tag{19}$$

By performing a Jacobi transformation to the variables μ and T,

$$C_V = \frac{\partial \varepsilon}{\partial T}\bigg|_{\mu} - \frac{\frac{\partial \varepsilon}{\partial \mu}\big|_T \frac{\partial n}{\partial T}\big|_{\mu}}{\frac{\partial n}{\partial \mu}\big|_T}, \tag{20}$$

$$C_P = C_V + \frac{T}{n^2}\frac{\left(\frac{\partial P}{\partial T}\big|_{\mu} - \frac{\frac{\partial P}{\partial \mu}\big|_T \frac{\partial n}{\partial T}\big|_{\mu}}{\frac{\partial n}{\partial \mu}\big|_T}\right)^2}{\frac{\frac{\partial P}{\partial \mu}\big|_T}{\frac{\partial n}{\partial \mu}\big|_T}}, \tag{21}$$

respectively.

The calculation of C_V and C_P for the MDI model involves some intricacies not encountered in the zero range Skyrme-like models because $U(n_i, n_p, p)$ in Eq. (10) depends only on the nucleon densities and the temperature. Consequently, derivatives in the above equations must be evaluated with some care, as described in Appendix C.

B. Zero-temperature properties

The MDI Hamiltonian density can be written as the sum of terms arising from kinetic sources, $\mathcal{H}_k$, density-dependent interactions, $\mathcal{H}_d$, and momentum-dependent interactions, $\mathcal{H}_m$:

$$\mathcal{H} = \mathcal{H}_k + \mathcal{H}_d + \mathcal{H}_m. \tag{22}$$

At $T = 0$,

$$\mathcal{H}_k = \frac{1}{2m}(\tau_n + \tau_p) = \frac{1}{2m}\frac{1}{5\pi^2\hbar^3}(p_{Fn}^5 + p_{Fp}^5), \tag{23}$$

$$\mathcal{H}_d = \frac{A_1}{2n_0}n^2 + \frac{A_2}{2n_0}n^2(1-2x)^2 + \frac{B}{\sigma+1}\frac{n^{\sigma+1}}{n_0^\sigma}[1-y(1-2x)^2], \quad (24)$$

$$\mathcal{H}_m = \frac{C_l}{n_0}(I_{nn}+I_{pp}) + \frac{2C_u}{n_0}I_{np}, \quad (25)$$

with

$$p_{Fi} = (3\pi^2 n_i \hbar^3)^{1/3}, \quad (26)$$

$$I_{ij} = \frac{8\pi^2\Lambda^2}{(2\pi\hbar)^6}\left\{p_{Fi}p_{Fj}\left(p_{Fi}^2+p_{Fj}^2\right) - \frac{p_{Fi}p_{Fj}\Lambda^2}{3} + \frac{4\Lambda}{3}\left(p_{Fi}^3-p_{Fj}^3\right)\arctan\left(\frac{p_{Fi}-p_{Fj}}{\Lambda}\right) - \frac{4\Lambda}{3}\left(p_{Fi}^3+p_{Fj}^3\right)\arctan\left(\frac{p_{Fi}+p_{Fj}}{\Lambda}\right) + \left[\frac{\Lambda^4}{12} + \frac{\left(p_{Fi}^2+p_{Fj}^2\right)\Lambda^2}{2} - \frac{\left(p_{Fi}^2-p_{Fj}^2\right)^2}{4}\right] \times \ln\left[\frac{(p_{Fi}+p_{Fj})^2+\Lambda^2}{(p_{Fi}-p_{Fj})^2+\Lambda^2}\right]\right\}. \quad (27)$$

We note that Eq. (3.5) in Ref. [25], which agrees with Eq. (27) above for isospin-symmetric matter and for pure neutron matter, must be corrected to properly account for properties of bulk matter with intermediate isospin content.

The energy per particle, the pressure, and the chemical potentials are obtained from the relations

$$E = \frac{\mathcal{H}}{n}, \quad P = n\frac{\partial\mathcal{H}}{\partial n} - \mathcal{H}, \quad \text{and} \quad \mu_i = \frac{\partial\mathcal{H}}{\partial n_i}, \quad (28)$$

where $n = n_n + n_p$ is the total baryon number density.

Symmetric nuclear-matter properties at the saturation density $n_0 = 0.16\,\mathrm{fm}^{-3}$ such as the compression modulus K_0, the symmetry energy S_v, as well as its slope L_v and curvature K_v are obtained from

$$K_0 = K(n=n_0, x=1/2) = 9n_0\left.\frac{\partial^2\mathcal{H}}{\partial n^2}\right|_{n=n_0,x=1/2}, \quad (29)$$

$$S_v = S_2(n_0); \quad S_2 = \frac{1}{8n}\left.\frac{\partial^2\mathcal{H}}{\partial x^2}\right|_{x=1/2}, \quad (30)$$

$$L_v = L_2(n_0) = 3n_0\left.\frac{dS_2}{dn}\right|_{n=n_0}, \quad (31)$$

$$K_v = K_2(n_0) = 9n_0^2\left.\frac{d^2S_2}{dn^2}\right|_{n=n_0}. \quad (32)$$

The proton fraction x is defined as $x = n_p/(n_n+n_p)$.

The $T=0$ single-particle energy spectrum is

$$\epsilon_{p_i} = \frac{p_i^2}{2m} + U_i(n_i, n_j, p_i), \quad (33)$$

with

$$U_i(n_i,n_j,p_i) = \mathcal{U}_i(n_i,n_j) + \frac{2C_l}{n_0}R_{ii}(n_i,p_i) + \frac{2C_u}{n_0}R_{ij}(n_j,p_i), \quad (34)$$

where $i \neq j$, and

$$R_{ij}(n_j,p_i) = \frac{\Lambda^3}{4\pi^2\hbar^3}\left\{\frac{2p_{Fj}}{\Lambda} - 2\left[\arctan\left(\frac{p_i+p_{Fj}}{\Lambda}\right) - \arctan\left(\frac{p_i-p_{Fj}}{\Lambda}\right)\right] + \frac{\left(\Lambda^2+p_{Fj}^2-p_i^2\right)}{2\Lambda p_i} \times \ln\left[\frac{(p_i+p_{Fj})^2+\Lambda^2}{(p_i-p_{Fj})^2+\Lambda^2}\right]\right\}, \quad (35)$$

from which the nucleon effective masses can be derived:

$$m_i^* = p_{Fi}\left(\left.\frac{\partial\epsilon_{p_i}}{\partial p_i}\right|_{p_{Fi}}\right)^{-1} = \frac{m}{1+\left.\frac{m}{p_{Fi}}\frac{\partial U_i}{\partial p_i}\right|_{p_{Fi}}}. \quad (36)$$

Explicitly,

$$m_i^* = p_{Fi}\left(\frac{p_{Fi}}{m} + \frac{2C_l}{n_0}\left.\frac{\partial R_{ii}}{\partial p_i}\right|_{p_{Fi}} + \frac{2C_u}{n_0}\left.\frac{\partial R_{ij}}{\partial p_i}\right|_{p_{Fi}}\right)^{-1}, \quad (37)$$

$$\left.\frac{\partial R_{ij}}{\partial p_i}\right|_{p_{Fi}} = \frac{\Lambda^2}{2\pi^2\hbar^3}\frac{p_{Fj}}{p_{Fi}}\left\{1 - \frac{\left(\Lambda^2+p_{Fj}^2+p_{Fi}^2\right)}{4p_{Fi}p_{Fj}} \times \ln\left[\frac{(p_{Fi}+p_{Fj})^2+\Lambda^2}{(p_{Fi}-p_{Fj})^2+\Lambda^2}\right]\right\}. \quad (38)$$

Expressions for P, μ_i, and U_i and the derivatives of m_i^* with respect to the nucleon densities are collected in Appendix A.

C. Zero range Skyrme interactions

For comparison with the results of the finite range model discussed above, we also consider the often studied zero range model due to Skyrme [70]. In its standard form, the Skyrme Hamiltonian density reads as

$$\mathcal{H} = \frac{1}{2m_n}\tau_n + \frac{1}{2m_p}\tau_p + n(\tau_n+\tau_p)\left[\frac{t_1}{4}\left(1+\frac{x_1}{2}\right) + \frac{t_2}{4}\left(1+\frac{x_2}{2}\right)\right] + (\tau_n n_n + \tau_p n_p)\left[\frac{t_2}{4}\left(\frac{1}{2}+x_2\right) - \frac{t_1}{4}\left(\frac{1}{2}+x_1\right)\right] + \frac{t_o}{2}\left(1+\frac{x_o}{2}\right)n^2 - \frac{t_o}{2}\left(\frac{1}{2}+x_o\right)\left(n_n^2+n_p^2\right) + \left[\frac{t_3}{12}\left(1+\frac{x_3}{2}\right)n^2 - \frac{t_3}{12}\left(\frac{1}{2}+x_3\right)\left(n_n^2+n_p^2\right)\right]n^\epsilon. \quad (39)$$

Explicit forms of the single-particle potentials for the SkO′ Hamiltonian (with $Y_i = n_i/n, i = n, p$) are

$$U_i(n,k) = (X_1 + Y_i X_2)nk^2 + (X_1 + X_2)\tau_i + X_1\tau_j + 2n(X_3 + Y_i X_4) + n^{1+\epsilon}\{(2+\epsilon)X_5 + [2Y_i + \epsilon(Y_i^2 + Y_j^2)]X_6\}; \quad i \neq j, \tag{40}$$

where

$$X_1 = \frac{1}{4}\left[t_1\left(1 + \frac{x_1}{2}\right) + t_2\left(1 + \frac{x_2}{2}\right)\right],$$
$$X_2 = \frac{1}{4}\left[t_2\left(\frac{1}{2} + x_2\right) - t_1\left(\frac{1}{2} + x_1\right)\right],$$
$$X_3 = \frac{t_0}{2}\left(1 + \frac{x_0}{2}\right); \quad X_4 = -\frac{t_0}{2}\left(\frac{1}{2} + x_0\right),$$
$$X_5 = \frac{t_3}{12}\left(1 + \frac{x_3}{2}\right); \quad X_6 = -\frac{t_3}{12}\left(\frac{1}{2} + x_3\right). \tag{41}$$

From Eq. (36), the density-dependent Landau effective masses are

$$\frac{m_i^*}{m} = \left[1 + \frac{2m}{\hbar^2}(X_1 + Y_i X_2)n\right]^{-1}. \tag{42}$$

The derivations of the various state variables, nuclear saturation properties, and thermal response functions proceed as previously described for MDI. For details of evaluating the thermal state variables for Skyrme-like models, we refer the reader to a recent compilation of formulas and numerical methods in Ref. [71]. For numerical values of the various strength parameters above, we choose the SkO′ parametrization of Ref. [42].

IV. RESULTS FOR ZERO TEMPERATURE

In this section, we consider the zero-temperature properties of the finite range and zero range models discussed in the previous section. We begin with the MDI(0) parametrization of the model of Das *et al.* [25] so that its characteristics extended to neutron star matter, not considered previously, may be assessed.

A. MDI models for isospin-asymmetric matter

Table I lists the various parameters employed in the MDI(0) model of Ref. [25]. In Table II, we list the characteristic properties of this model at the equilibrium density of isospin-symmetric nuclear matter. Also included in this table are values of the various physical quantities (the last three rows) accessible to laboratory experiments for small isospin asymmetry. Note the fairly good agreement with experimental determinations of the various quantities.

TABLE I. Values for the MDI(0) Hamiltonian density of [25].

Parameter	Value	Parameter	Value
A_1	−108.28 MeV	y	0
A_2	−12.30 MeV	C_l	−11.70 MeV
B	106.35 MeV	C_u	−103.40 MeV
σ	4/3	Λ	263.04 MeV

TABLE II. Entries are at the equilibrium density n_0 of symmetric nuclear matter for the MDI(0) model [25]. E_0 is the energy per particle, K_0 is the compression modulus, m_0^*/m is the ratio of the Landau effective mass to mass in vacuum, S_v is the nuclear symmetry energy, L_v and K_v are related to the first and second derivatives of the symmetry energy, respectively.

Property	Value [MDI(0)]	Experiment	Reference
n_0 (fm^{-3})	0.16	0.17 ± 0.02	[72–75]
E_0 (MeV)	−16.10	−16 ± 1	[74,75]
K_0 (MeV)	212.4	230 ± 30	[22,23]
		240 ± 20	[76]
m_0^*/m	0.67	0.8 ± 0.1	[77,78]
S_v (MeV)	30.54	30–35	[79,80]
L_v (MeV)	60.24	40–70	[79,80]
K_v (MeV)	−81.67	−100 ± 200	[71]

In Table III, the structural properties of neutron stars built using the EOS of charge-neutral and β-equilibrated matter from the MDI(0) model are summarized. The predicted maximum mass falls slightly short of the largest well-measured mass. The radii of the maximum mass and $1.4M_\odot$ stars are in reasonable agreement with their current estimations from x-ray data. A noteworthy feature is the central baryon chemical potential of the maximum-mass star, $\mu_c \sim 1.9$ GeV, which is below the limit of 2.1 GeV set by the maximally compact EOS of a neutron star derived in Ref. [31]. Note that the density n_a, at which the EOS violates causality, that is, the squared speed of sound $c_s^2 = dP/d\epsilon > 1$ (a common feature of potential models), lies well above the central density of the maximum star, as is the case for all models discussed in subsequent sections.

TABLE III. $M_{\max}$ is the maximum neutron star mass for the MDI(0) model and $R_{\max}$ is its radius. Other entries are the central density n_c, energy density ϵ_c, pressure P_c, the chemical potential μ_c for both $M_{\max}$ and $1.4M_\odot$ configurations, and the density n_a at which the EOS becomes acausal. The radius of a $1.4M_\odot$ neutron star is given by $R_{1.4}$.

Property	Value [MDI(0)]	Observation	Reference
$M_{\max}$ ($M_\odot$)	1.884	2.01 ± 0.04	[30]
$R_{\max}$ (km)	9.84	11.0 ± 1.0	[32]
n_c (fm^{-3})	1.3065		
ϵ_c (MeV fm^{-3})	1703.3		
P_c (MeV fm^{-3})	761.22		
μ_c (MeV)	1886.3		
n_a (fm^{-3})	1.883		
$R_{1.4}$ (km)	11.77	11.5 ± 0.7	[32]
n_c (fm^{-3})	0.5782		
ϵ_c (MeV fm^{-3})	599.19		
P_c (MeV fm^{-3})	91.784		
μ_c (MeV)	1195.0		

TABLE IV. Values for the MDI(A) Hamiltonian density.

Parameter	Value	Parameter	Value
A_1	−69.4758 MeV	y	−0.032 792 9
A_2	−29.2241 MeV	C_l	−23.0576 MeV
B	100.084 MeV	C_u	−105.885 MeV
σ	1.362 27	Λ	420.864 MeV

B. Revised parametrization of the MDI model

In this section, we provide a revised set of parameters (see Table IV) for the MDI model so that the isospin-symmetric and -asymmetric properties at the nuclear-matter equilibrium density are closer to the experimentally derived mean values than given by the MDI(0) parametrization and the neutron star maximum mass also comes close to the recently observed 2 solar mass. We note that this model also allows us to constrain the single-particle potential $U(n,p)$ to match optical-model fits to data. We have used $U(n_0, p = 0) = -74.6$ MeV and $U[n_0, p^2/(2m) = 303.1 \text{ MeV}] = 0$ in determining the constants of the model as the variational Monte Carlo calculations of Wiringa in Ref. [81] suggest. The asymptotically flat behavior of $U(n_0, p) \simeq 30.6$ MeV with p arises naturally from effects of the finite range interaction in this model.

C. Parameters of a prototype Skyrme model

As an example of a zero range model, we have chosen to work with the Skyrme model of Ref. [42] known as SkO′, the parameters of which are listed in Table V. For an apposite comparison, the parameters of the MDI(A) model were tuned so that its energy per particle vs baryon density closely matches that of the SkO′ model for both symmetric matter and pure neutron matter.

Comparison of MDI(A) and SkO′ *models*

Attributes of the MDI(A) and SkO′ models at their respective equilibrium densities of symmetric nuclear matter are presented in Table VI. The resulting structural aspects of neutrons stars from these two models are presented in Table VII. These results indicate the nearly identical nature of the two models at zero temperature. As with the MDI(0) model, the central baryon chemical potentials for these models also lie below the value for the maximally compact EOS.

We wish to add that neutron star maximum masses in excess of $2M_\odot$ can also be obtained from a reparametrization of the MDI model, but at the expense of losing close similarity with the results of the SkO′ model. An illustration is provided with $K_0 = 260$ MeV, $L_v = 70$ MeV, and $K_v = -50$ MeV,

TABLE V. Values for the Skyrme Hamiltonian density SkO′.

	t_i	x_i	ϵ
0	−2099.419 MeV fm^3	−0.029 503	1/4
1	301.531 MeV fm^5	−1.325 732	
2	154.781 MeV fm^5	−2.323 439	
3	13 526.464 MeV fm$^{3(1+\epsilon)}$	−0.147 404	

TABLE VI. As Table II for the MDI(A) and SkO′ models.

Property	Value [MDI(A)]	Value [SkO′]	Experiment	Reference
n_0 (fm^{-3})	0.160	0.160	0.17 ± 0.02	[72–75]
E_0 (MeV)	−16.00	−15.75	−16 ± 1	[74,75]
K_0 (MeV)	232.0	222.3	230 ± 30	[22,23]
			240 ± 20	[76]
m_0^*/m	0.67	0.90	0.8 ± 0.1	[77,78]
S_v (MeV)	30.0	31.9	30–35	[79,80]
L_v (MeV)	65.0	68.9	40–70	[79,80]
K_v (MeV)	−72.0	−78.8	−100 ± 200	[71]

while keeping the other saturation properties the same as for MDI(A). This was achieved through the choice of the constants $A_1 = -39.0752$, $A_2 = -27.4916$, $B = 69.6838$, $\sigma = 1.564\,97$, $y = -0.105\,539$, $C_l = -26.95$, $C_u = -101.993$, and $\Lambda = 420.864$, the units of these constants being the same as in Table I. Results for the structural properties of a neutron star in β equilibrium are $M_{\max} = 2.153 M_\odot$, $R_{\max} = 10.58$ km, and $R_{1.4} = 12.13$ km. At the edges of the 1σ errors of the empirical saturation properties at the nuclear equilibrium density, it is not difficult to raise the maximum mass well above $2M_\odot$.

D. Single-particle potentials

In this section, we present results of the single-particle potentials for the MDI(A) and SkO′ models from Eqs. (34) and (40), respectively, and contrast them with those from the microscopic calculations of Refs. [81] and [82].

Figure 1 shows the neutron single-particle potentials for MDI(A) and SkO′ as functions of momentum for select baryon densities at zero temperature. Results shown are for pure neutron matter ($x = 0$) [Fig. 1(a)] and for isospin-asymmetric matter with $x = 0.2$ [Fig. 1(b)]. Notice that the results for MDI(A) tend to saturate at large momenta for both proton fractions due to the logarithmic structure of Eq. (35). The SkO′ model, however, in common with most Skyrme models, exhibits a quadratic rise with momentum. This latter feature is

TABLE VII. As Table III for the MDI(A) and SkO′ models.

Property	Value [MDI(A)]	Value [SkO′]	Observation	Reference
$M_{\max}$ ($M_\odot$)	1.9725	1.9600	2.01 ± 0.04	[30]
$R_{\max}$ (km)	10.20	10.13	11.0 ± 1.0	[32]
n_c (fm^{-3})	1.2065	1.2233		
ϵ_c (MeV fm^{-3})	1573.4	1595.7		
P_c (MeV fm^{-3})	718.90	739.42		
μ_c (MeV)	1900.0	1908.9		
n_a (fm^{-3})	1.64	1.678		
$R_{1.4}$ (km)	12.21	12.17	11.5 ± 0.7	[32]
n_c (fm^{-3})	0.5126	0.5234		
ϵ_c (MeV fm^{-3})	526.36	533.06		
P_c (MeV fm^{-3})	75.802	78.421		
μ_c (MeV)	1174.7	1168.3		

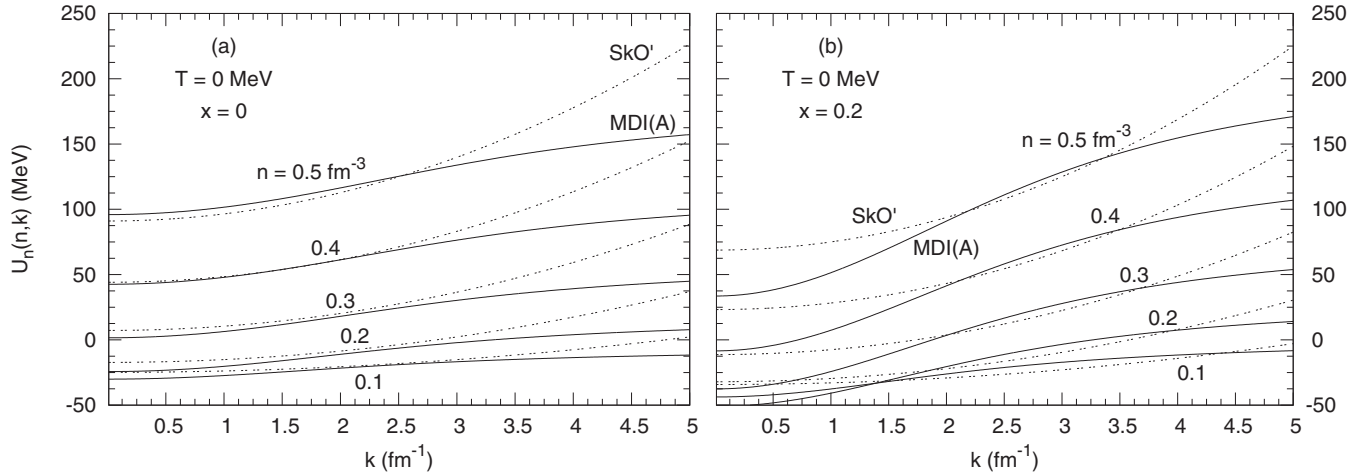

FIG. 1. Neutron single-particle potentials vs momentum at $T = 0$ for the densities n and proton fractions x as marked. Results for the MDI(A) model (solid curves) from Eqs. (10), (34), and (35). Those for the SkO′ model (dashed curves) from Eq. (40).

also present in the results of the Akmal, Pandharipande, and Ravenhall (APR) model [83] in which the Hamiltonian density of the many-body calculations of Akmal and Pandharipande [84] is parametrized in Skyrme-like fashion. For both MDI(A) and SkO′ models the effect of a finite x [Fig. 1(b)] is more pronounced at low momenta for which the single-particle potential becomes more attractive relative to that for pure neutron matter.

In Fig. 2, the neutron single-particle potentials vs momentum for the MDI(A) model from Eqs. (34) (solid curves) and for the SkO′ model from Eq. (35) (dashed curves) are compared with the variational Monte Carlo results (solid curves marked with asterisks) of Ref. [81] using the UV14-TNI interaction and the Bruekner-Hartree-Fock results (dash-dotted curves) of Ref. [82] with the inclusion of three-body interactions (labeled BHF-TBF). Results are for symmetric nuclear matter at about one, two, and three times the nuclear-matter equilibrium density in panels (a), (b), and (c), respectively. A curve-to-curve quantitative comparison between the results of models used in this work and those of UV14-TNI and BHF-TBF models is not appropriate because the saturation properties of the latter models differ significantly from those of the former ones. Specifically, for the UV14-TNI model, $E_0 = -16.6$ MeV at $n_0 = 0.157$ fm^{-3}, with $K_0 = 260$ MeV, whereas for the BHF-TBF model, $E_0 = -15.08$ MeV at $n_0 = 0.198$ fm^{-3}, with $K_0 = 207$ MeV. In this work, the single-particle potential was designed to mimic closely the behavior of the UV14-TNI model. However, the qualitative trends—power-law rise vs logarithmic rise—at high momenta in other microscopic models are worth noting as discussed below.

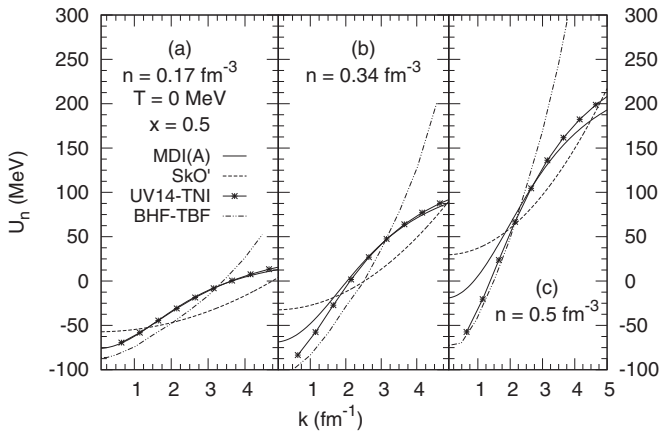

FIG. 2. Comparison of neutron single-particle potentials vs momentum from Eqs. (34) and (35) with the variational Monte Carlo results of Ref. [81] using the UV14-TNI interaction and Bruekner-Hartree-Fock results of Ref. [82] with the inclusion of three-body interactions (labeled BHF-TBF).

At the densities shown, and at high momenta, there is good agreement between the results of the MDI(A) model and those of the UV14-TNI model by design. As mentioned in the Introduction, this saturating behavior at high momenta is in accord with the analysis of optical model fits to nucleon-nucleus scattering data. The other two models, SkO′ and BHF-TBF, rise quadratically with momenta. In the case of the SkO′ model, this behavior ensues from the zero range approximation made for nuclear interactions. In the case of the BHF-TBF calculations, the quadratic rise with momentum stems from the similar behavior of $U(n,k)$ chosen for purposes of convergence during numerical calculations. Such a behavior of the single-particle potential, even with the symmetric nuclear-matter compression moduli around 240 MeV, leads to nucleon collective flows that are larger than those observed in heavy-ion collisions [14,16–18]. We note that Danielewicz reaches similar conclusions with a different parametrization $U(n,p)$, which also saturates at high momenta (see Fig. 17 of Ref. [19]).

E. Isospin dependence of effective masses

The single-particle potentials discussed above facilitate the calculation of the Landau effective masses of nucleons according to Eq. (36). For the MDI(A) and SkO′ models, explicit expressions as functions of density and proton fraction were given in Eqs. (38) and (42), respectively.

In Fig. 3, the neutron and proton effective masses scaled with the vacuum nucleon mass are shown as a function of

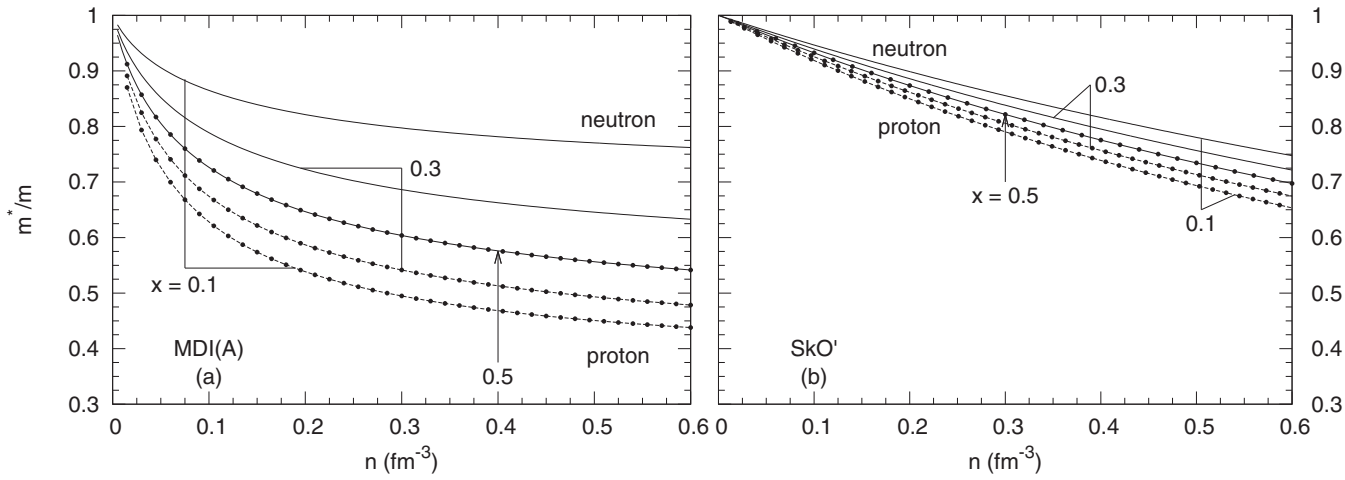

FIG. 3. Landau effective masses of the neutron and proton vs baryon density n for the marked values of the proton fraction x. (a) Results for the MDI(A) model from Eqs. (37) and (38). (b) Same as (a), but for the SkO′ model from Eq. (36).

baryon density for select proton fractions for the MDI(A) and SkO′ models in panels (a) and (b), respectively. Although these two models yield similar properties for most observables for symmetric nuclear matter at the equilibrium density n_0, the effective masses are significantly different; $m_0^*/m = 0.67(0.9)$ for the MDI(A) (SkO′) model (see Table VI). The density dependence of $m_{n,p}^*/m$ also differs significantly between the two models: a logarithmic decrease in the MDI(A) model vs a $[1 + (\text{constant}) \cdot n]^{-1}$ decrease with density in the SkO′ model. Effects of isospin content as it varies from that of symmetric nuclear matter ($x = 0.5$) toward pure neutron matter ($x \to 0$) are qualitatively similar, but quantitatively different with MDI(A) producing a significantly larger change compared with SkO′. It is worthwhile to note, however, that several parametrizations of Skyrme interactions exist in the literature which yield a larger variation of $m_{n,p}^*/m$ with varying x than is present in the SkO′ model, although the logarithmic decline with density of the MDI models would be absent in all of them.

A noteworthy feature of the results in Figs. 3(a) and 3(b) is that $m_n^* > m_p^*$ for all densities as x moves from its symmetric matter value of 0.5 to 0, the value for pure neutron matter. The cause for this behavior may be traced to the values of strength and range parameters that govern the behavior of effective masses with proton fraction. For example, if we require the condition $m_n^* > m_p^*$ to be satisfied for the MDI models, Eq. (38) implies that to leading order in n and for all x

$$C_l - C_u > 0, \tag{43}$$

independent of the finite range parameter Λ. Next-to-leading order in n and for all x, the condition becomes

$$C_l\left[1 - \frac{20}{3}\left(\frac{p_F}{\Lambda}\right)^2 + 4\left(\frac{n}{n_0}\right)\left(\frac{mC_l}{\Lambda^2}\right)\right] - C_u\left[1 - 4\left(\frac{p_F}{\Lambda}\right)^2 + 4\left(\frac{n}{n_0}\right)\left(\frac{mC_u}{\Lambda^2}\right)\right] > 0, \tag{44}$$

where p_F above is the Fermi momentum of symmetric nuclear matter. As $(20/3)(p_F/\Lambda)^2 > 4(p_F/\Lambda)^2$, the condition becomes $aC_l > C_u$, with $a < 1$. These conditions are met for the MDI(0) (and for all the MDI models in Ref. [25]) and MDI(A) models, which ensures that $m_n^* > m_p^*$ for all x in the range 0.5–0.

For Skyrme interactions, Eq. (42) implies that $m_n^* > m_p^*$ in neutron-rich matter as long as

$$t_1(1 + 2x_1) > t_2(1 + x_2), \tag{45}$$

which is satisfied by the parameters in Table V.

When the conditions in Eqs. (43), (44), and (45) are not satisfied, a reversal in the behavior of neutron and proton effective masses occurs; that is, $m_n^* < m_p^*$ as x moves away from 0.5 toward 0. For examples of Skyrme interactions exhibiting this behavior, see the compilation in Ref. [45] and also Ref. [46]. Notwithstanding this behavior, the properties of symmetric nuclear matter, symmetry energy attributes, and collective excitations of nuclei have been well described. Additionally, the requirement that the EOS of neutron star

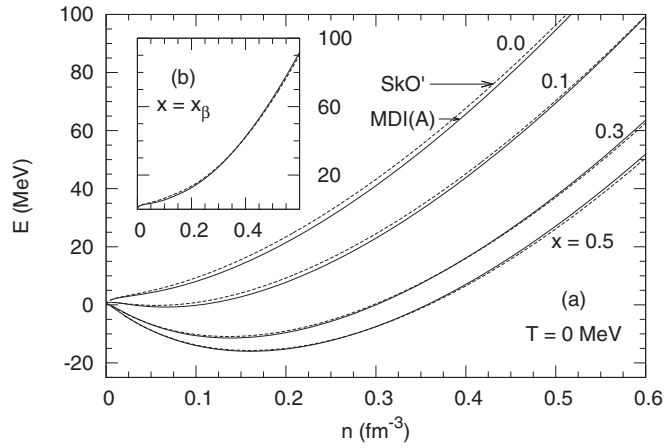

FIG. 4. (a) Energy per particle $E = \mathcal{H}/n$ vs baryon number density n ($T = 0$) at the proton fractions x for the MDI(A) model from Eqs. (23)–(25) and the SkO′ model from Eq. (39). (b) E vs n for matter with proton fractions x_β determined from charge neutrality and β equilibrium.

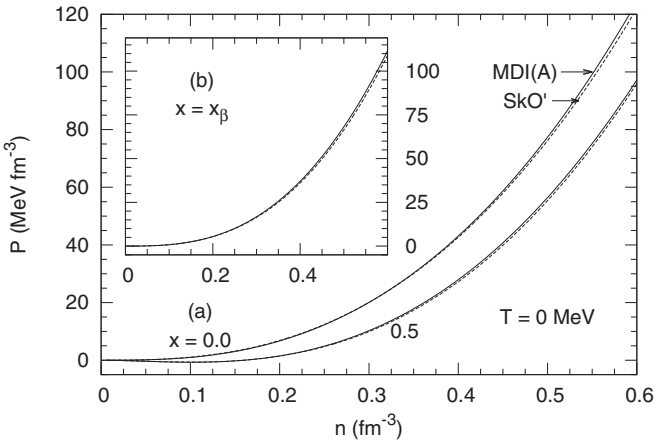

FIG. 5. (a) Pressure P vs baryon density n ($T = 0$) at the proton fractions x shown for the MDI(A) model from Eqs. (A1)–(A6) and the SkO′ model from Eq. (28). (b) P vs n for x_β determined from charge neutrality and β equilibrium.

matter is able to support stars of $2M_\odot$ has also been met. It is worthwhile noting that in the microscopic BHF and Dirac-Brueckner-Hartree-Fock calculations that include three-body interactions, $m_n^* > m_p^*$ in neutron-rich matter [85–88]. Their density dependencies, while akin to those of Skyrme-like models with similar splitting exhibit quantitative differences only. The isospin splitting of the effective masses in the MDI(A) model is in agreement with the above microscopic models.

F. Energy, pressure, and chemical potentials

The energy per baryon $E = \mathcal{H}/n$ from the MDI(A) and SkO′ models is presented as functions of baryon density and proton fraction in Fig. 4. Explicit expressions for $\mathcal{H}$ are in Eq. (25) for the MDI model and in Eq. (39) for the SkO′ model. For all proton fractions ranging from pure neutron matter to symmetric nuclear matter shown in Fig. 4(a) there is little difference between the energies of the two models, the energy for the SkO′ model being slightly larger than that of MDI for pure neutron matter at all densities. The inset in Fig. 4(b) shows the energy per baryon of nucleons vs baryon density for charge-neutral matter in β equilibrium. The two models yield nearly the same energy at most densities with only small differences around the nuclear-matter density.

In Fig. 5(a), we show the pressures exerted by nucleons resulting from the MDI(A) and SkO′ models as functions of density for symmetric nuclear and pure neutron matter. The results in Fig. 5(b) correspond to charge-neutral matter in β equilibrium. Both models have nearly identical pressures regardless of the proton fraction with small differences at the highest densities shown.

The density dependence of the neutron and proton chemical potentials from the MDI(A) and SkO′ models are presented in Figs. 6(a) and 6(b), respectively. For all proton fractions presented ($x = 0.1$, 0.3, and 0.5), the neutron chemical potentials of the two models agree at all densities. Small differences between the two models are observed in the proton chemical potentials, with the largest difference occurring at low proton fractions and large baryon densities. Figure 6(c) shows the difference between the neutron and proton chemical potentials ($\hat{\mu} = \mu_n - \mu_p$) vs density for the MDI(A) and SkO′ models, respectively. As there is little difference between the neutron chemical potentials of the two models, the small differences between the $\hat{\mu}$′s stem from differences in the proton chemical potentials. The differences in $\hat{\mu}$ occur mainly for low proton fractions and high densities.

G. Properties of cold-catalyzed neutron stars

In Figs. 7(a) and 7(b), we show the gravitational mass vs radius (M_G vs R) and mass vs central density (M_G vs n_c) of cold-catalyzed neutron stars for the MDI(A) and SkO′ models. Not unexpectedly, the results are very nearly the same as the P vs n relations in neutron star matter are nearly identical for the two models [see Fig. 5(b)]. The close to vertical rise of mass with radius is attributable to the similar behaviors of the symmetry energies in the two models (characterized by similar values of L at n_0).

The central densities of stars with different masses are of relevance in the long-term cooling of neutron stars [89]. For up to 10^6 yr after their birth, neutron stars cool primarily through neutrino emission. As pointed out in Ref. [89], the density dependence of $S_2(n)$, more precisely $\Delta E(n)$, determines the threshold densities for the rapid direct Urca processes $n \leftrightarrow p + e^- + \bar{\nu}_e$ and $n \leftrightarrow p + \mu^- + \bar{\nu}_\mu$ to occur.

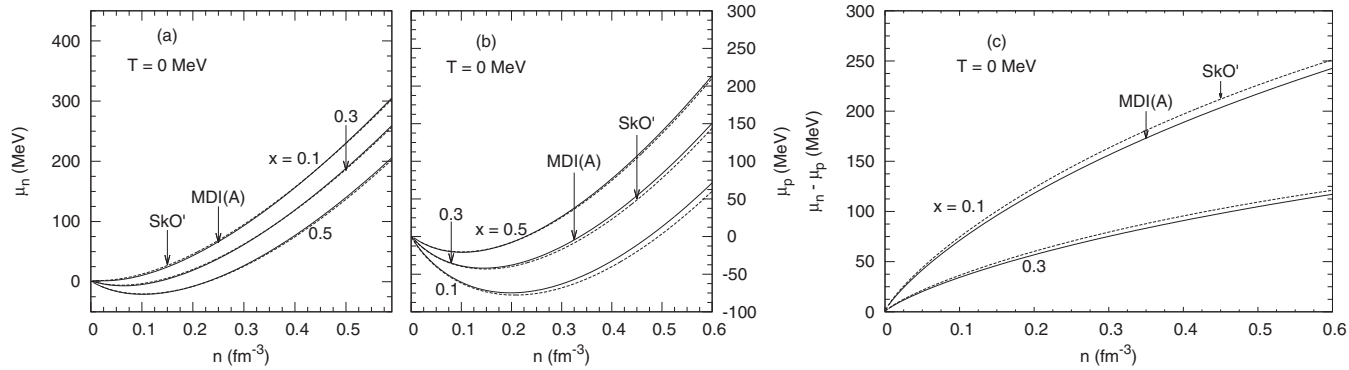

FIG. 6. (a),(b) The neutron and proton chemical potentials vs baryon density n for the MDI(A) [Eqs. (A7)–(A10)] and the SkO′ [Eq. (28)] models for values of x shown. (c) $\hat{\mu} = \mu_n - \mu_p$ vs n.

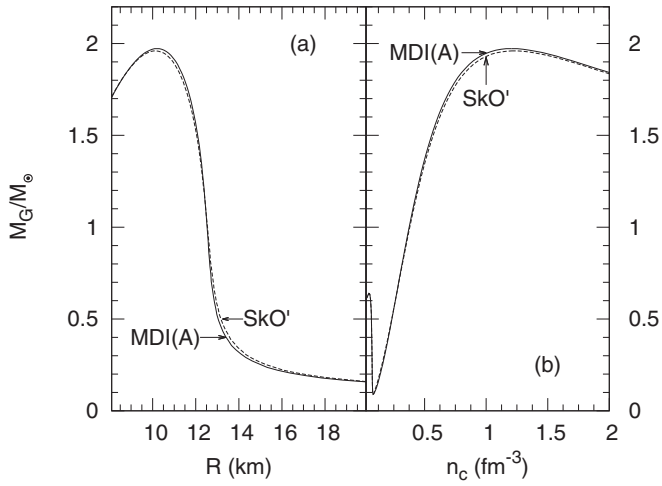

FIG. 7. (a) Mass vs radius and (b) mass vs central density of $T = 0$ neutron stars for the MDI(A) and SkO′ models.

In charge-neutral ($n_{e^-} + n_{\mu^-} = n_p$) and β-equilibrated ($\hat{\mu} = \mu_{e^-} = \mu_{\mu^-}$) neutron star matter, the threshold densities for these direct Urca processes are determined when the triangular inequalities

$$p_{F_i} + p_{F_j} \geqslant p_{F_k}, \tag{46}$$

where i, j, and k are p, $e^-(\mu^-)$, and n, and cyclic permutations of them are satisfied (neutrinos at the relevant temperatures contributing little to the momentum balance conditions). For the process involving electrons (and muons), the threshold density is 0.67(0.93) fm^{-3} for the MDI(A) model. Thus, stars with masses $M > 1.7M_\odot$ will undergo rapid cooling from neutrino emission from the process involving electrons, while those with $M > 1.9M_\odot$ will receive an equal and additional contribution to neutrino emissivity from the process with muons. The corresponding numbers for the SkO′ model are 0.59(0.92) fm^{-3} and 1.5(1.9)$M_\odot$, respectively.

V. THERMAL EFFECTS

Finite-temperature effects can be studied by isolating the thermal part of the various functions of interest defined as the difference between the finite-T and $T = 0$ expressions for a given quantity X:

$$X_{\rm th} = X(n_i, n_j, T) - X(n_i, n_j, 0). \tag{47}$$

For Skyrme-like models, we refer the reader to Sec. V of Ref. [71], where explicit expressions and numerical notes are provided for evaluations of the thermal state variables and response functions. Thus, our discussion below focuses on evaluations of the thermal state variables for the MDI models only.

Suppressing the symbols denoting dependencies on the baryon density n and proton fraction x for brevity, the thermal energy is given by

$$E_{\rm th} = E(T) - E(0), \tag{48}$$

where $E(T) = \mathcal{H}(T)/n$ is calculated using Eqs. (6)–(13) in Sec. II A, and $E(0) = \mathcal{H}(0)/n$ is obtained from Eqs. (25)–(27) in Sec. II B.

Likewise, the thermal pressure is

$$P_{\rm th} = P(T) - P(0), \tag{49}$$

where $P(T)$ and $P(0)$ are calculated using Eq. (17) in Sec. II A. Details regarding the numerical evaluation of the chemical potentials at finite T are described in Sec. II A in connection with Eq. (13) and the discussion thereafter. Utilizing these results, the thermal chemical potentials are given by

$$\mu_{\rm th} = \mu(T) - \mu(0). \tag{50}$$

The entropy per baryon $S = s/n$ issues from Eq. (14) of Sec. III A, the specific heats at constant volume and pressure, C_V and C_P, from Eqs. (18) and (19), respectively, of the same section.

The question arises as to what plays the role of the degeneracy parameter for a general momentum-dependent interaction. The exposition below is for a one-component system. Generalization to the two-component case is straightforward. For the MDI model, the single-particle spectrum in Eq. (10) can be written as

$$\epsilon_p = \frac{p^2}{2m} + U(n,p) = \frac{p^2}{2m} + R(n,p;T) + \mathcal{U}(n), \tag{51}$$

where the explicit p dependence arising from finite range interactions is contained in $R(n,p;T)$ and $\mathcal{U}(n)$ is a density-dependent, but p-independent term from interactions that are local in space. For a given n at fixed T, the chemical potential μ is determined from Eq. (7) using an iterative procedure as outlined earlier. At finite T, the term R acquires a T dependence (see, e.g., Fig. 1), which has been explicitly indicated. We can write

$$\begin{aligned}\epsilon_p - \mu &= \frac{p^2}{2m} + R(n,p;T) - [\mu - \mathcal{U}(n)] \\ &= \frac{p^2}{2m} + R(n,p;T) - R(n,p=0;T) \\ &\quad - [\mu - \{\mathcal{U}(n) + R(n,p=0;T)\}],\end{aligned} \tag{52}$$

where in the last step we have isolated the p-independent, but n- and T-dependent part $R(n,p=0;T)$ and grouped it with $\mathcal{U}(n)$. Note that $R(n,p=0;T)$ provides an n- and T-dependent pedestal for the momentum dependence of $R(n,p;T)$. As a result,

$$\frac{\epsilon_p - \mu}{T} = \frac{1}{T}\left\{\frac{p^2}{2m} + R(n,p;T) - R(n,p=0;T)\right\} - \eta, \tag{53}$$

with

$$\eta = \frac{1}{T}[\mu - \{\mathcal{U}(n) + R(n,p=0;T)\}], \tag{54}$$

which serves as the degeneracy parameter. The term $R(n,p;T)$, when combined with $p^2/(2m)$, generates an effective mass m^*. For free gases, $R(n,p;T=0) = 0$ and $\mathcal{U}(n) = 0$ so that $\eta = \mu/T$.

For Skyrme interactions, $R(n,p;T) = \beta \times np^2/(2m)$, where β is an interaction strength-dependent constant.

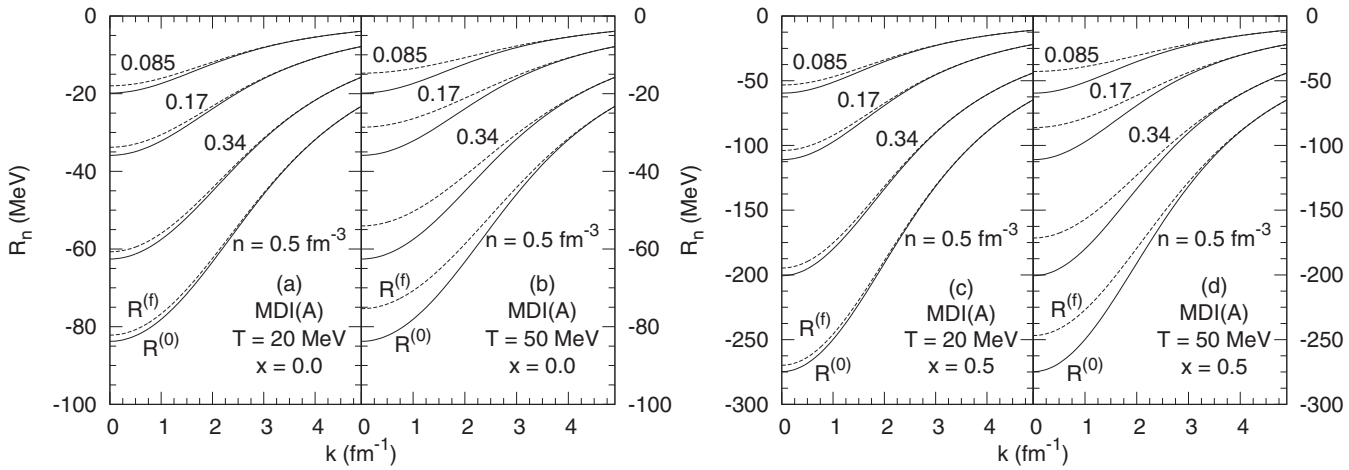

FIG. 8. Momentum-dependent part of the neutron single-particle potential for the baryon densities, temperatures, and proton fractions indicated in each panel. The zeroth approximation $R^{(0)}$ is the zero-temperature R_n given by the momentum-dependent terms in Eq. (34), whereas the final result $R^{(f)}$ is found via an iterative procedure using Eq. (13).

Combined with the $p^2/(2m)$ term, the p-dependent part of ϵ_p can be written as $p^2/(2m^*)$, with $m^* = m(1+\beta n)^{-1}$ being a density-dependent, but T-independent, effective mass. Thus,

$$\eta = \frac{\mu - \mathcal{U}(n)}{T} \quad \text{for Skyrme interactions.} \tag{55}$$

A. Results of numerical calculations

For given n, x, and T, the chemical potentials μ_n and μ_p for the MDI(A) model can be calculated using the iterative procedure described earlier in connection with Eq. (13). This entails a self-consistent determination of $R_n(p)$ and $R_p(p)$, results for which are shown in Fig. 8 for pure neutron matter and isospin-symmetric nuclear matter at various densities, and temperatures of $T = 20$ and 50 MeV, respectively. In few iterations, convergence is reached from the starting guess $R^{(0)}$ at $T = 0$ to the final result $R^{(f)}$ shown in panels (a) through (d) of this figure. As expected, substantial corrections to the zero-temperature result at low to intermediate momenta are evident as the temperature increases.

The thermal chemical potentials of the neutron $\mu_{n,\mathrm{th}}$ are shown in Fig. 9. Both models predict that the $\mu'_{n,\mathrm{th}}$s of symmetric matter and pure neutron matter cross with the latter having a larger value at low densities. The density at which the crossing occurs is smaller in the case of MDI(A) than that of SkO′. Larger temperatures move the crossing to larger densities. For pure neutron matter the two models predict nearly the same result at all densities and temperatures. The saturating behavior in both models is a consequence of progressively increasing degeneracy of the fermions and its onset occurs at higher densities for the higher temperature.

Contours of the degeneracy parameter η are shown in Fig. 10. While the qualitative trends are similar for the MDI(A) and SkO′ models, quantitative differences exist in the degenerate regime for $\eta > 1$. The origin of these differences can be traced to the different behaviors of the effective masses in the two models.

The thermal energy per baryon from the MDI(A) and SkO′ models are shown as functions of baryon density in Figs. 11(a) and 11(b). At $T = 20$ MeV, the MDI(A) model has somewhat lower values than those of the SkO′ model beyond nuclear densities for symmetric nuclear matter ($x = 0.5$). However, results of the two models agree to well beyond the nuclear density for pure neutron matter ($x = 0$), significant differences occurring only for densities beyond those shown in the figure. An opposite trend is observed at $T = 50$ MeV, for which the two models differ slightly around nuclear densities for $x = 0.5$, whereas they yield similar results for $x = 0$ at subnuclear densities. We attribute these behaviors to the significantly different behaviors of the effective masses (both their magnitudes and density dependencies) in these two models (see Fig. 3) as our analysis in the subsequent section, where analytical results in the limiting cases of degenerate and nondegenerate matter are compared with the exact results, shows.

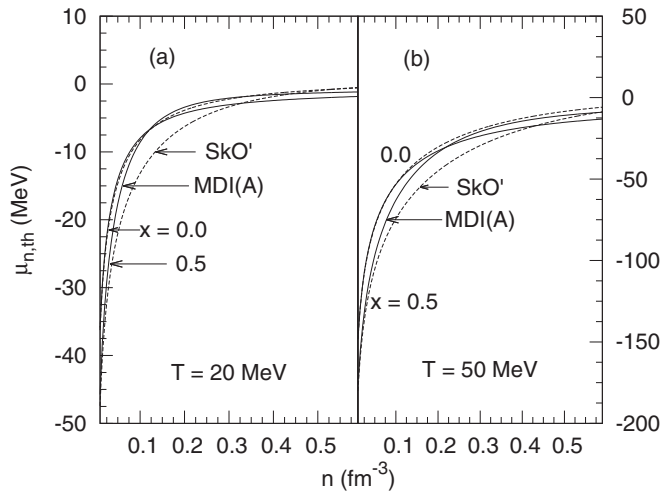

FIG. 9. Thermal chemical potentials vs n for the MDI(A) and SkO′ models from Eq. (7).

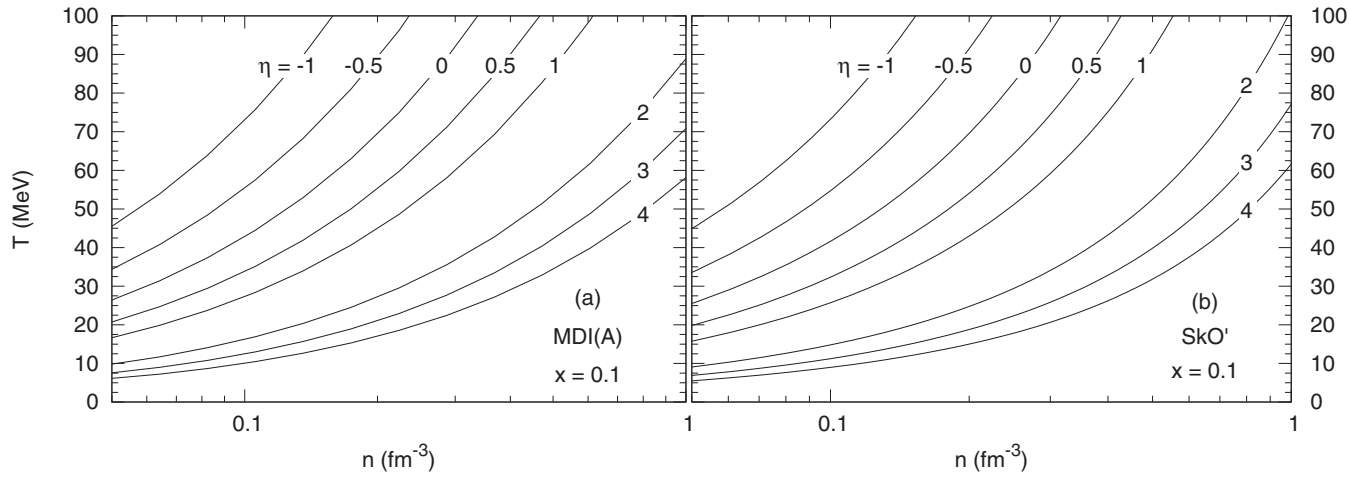

FIG. 10. Degeneracy parameter η in the n-T plane. Results are from Eq. (54) [for MDI(A)] and Eq. (55) [for SkO′].

The thermal free energy per baryon is shown in Fig. 12 as a function of baryon density for the MDI(A) and SkO′ models. Results for the two models are indistinguishable at low densities ($n < 0.01$ fm^{-3}). This low-density agreement between the two models improves with increasing temperature and with lower proton fractions. For $n > 0.01$ fm^{-3}, quantitative differences between the two models are attributable to the different trends with density of the nucleon effective masses. These differences become increasingly small for all proton fractions as the limit of extreme degeneracy is approached at very high densities.

In Fig. 13, we present the thermal pressures vs density. For both temperatures and proton fractions shown, the two models display similar traits in that at around nuclear and subnuclear densities they predict similar values, but begin to differ substantially at supranuclear densities. With increasing density, the thermal pressure of the MDI(A) model is smaller than that of the SkO′ model chiefly due to its smaller effective mass and relatively flat variation with density.

Figure 14 shows the entropy per baryon for the two models. The two models agree at low densities with the best agreement occurring for pure neutron matter up to about twice the nuclear density. At larger densities the MDI(A) model predicts that the entropy of symmetric matter converges to that of pure neutron matter. This feature is also present in SkO′ but occurs at larger densities than shown here.

Isentropic contours in the n-T plane are shown in Fig. 15 for a proton fraction of 0.1 and entropies in the range 0.25–3. Both models show similar trends in that all contours rise quickly until around $n_0/2$, beyond which only a moderate increase in the temperature is observed. For each entropy contour, the temperature is systematically larger for the SkO′ model when compared with that of the MDI(A) model. For densities larger than $2n_0$ and for values of entropy exceeding 1.5, the temperatures predicted by both models are well in excess of 50 MeV.

The specific heat at constant volume, C_V, is plotted as a function of baryon density in Fig. 16 for the two models. Noteworthy features at both temperatures are the peaks occurring at values in excess of 1.5 (the maximum

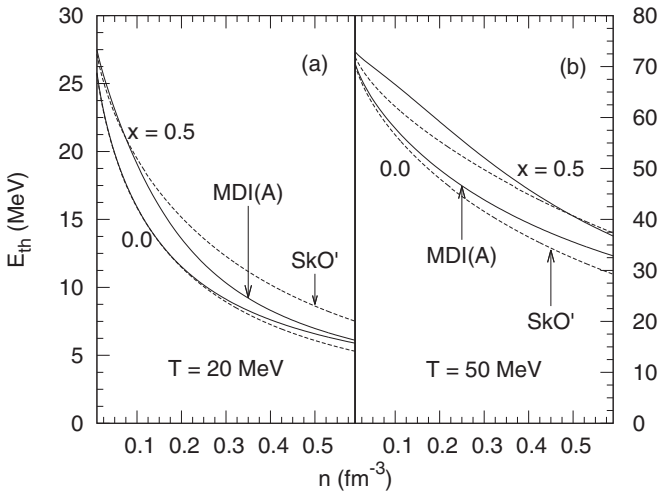

FIG. 11. Thermal energy per particle vs n for the MDI(A) and SkO′ models from Eqs. (6) and (39).

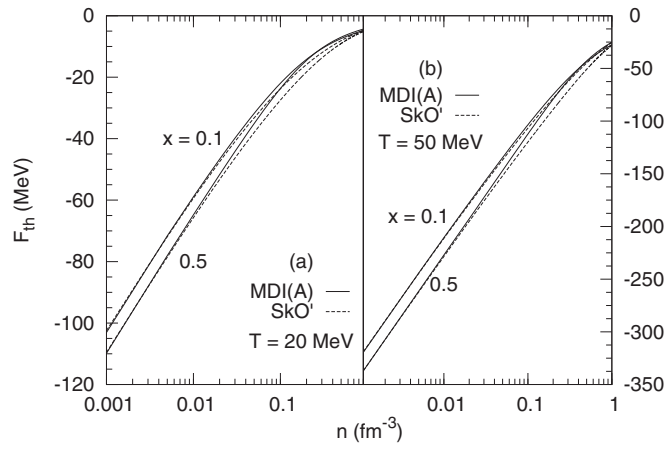

FIG. 12. Thermal free energy for the MDI(A) and SkO′ models from Eqs. (6), (39), and (14).

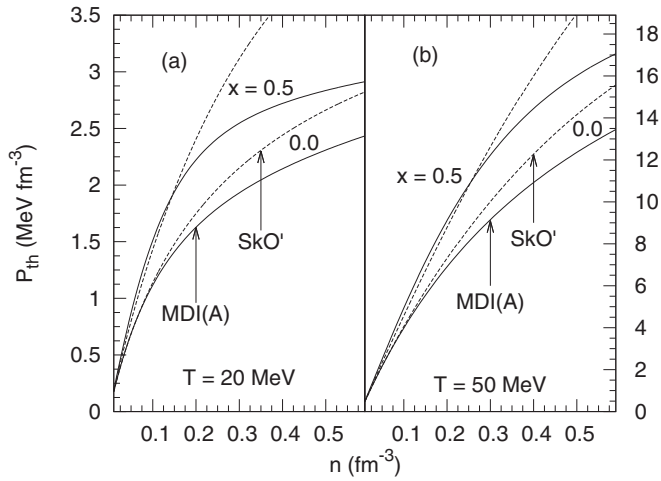

FIG. 13. Thermal pressure vs n for the MDI(A) and SkO′ models from Eq. (16).

value characteristic of free Fermi gases at vanishing density, which is also the case for Skyrme models) at finite densities in the MDI(A) model. These peaks can be attributed to the momentum dependence built into the interaction which produces a temperature-dependent spectrum via $R(n,p)$. This trait, shared with relativistic mean-field models (although there the T dependence in the spectrum enters through the Dirac effective mass) [90], has implications related to the hydrodynamic evolution of a core-collapse supernova in that C_V controls the density at which the core rebounds. C_V decreases with increasing density and the magnitude of the decrease is larger at the lower temperature. As was the case for the entropy per baryon, the C_V's of nuclear and neutron matter approach each other at large densities.

The specific heat at constant pressure, C_P, is shown in Fig. 17 as a function of baryon density. The predominant feature for both models is the sharp rise in C_P for symmetric nuclear matter at $T = 20$ MeV. This feature arises from the

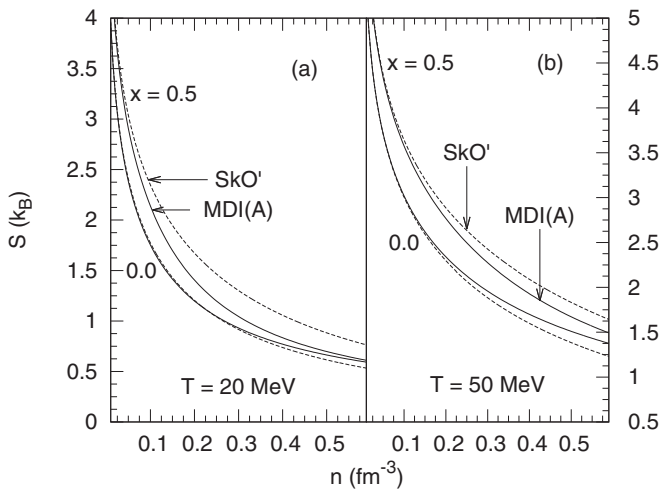

FIG. 14. Entropy per particle vs n for the MDI(A) and SkO′ models from Eq. (14).

temperature being close to that for the onset of the liquid-gas phase transition for which $dP/dn = 0$. At high densities C_P resembles the behaviors seen for C_V and the entropy per baryon.

Figure 18 shows the ratio of specific heats C_P/C_V vs n for $T = 20$ and 50 MeV, respectively, for the two models. In (a), the large variations seen at subsaturation densities for values of x not too close to that of pure neutron matter are attributable to the proximity of an incipient liquid-gas phase transition. C_P/C_V is closely related to the adiabatic index, Γ_S, which provides a measure of the stiffness of the equation of state. In addition, it also determines the speed of adiabatic sound-wave propagation in hydrodynamic evolution of matter.

B. Analytical results in limiting cases

In the cases when degenerate (low T, high n such that $T/E_{F_i} \ll 1$) or nondegenerate (high T, low n such that $T/E_{F_i} \gg 1$) conditions are met, generally compact analytical expressions can be derived. As the densities and temperatures encountered in the thermal evolution of supernovae, neutron stars, and binary mergers vary over wide ranges, matter could be in the degenerate, partially degenerate, or nondegenerate limits depending on the ambient conditions. A comparison of the exact, but numerical, results with their analytical counterparts not only allows for a check of the often involved numerical calculations, but is also helpful in identifying the density and temperature ranges in which matter is in one or the other limiting case. Because of the varying concentrations of neutrons, protons, and leptons, one or the other species may lie in different regimes of degeneracy.

1. Degenerate limit

In this case, we can use Landau's Fermi liquid theory (FLT) [91,92] to advantage. The explicit forms of the entropy density, thermal energy, thermal pressure, and thermal chemical potential are

$$s = 2T\sum_i a_i n_i, \quad E_{\rm th} = \frac{T^2}{n}\sum_i a_i n_i, \tag{56}$$

$$P_{\rm th} = \frac{2T^2}{3}\sum_i a_i n_i\left(1 - \frac{3}{2}\frac{n}{m_i^*}\frac{\partial m_i^*}{\partial n}\right), \tag{57}$$

$$\mu_{i,\rm th} = -T^2\left(\frac{a_i}{3} + \sum_j \frac{n_j a_j}{m_j^*}\frac{\partial m_j^*}{\partial n_i}\right), \tag{58}$$

where $a_i = \frac{\pi^2}{2}\frac{m_i^*}{p_{Fi}^2}$ is the level density parameter. In this limit, to lowest order in temperature, $C_V = C_P = s/n$. The above relations are quite general in character and highlight the importance of concentrations, effective masses, and their density derivatives (which, in turn, depend on the single-particle spectra) of the various constituents in matter.

2. Nondegenerate limit

Nondegenerate conditions prevail when the fugacities $z_i = e^{\mu_i/T}$ are small. Methods to calculate the state variables in this limit for Skyrme-like models have been amply discussed in

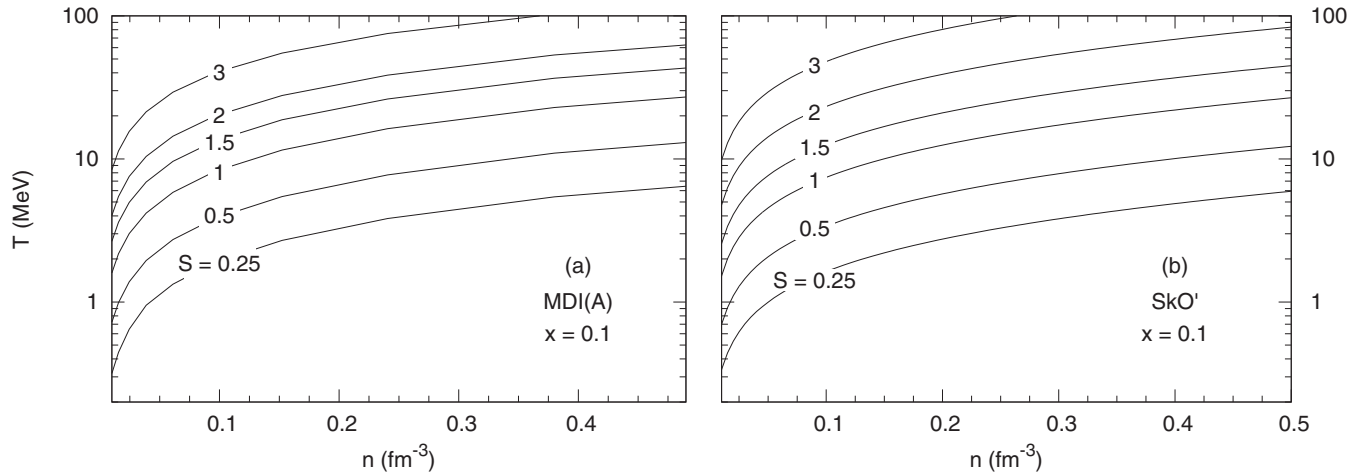

FIG. 15. Isentropes in the n-T plane for the MDI(A) model in (a) and those for the SkO′ model in (b).

the literature (see, e.g., Ref. [71] for a recent compilation of the relevant formulas). For the MDI models in which the single-particle spectrum receives significant contributions from momentum-dependent interactions, we have developed a method involving next-to-leading order steepest descent calculations that provides an adequate description of the various state variables (see Appendix B for details). The numerical results presented below for the nondegenerate limit are obtained employing the relations in Appendixes B and C.

C. Numerical vs analytical results

In this section, the exact numerical results of Sec. V are compared with those using the analytical formulas in the degenerate and nondegenerate limits described in the previous section. Figure 19 contains plots of the exact thermal chemical potential of the neutron and its degenerate and nondegenerate limits. The agreement between the nondegenerate limit and the exact result is significantly better for SkO′ compared with MDI(A). This is best seen in the $T = 50$ MeV results for pure neutron matter for which the nondegenerate limit coincides with the exact result until about $2n_0$ for SkO′ compared with MDI(A), which agrees only to about n_0. Both models predict convergence between the degenerate and exact results beginning at around $2n_0$ for $T = 20$ MeV and around $4n_0$ for $T = 50$ MeV.

The exact thermal energy and its limits from the two models are shown in Fig. 20. The MDI(A) model has a thermal energy that agrees with its nondegenerate limit for similar densities compared to that for the SkO′ model. For both models the agreement between the exact result and the nondegenerate limit is better at high temperatures and for pure neutron matter. Agreement between the degenerate limit and the exact solution occurs sooner (lower density) for MDI(A) than for SkO′. In both cases, the best agreement is for lower temperatures and for symmetric nuclear matter. Note, however, that around nuclear densities, matter is in the semidegenerate limit, as was the case for APR and Ska models in Ref. [71].

In Fig. 21, we present the thermal pressure and its limiting cases. For both models the nondegenerate limit agrees with the

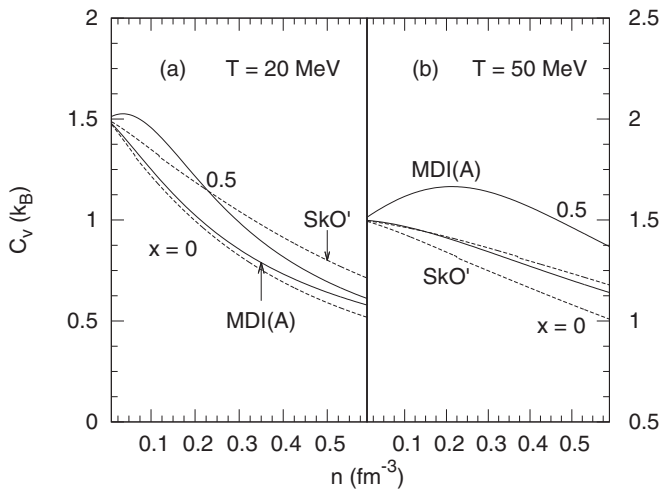

FIG. 16. (a),(b) Specific heat at constant volume C_V vs density from Eq. (18) for the MDI(A) and SkO′ models.

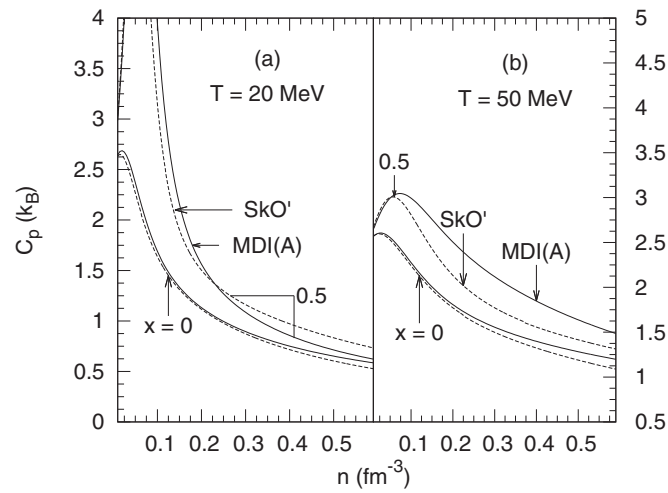

FIG. 17. (a),(b) Specific heat at constant pressure C_P vs density from Eq. (19).

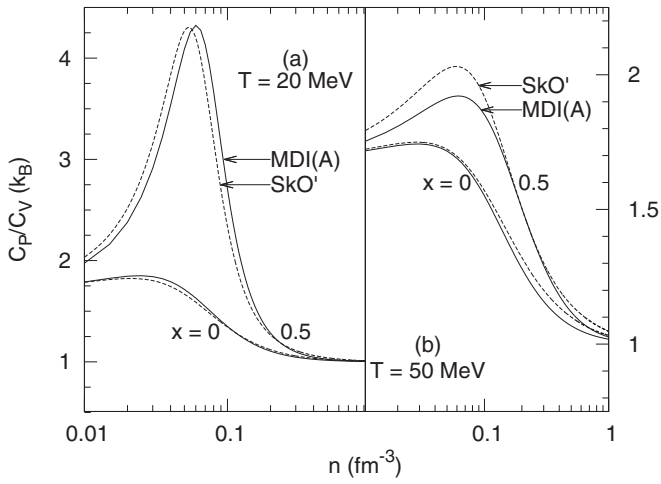

FIG. 18. Ratio of specific heats.

exact result until about n_0 at 20 MeV [panels (a) and (c)] and until $3n_0$ for $T = 50$ MeV [panels (b) and (d)]. The agreement is better at high temperatures and for symmetric matter than for pure neutron matter. At both temperatures and proton fractions, the degenerate limits come closer to the exact results using the MDI(A) model.

In Fig. 22 we present the entropy per baryon and its degenerate and nondegenerate limits. The nondegenerate limit has the best agreement using SkO′ for symmetric nuclear matter at $T = 50$ MeV, which extends to about $3n_0$. The range of densities over which the MDI(A) model agrees with the exact result is smaller than that for SkO′. For symmetric nuclear matter, for example, the agreement does not extend beyond about 1–1.5 n_0 even at 50 MeV. The degenerate limit coincides with the exact solution starting approximately around $2n_0$ for the MDI(A) model for symmetric nuclear matter at $T = 20$ MeV. The SkO′ model does notably worse with its best agreement not occurring until $3n_0$–$4n_0$ for pure neutron matter at $T = 20$ MeV.

Some insight into the behaviors of the thermal variables presented above can be gained from the asymptotic behaviors of the single-particle potentials at high momenta in the two models which lead to two noteworthy effects: (1) The earlier onset of degeneracy in the MDI model compared to that for SkO′ is attributable to weaker binding at high densities and (2) the MDI nucleon effective masses that are nearly independent of density at high density (while qualitatively the isospin splitting is similar to that of SkO′) cause the thermal state variables to exhibit less sensitivity to the proton fraction being changed (cf. FLT equations with $\partial m^*/\partial n \to 0$).

The specific heat at constant volume vs baryon density and its limiting cases are presented in Figs. 23(a) and 23(b) for the MDI(A) model, while those for the SkO′ model are in panels (c) and (d) of the same figure. The best agreement between the results of the exact and the degenerate limit calculations occurs at low temperatures and large densities. Although this is true of both models, the agreement is better for the MDI(A) model as the degenerate limit comes far closer to the exact solution than the SkO′ model. For MDI(A), the degenerate limit has better agreement with the exact solution for symmetric nuclear matter as opposed to SkO′, which shows better agreement for pure neutron matter. The nondegenerate limit coincides with the exact solution only for densities much less than the nuclear saturation density. The agreement between the nondegenerate limit and the exact result is best using the MDI(A) model for symmetric nuclear matter at high temperatures. The agreement between the nondegenerate limit and the exact result using the SkO′ model is slightly better for pure neutron matter and at high temperatures.

In Fig. 24 we display the specific heat at constant pressure vs baryon density from the MDI(A) [panels (a) and (b)] and SkO′ [panels (c) and (d)] models. The agreement between the nondegenerate limit and the exact solution is remarkably good using the MDI(A) for pure neutron matter at high temperatures and low densities. For the MDI(A) model the agreement extends out to about 0.4 fm^{-3}, whereas for the SkO′ the agreement is up to 0.3 fm^{-3} for symmetric or pure neutron matter at high temperatures. The agreement between

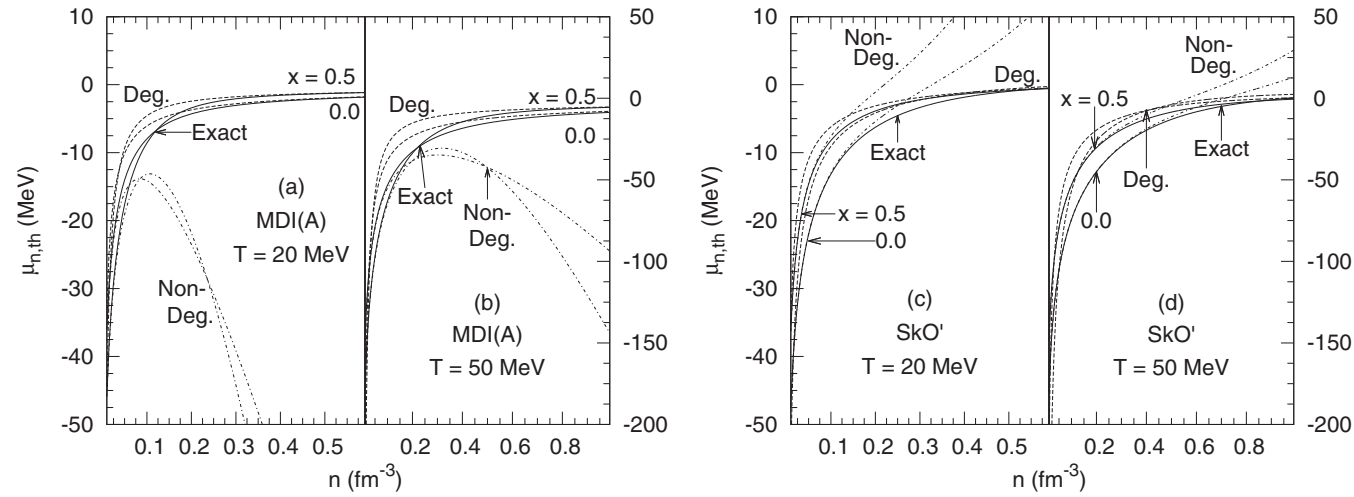

FIG. 19. Neutron thermal chemical potentials [Eq. (7)] vs n for the MDI(A) model in (a) and (b) and the SkO′ model in (c) and (d) compared with their limiting cases from Eqs. (58) and (B20).

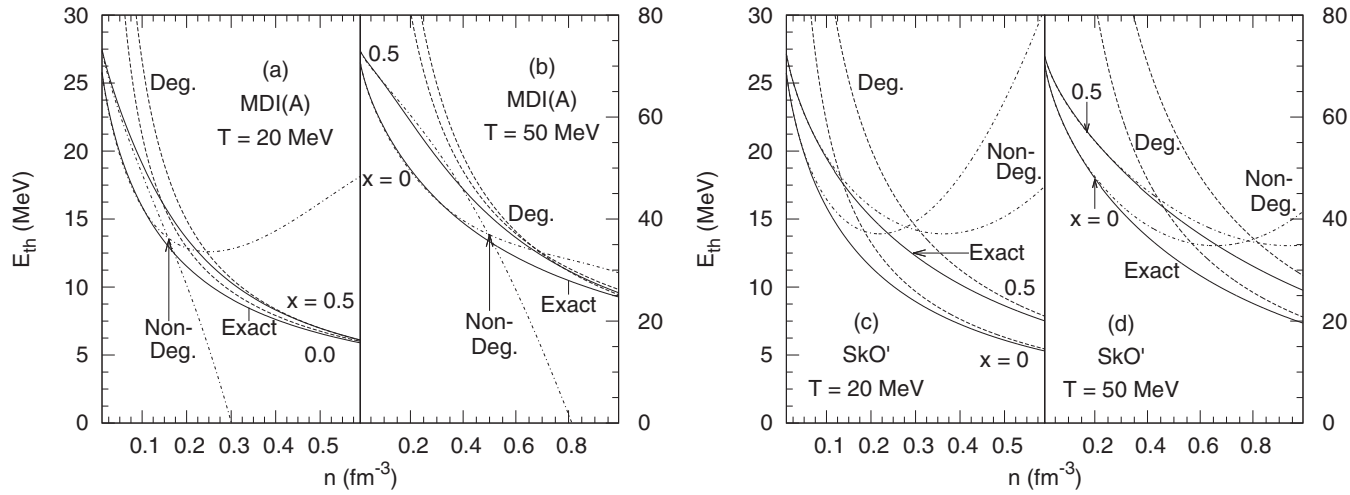

FIG. 20. Thermal energy per particle [Eq. (6)] and limiting cases [Eqs. (56) and (B30)] vs n.

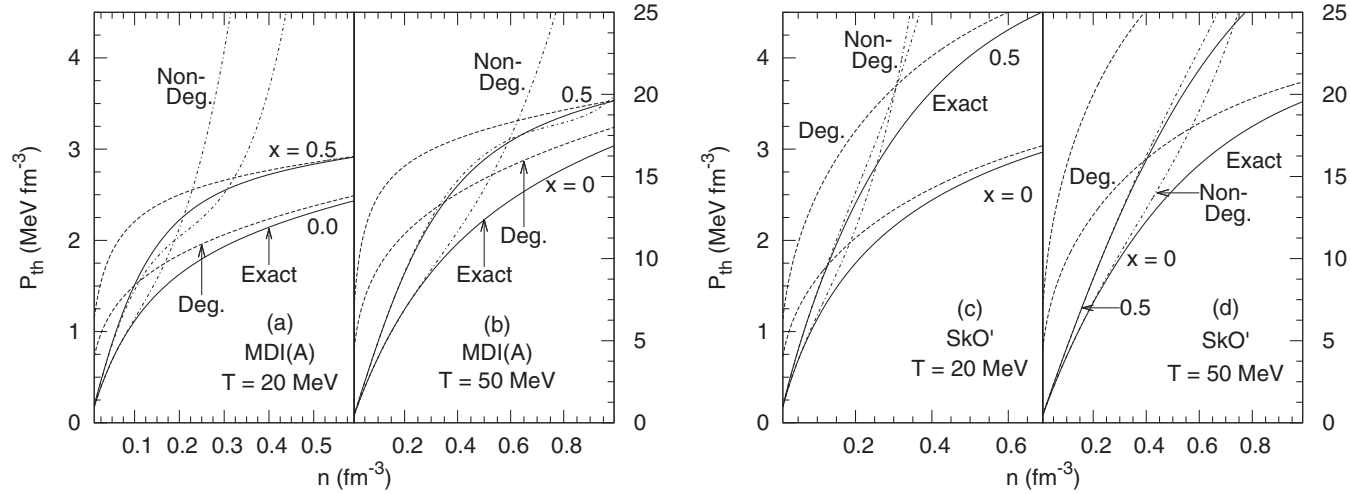

FIG. 21. Thermal pressure [Eq. (16)] and limiting cases [Eqs. (57) and (B35)] vs n.

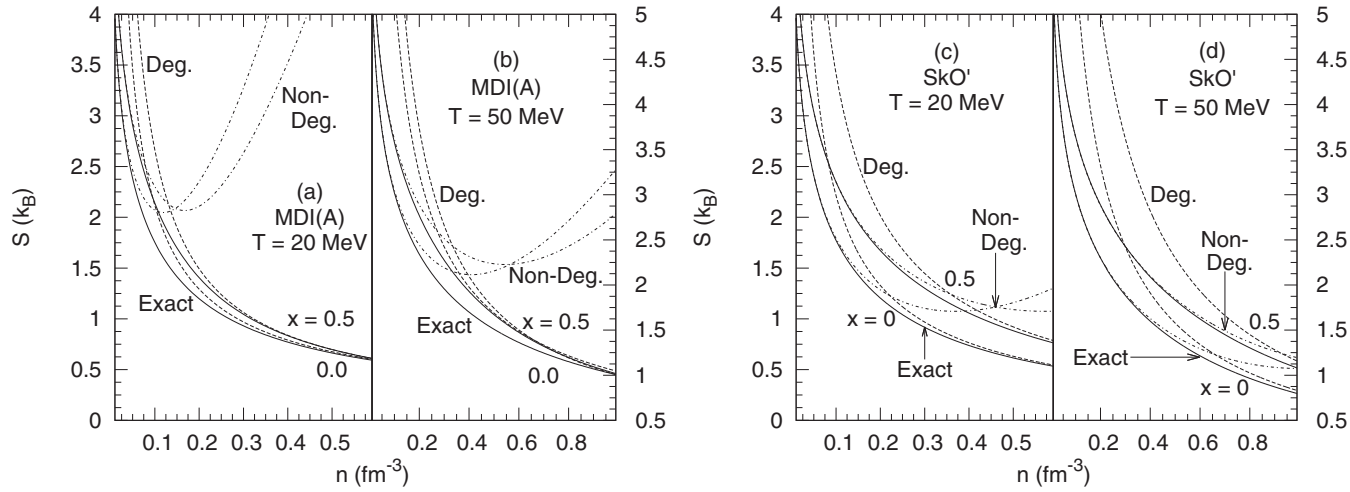

FIG. 22. Entropy per particle [Eq. (14)] vs n for the MDI(A) model in (a) and (b) and the SkO′ model in (c) and (d) compared with their limiting cases from Eqs. (56) and (B34).

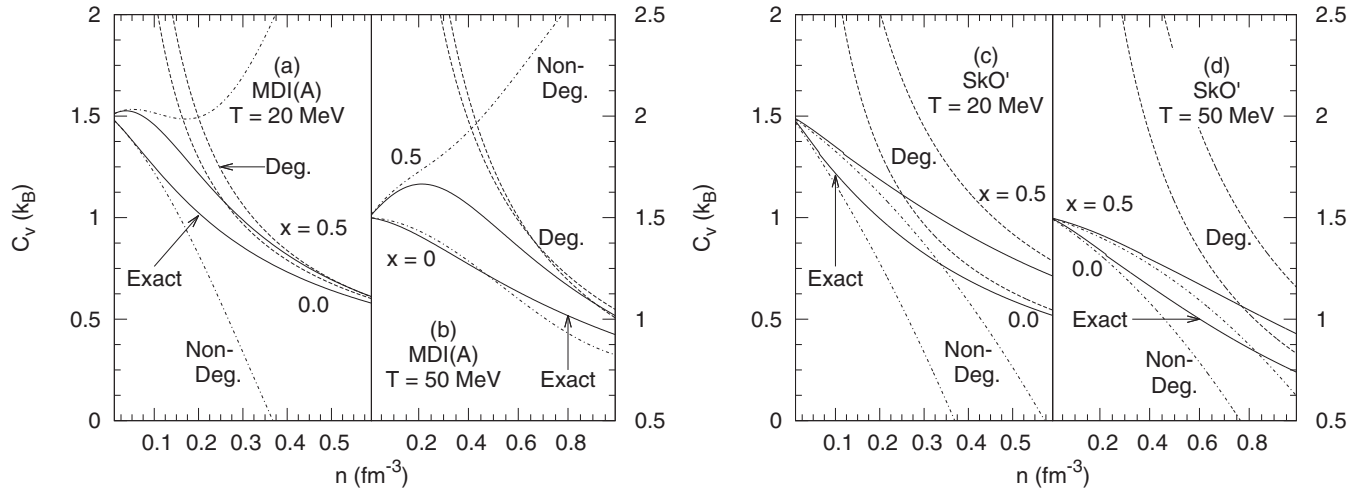

FIG. 23. Specific heat at constant volume C_V for the MDI(A) model in (a) and (b) and the SkO′ model in (c) and (d) compared with their limiting cases from Eq. (56) as $S = C_V$ in the degenerate limit, and Eq. (C23).

the degenerate limit and the exact result for C_P is best for the MDI(A) model for pure neutron matter at large densities and low temperatures. For the SkO′ model, the agreement between the degenerate limit and the exact solution is better for pure neutron matter at large densities and low temperatures.

VI. THERMAL AND ADIABATIC INDICES

The paradigm for neutron star mergers now seems to be that one begins with two 1.3–1.4 $M_G/M_\odot$ stars, which form a hypermassive remnant stabilized against collapse by rotation, thermal, and magnetic effects. It could be differentially rotating. Loss of differential rotation and loss of thermal and/or magnetic support lead to an eventual collapse to a black hole. The time scale is very important, as it will have observable effects on gravitational-wave and γ-ray burst durations. Thermal effects at supranuclear density seem to have little effect, but rotational support means the average densities of the disk are near saturation density where the thermal effects become substantial (see references below). Thus, the thermal support needs to be properly treated.

A. Thermal index

The inclusion of thermal effects in neutron star merger simulations is often treated using an effective thermal index $\Gamma_{\rm th}(n)$ defined as

$$\Gamma_{\rm th}(n) = 1 + \frac{P_{\rm th}(n)}{\varepsilon_{\rm th}(n)}. \tag{59}$$

Shibata's group commonly uses $\Gamma_{\rm th}$ to describe finite-temperature effects, favoring the value 1.8 [93]. Bauswein *et al.* [94] prefer the value 2.0; see also Janka *et al.* [95]. In simulations by Foucart *et al.* [96] and Kaplan *et al.* [63] conditions such as $S = 5$ at 10^{14} g cm^{-3} and $S = 10$ at 10^{12} g cm^{-3} are reached in the ejecta. In these works, realistic

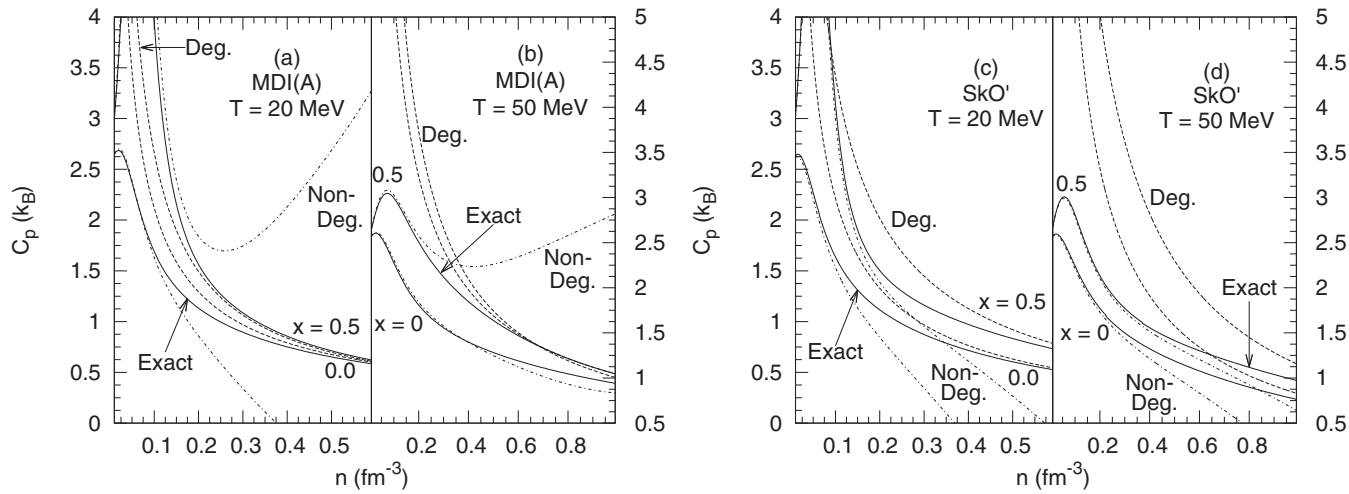

FIG. 24. Specific heat at constant pressure C_P for the MDI(A) model in (a) and (b) and the SkO′ model in (c) and (d) compared with their limiting cases from Eq. (56) as $S = C_P$ in the degenerate limit, and Eq. (19).

EOSs with consistent thermal treatments (LS [1] or Shen [64], among others) are used.

Our aim here is to provide a basis for understanding the behavior of $\Gamma_{\rm th}$ from elementary considerations. The results of our calculations are relevant only for densities and temperatures for which a bulk homogeneous phase will be present. Inhomogeneous phases present at subnuclear densities, and which induce large variations in $\Gamma_{\rm th}$, have not been considered here as they lie beyond the scope of this work.

In the degenerate limit, the FLT results in Eqs. (56) and (57) imply that

$$\Gamma_{\rm th}(n) = 1 + \frac{2}{3}\frac{\sum_i a_i n_i Q_i}{\sum_i a_i n_i}, \quad i = n,p,e, \tag{60}$$

where the level density parameters are

$$a_i = \left\{ \begin{array}{ll} \frac{\pi^2 m_i^*}{2p_{F_i}^2}, & \text{nonrelativistic nucleons} \\ \frac{\pi^2\sqrt{p_{F_e}^2+m_e^2}}{2p_{F_e}^2} & \text{relativistic electrons} \end{array} \right\}, \tag{61}$$

and

$$Q_i = 1 - \frac{3}{2}\frac{n}{m_i^*}\frac{dm_i^*}{dn}. \tag{62}$$

The above equations highlight the role of the effective masses and their behavior with density. Note that relativity endows noninteracting electrons with a density-dependent effective mass $m_e^* = E_{F_e} = \sqrt{p_{F_e}^2 + m_e^2}$. Thus, in a pure electron gas,

$$Q_e = 1 - \frac{1}{2}\frac{p_{F_e}^2}{p_{F_e}^2 + m_e^2}, \tag{63}$$

which has the limit 1/2 for ultrarelativistic electrons ($p_{F_e} \gg m_e$) and 1 for nonrelativistic electrons ($p_{F_e} \ll m_e$). These limits help to recover the well-known results $\Gamma_{\rm th} = 4/3$ in the former case and 5/3 in the latter (also easily obtained by inspecting the limits of $P_{\rm th}/\varepsilon_{\rm th}$ in the two cases).

Note that in the degenerate limit, $\Gamma_{\rm th}$ in Eq. (60) is independent of temperature. For pure neutron matter (PNM) and symmetric nuclear matter (SNM) without electrons, Eq. (60) reduces to the simple result

$$\Gamma_{\rm th}(n) = \frac{5}{3} - \frac{n}{m_b^*}\frac{dm_b^*}{dn}, \tag{64}$$

where the subscript "b" identifies the appropriate baryons (neutrons in PNM and neutrons and protons in SNM or isospin-asymmetric matter).

For Skyrme models, the above relation is valid for all regions of degeneracy as $P_{\rm th}$ and $\varepsilon_{\rm th}$ can be written in terms of their ideal gas counterparts [calculated with $m^*(n)$ instead of m] as

$$\begin{aligned} P_{\rm th}(n,T) &= P_{\rm th}^{id}(n,T;m^*)\left(1 - \frac{3}{2}\frac{n}{m^*}\frac{dm^*}{dn}\right) \\ \varepsilon_{\rm th}(n,T) &= \varepsilon_{\rm th}^{id}(n,T;m^*), \quad \frac{P_{\rm th}^{id}}{\varepsilon_{\rm th}^{id}} = \frac{2}{3}. \end{aligned} \tag{65}$$

These results in conjunction with Eq. (59) lead to Eq. (64). The simple form of the effective masses in Skyrme models, $m^* = m(1+\beta n)^{-1}$, where the positive constant β depends mildly on the proton fraction (for the SkO′ model, β lies in the range 0.523–0.724 as Y_p varies from 0 to 0.5) allows us to obtain

$$\Gamma_{\rm th}(n) = \frac{5}{3} + \frac{\beta n}{1+\beta n} = \frac{8}{3} - \frac{m^*}{m}, \tag{66}$$

which establishes the T independence and very mild dependence on the proton fraction. For Skyrme models, therefore, $\Gamma_{\rm th}$ of nucleons increases monotonically from 5/3 to 8/3 as the density increases.

The analytical expressions for the effective masses and their derivatives with respect to density are more complicated for the MDI models than those for the Skyrme models (see Appendix A). However, they are easily implemented in numerical calculations. In the Maxwell-Boltzmann limit [that is, the nondegenerate limit to $\mathcal{O}(z^1)$], the thermal energy density and pressure of the MDI model are

$$\begin{aligned} \varepsilon_{\rm th} &= \frac{3nT}{2}\exp\left[\frac{R(\sqrt{2mT}) - R(\sqrt{4mT})}{T}\right] \\ &\quad + \frac{n}{2}R(\sqrt{2mT}) - \frac{3}{5}\mathcal{T}_F n, \end{aligned} \tag{67}$$

$$P_{\rm th} = nT\left[1 + \frac{R(\sqrt{2mT})}{2T}\right] - \frac{2}{5}\mathcal{T}_F n, \tag{68}$$

where $R(p)$ is given by Eq. (B12) with $p_{0R} = \sqrt{2mT}$ and $\mathcal{T}_F = p_F^2/(2m^*)$. As in this regime the interactions are weak due to the diluteness of the system, we expand the exponential in Eq. (67) in a Taylor series about the zero of its argument, which leads to

$$\varepsilon_{\rm th} = \frac{3nT}{2}\left[1 + \frac{4/3R(\sqrt{2mT}) - R(\sqrt{4mT})}{T}\right] - \frac{3}{5}\mathcal{T}_F n. \tag{69}$$

Note that in Eqs. (68) and (69) the leading terms are proportional to nT, the interaction terms to n^2/T^2 (approximately), and the $T = 0$ terms to $n^{5/3}$. Thus, in the limit of vanishing density, the ratio $P_{\rm th}/\varepsilon_{\rm th}$ goes to 2/3; consequently, $\Gamma_{\rm th}$ approaches 5/3 as expected for a nonrelativistic gas.

To appreciate the role of electrons in the behavior of $\Gamma_{\rm th}$ vs n, we first show in Fig. 25 results with nucleons only for three different models. Proton fractions and temperatures are as noted in the figure. Results for the nonrelativistic models in this figure are for MDI(A) and SkO′ used throughout this work. For contrast, we also show results for a typical relativistic mean-field theoretical model (labeled MFT in the figure) with up to quartic scalar self-interactions. The strength parameters of this MFT model yield the zero-temperature properties of $n_0 = 0.155$ fm^{-3}, $E_0 = 16$ MeV, $M^*/M = 0.7, K_0 = 222$ MeV, $S_2 = 30$ MeV, and $L = 87.0$ MeV. We have restricted ourselves to the standard MFT model as the $T \neq 0$ results with nonlinear derivatives in MFT models [40] are in progress and those with two-loop effects [41] will be published separately.

In the nondegenerate regime, the exact numerical results in all cases shown tend to 5/3, as expected. Also shown in

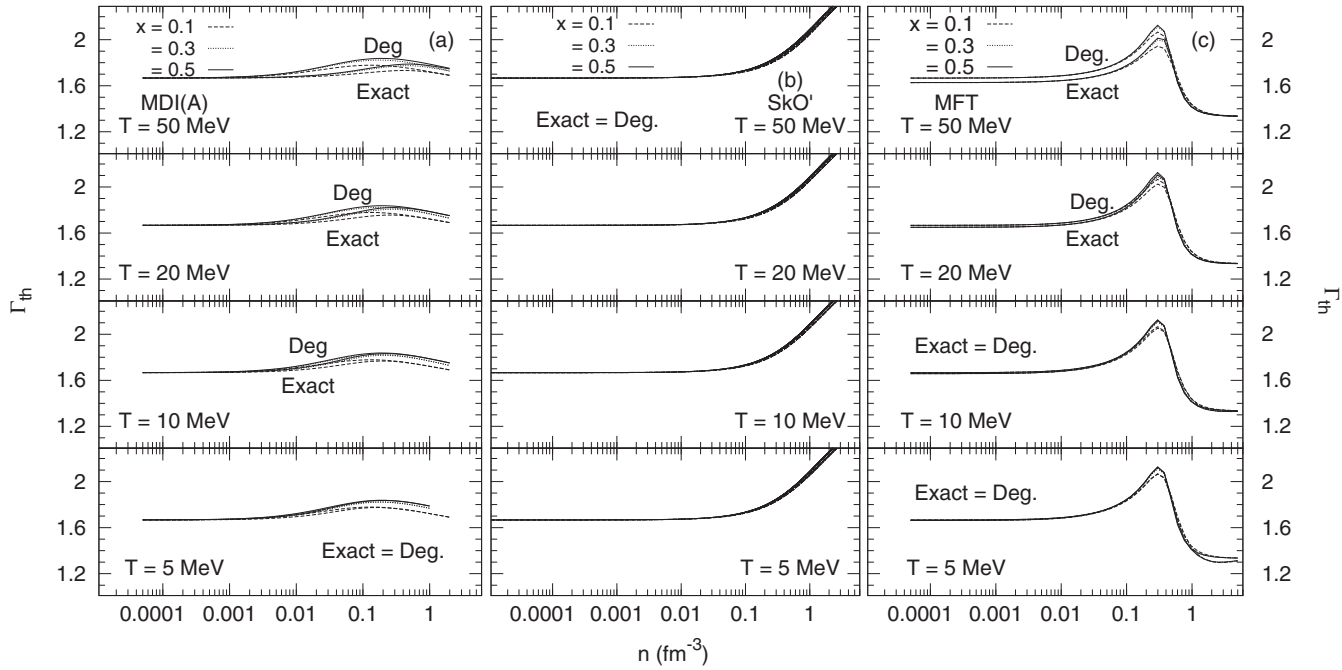

FIG. 25. The thermal index $\Gamma_{\rm th}$ vs n for the three models indicated in the figure. Results for the exact calculations are from Eqs. (48), (49), and (59), whereas those for the degenerate limit are from Eqs. (60)–(62). Results shown are for nucleons only.

this figure are results from the expression in Eq. (60), which agree very well with the exact results in the expected regions of density (that are very nearly independent of temperature) for all three models (except the MFT model at $T = 50$ MeV, to which we return below). Beginning with the nonrelativistic models, we observe a distinct difference between results for the two models in that the MDI(A) model exhibits a pronounced peak for $Y_p = x = 0.5$, whereas the SkO′ model does not. The origin of these differences can be traced back to the behavior of $m^{*\prime}$s of these models with density. The presence or absence of a peak can be ascertained by examining whether

$$\frac{d\Gamma_{\rm th}}{dn} = 0 = \frac{dm^*}{dn}\left(1 - \frac{n}{m^*}\frac{dm^*}{dn}\right) + n\frac{d^2m^*}{dn^2} = 0 \qquad (70)$$

admits a solution. For the MDI(A) model, the solution of the above equation occurs at $n \simeq 0.15$ fm^{-3} at $T = 0$, in good agreement with the exact numerical results. As T increases toward 50 MeV, the estimate from the degenerate limit no longer applies.

We turn now to analyze results of the MFT model, particularly in the degenerate region where a peak occurs for all values of Y_p. In MFT models, the Landau effective masses $m_i^* = E_{F_i}^* = \sqrt{p_{F_i}^2 + M^{*2}}$, where M^* is the Dirac effective mass obtained from a self-consistent procedure which involves minimizing the energy density (pressure at finite T) with respect to density.

Figure 26 shows M^* and m_n^* of the MFT model employed here for $T = 0$. Note that although M^* decreases monotonically with density, m_n^* exhibits a minimum and rises monotonically with density, a characteristic behavior solely attributable to relativity (at asymptotic densities, mass is overwhelmed by momentum). The density at which the minima occur is easily found from the roots of

$$\frac{p_{F_i}}{M^*} + \frac{dM^*}{dp_{F_i}} = 0 \qquad (71)$$

for each Y_p. The densities at the minima range from 0.52 to 0.57 fm^{-3} for Y_p in the range 0–0.5. This behavior of $m^{*\prime}$s is also at the root of the peaks seen in $\Gamma_{\rm th}$ vs n as the analysis below shows.

We restrict our analysis to the case of PNM as the location of the peak in $\Gamma_{\rm th}$ is not very sensitive to Y_p. The degenerate limit expressions for the thermal pressure and energy density

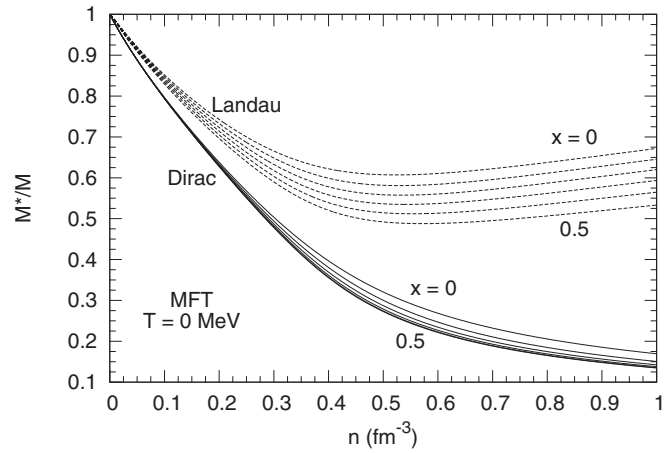

FIG. 26. The Dirac and Landau effective masses M^* and m_n^* of neutrons in a typical mean-field theoretical (MFT) model.

are [97]

$$P_{\rm th} = \frac{1}{3} naT^2 \left[1 + \left(\frac{M^*}{E_F^*} \right)^2 \left(1 - 3 \frac{n}{M^*} \frac{dM^*}{dn} \right) \right], \quad (72)$$

$$\varepsilon_{\rm th} = naT^2, \quad (73)$$

where the level density parameter $a = \pi^2 E_F^*/(2p_F^2)$. The thermal index then becomes

$$\Gamma_{\rm th} = \frac{4}{3} + \frac{1}{3} \left[\left(\frac{M^*}{E_F^*} \right)^2 \left(1 - 3 \frac{n}{M^*} \frac{dM^*}{dn} \right) \right]. \quad (74)$$

In the nonrelativistic limit, $M^*/E_F^* \to 1$ and the logarithmic derivative of M^* with respect to n tends to zero, leading to $\Gamma_{\rm th} = 5/3$. In the ultrarelativistic limit, $M^* \to 0$ so that $\Gamma_{\rm th} = 4/3$. The density at which the maximum occurs in $\Gamma_{\rm th}$ can be determined from

$$\frac{d\Gamma_{\rm th}}{dp_F} = 0 = \frac{d}{dp_F} \left(\frac{p_F^2}{E_F^{*2}} + \frac{p_F M^*}{E_F^{*2}} \frac{dM^*}{dp_F} \right). \quad (75)$$

The result is $n \simeq 0.27$ fm^{-3}, in good agreement with the exact results. Performing the appropriate calculations for neutrons and protons with Y_p in the range 0.1–0.5 yields densities in the range 0.28–0.31 fm^{-3}, also in good agreement with the exact numerical results in Fig. 25.

The $T = 50$ MeV results for the MFT model requires some explanation. Note that for densities below the peak, the exact and degenerate results are somewhat different although the qualitative trend is maintained. This is attributable to the fact that in MFT models, M^* acquires a temperature dependence with progressively increasing T, whereas the degenerate limit results are calculated with the zero-temperature M^*.

The preceding analysis sets the stage to assess the role leptons (e^- and e^+) play in determining $\Gamma_{\rm th}$. As Skyrme models lend themselves to a straightforward analysis (results for other models are similar although quantitative differences exist), we show in Fig. 27(a) the contributions from nucleons and leptons to $P_{\rm th}$ and $\varepsilon_{\rm th}$ at $T = 5$ MeV and $Y_p = 0.5$. The ratio $P_{\rm th}/\varepsilon_{\rm th}$ for

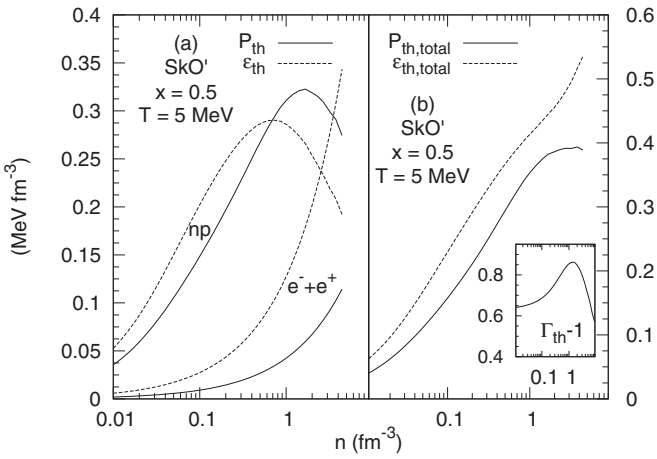

FIG. 27. (a) Contributions from nucleons and leptons to thermal pressure, $P_{\rm th}$, and thermal energy density, $\varepsilon_{\rm th}$, for the SkO′ model at the indicated proton fraction and temperature. (b) The total $P_{\rm th}$ and $\varepsilon_{\rm th}$; the inset shows their ratio.

leptons remains close to 1/3 for all densities with negligible contributions from positrons. With increasing density, the ideal gas value of $P_{\rm th}/\varepsilon_{\rm th} = 2/3$ for nucleons changes significantly due to corrections from the density dependence of m^*. From the degenerate result for $\varepsilon_{\rm th}$, it is easy to show that its maximum value is reached at $n = 1/(2\beta) \cong 0.69$ fm^{-3} using $\beta = 0.724$ fm^3 for $x = 0.5$ for this model. Use of this density yields the peak value of $\varepsilon_{\rm th} \simeq 0.29$ MeV fm^{-3}, in good agreement with the exact result. Likewise, the degenerate expression for $P_{\rm th}$ yields the density at which its peak occurs as $n = 0.5(1 + \sqrt{1.8})/\beta \cong 1.62$ fm^{-3} and a peak value of $P_{\rm th} \simeq 0.32$ MeV fm^{-3}, again in good agreement with the exact result.

Figure 27(b) shows the total thermal pressure and energy density along with its ratio in the inset. It is evident that the contributions from the leptons remain subdominant except at very low and very high densities at this temperature. With the inclusion of leptons the ratio of $P_{\rm th}/\varepsilon_{\rm th}$ is less than 1 at all densities. At large densities, the total thermal pressure approaches a constant value, whereas $\varepsilon_{\rm th}$ continues to increase. Thus, the ratio $P_{\rm th}/\varepsilon_{\rm th}$, and thereby $\Gamma_{\rm th}$, decrease at large densities, resulting in the maximum observed in the inset. The location of this maximum can be calculated by solving for the density at which

$$\frac{d}{dn} \left(\frac{2a_n Q_n + a_e Q_e}{2a_p + a_e} \right) = 0 \quad (76)$$

appropriate for SNM with $Q_n = Q_p$, $a_n = a_p$, and $n_n = n_p = n_e$. Using results from FLT, the above equation can be cast in the form

$$\frac{1}{\gamma} \frac{d\gamma}{dn} + \frac{1}{Q_n} \frac{dQ_n}{dn} = 0, \quad (77)$$

with

$$\gamma = \left(1 + \frac{Q_e m_e^*}{2Q_n m_n^*} \right) \left(1 + \frac{m_e^*}{2m_n^*} \right)^{-1}, \quad (78)$$

a relation that involves density-dependent effective masses of the neutron ($Q_n = 5/3 - m_n^*/m$) and the electron. A straightforward numerical evaluation yields the result $\simeq$1.37 fm^{-3} for the density at which the peak in $\Gamma_{\rm th}$ occurs in agreement with the exact result.

For contributions from the leptons (e^- and e^+), we adopt the JEL scheme [98] in all regions of degeneracy in our exact numerical calculations. Contributions from photons (significant at high values of T and n) are easily incorporated using

$$\varepsilon_\gamma = \frac{\pi^2}{15} \frac{T^4}{(\hbar c)^3}, \quad P_\gamma = \frac{\varepsilon_\gamma}{3}, \quad \text{and} \quad s_\gamma = \frac{4}{3} \frac{\varepsilon_\gamma}{T}. \quad (79)$$

In Figs. 28(a) and 28(b), results similar to those of Fig. 27 are shown, but at $T = 50$ MeV. Contributions from the leptons are such that $P_{\rm th}/\varepsilon_{\rm th}$ remains at 1/3 as for $T = 5$ MeV, with minimal contributions from positrons. At very low densities the nucleonic contributions are those of nearly free and nondegenerate fermions. With increasing density, however, nucleons enter the semidegenerate region for which a transparent analysis is not possible. While the qualitative features are similar to those of Fig. 27, quantitative differences are attributable to the higher temperature in this case.

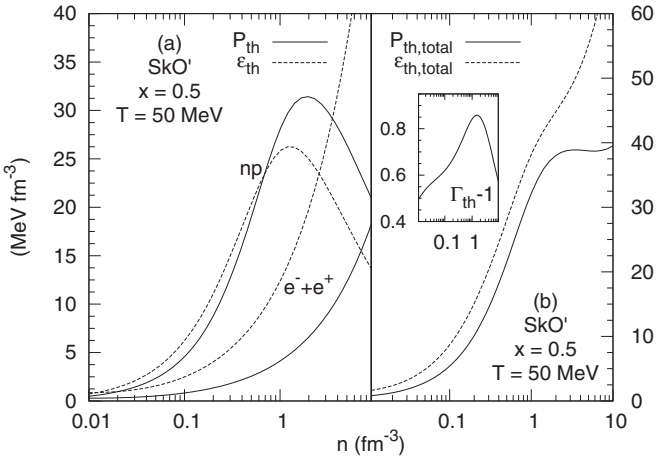

FIG. 28. Same as Fig. 27, but at $T = 50$ MeV.

Results of $\Gamma_{\rm th}$ for the three models considered in this section including the contributions from leptons and photons are shown in Fig. 29. Regions of density and temperature for which the degenerate or nondegenerate approximation is valid are apparent in this figure. Note that the behavior of $\Gamma_{\rm th}$ at supranuclear nuclear densities for the nonrelativistic models is significantly altered from the results with nucleons only (see Fig. 25 for comparison) primarily because of the contributions from leptons.

B. Adiabatic index

In hydrodynamics, compressions and rarefactions are adiabatic (that is, isentropic) rather than isothermal. The adiabatic index defined by

$$\Gamma_S = \left.\frac{\partial \ln P}{\partial \ln n}\right|_S = \frac{n}{P}\left.\frac{\partial P}{\partial n}\right|_S \tag{80}$$

is a gauge of the fractional variation of local pressure with density and hence the stiffness of the EOS. For our purposes it is more convenient to transform to the variables (n,T), which is achieved by the use of Jacobians [69]:

$$\begin{aligned}\Gamma_S &= \frac{n}{P}\frac{\frac{\partial(P,S)}{\partial(P,T)}\partial(P,T)}{\frac{\partial(n,S)}{\partial(n,T)}\partial(n,T)} \\ &= \frac{n}{P}\frac{\left.\frac{\partial S}{\partial T}\right|_P}{\left.\frac{\partial S}{\partial T}\right|_n}\frac{\partial(P,T)}{\partial(n,T)} = \frac{C_P}{C_V}\frac{n}{P}\left.\frac{\partial P}{\partial n}\right|_T .\end{aligned} \tag{81}$$

The calculation of Γ_S is facilitated by the isentropes in the n-T plane shown in Fig. 30. In contrast to the results shown in Fig. 15, contributions from leptons and photons in addition to those from nucleons are included in the results of Fig. 30. To calculate Γ_S from Eq. (81), one first selects values of (n,T) for which $S(n,T)$ is a prescribed constant. These n and T are, in turn, used to calculate P, its derivative $(\partial P/\partial n)|_T$, and the specific heats C_P and C_V. Alternatively, P can be expressed analytically as a function of (S,n) (as, for example, in the degenerate and nondegenerate limits). We have verified that these two approaches yield identical results.

In the derivation of a degenerate limit expression for Γ_S we must be mindful of the fact that even though $C_P \simeq C_V$ in FLT, the ratio C_P/C_V cannot be set equal to unity. This is because C_P and C_V are polynomials in odd powers of T in this limit, and thus

$$\frac{C_P}{C_V} = 1 + C(n)T^2 + \cdots , \tag{82}$$

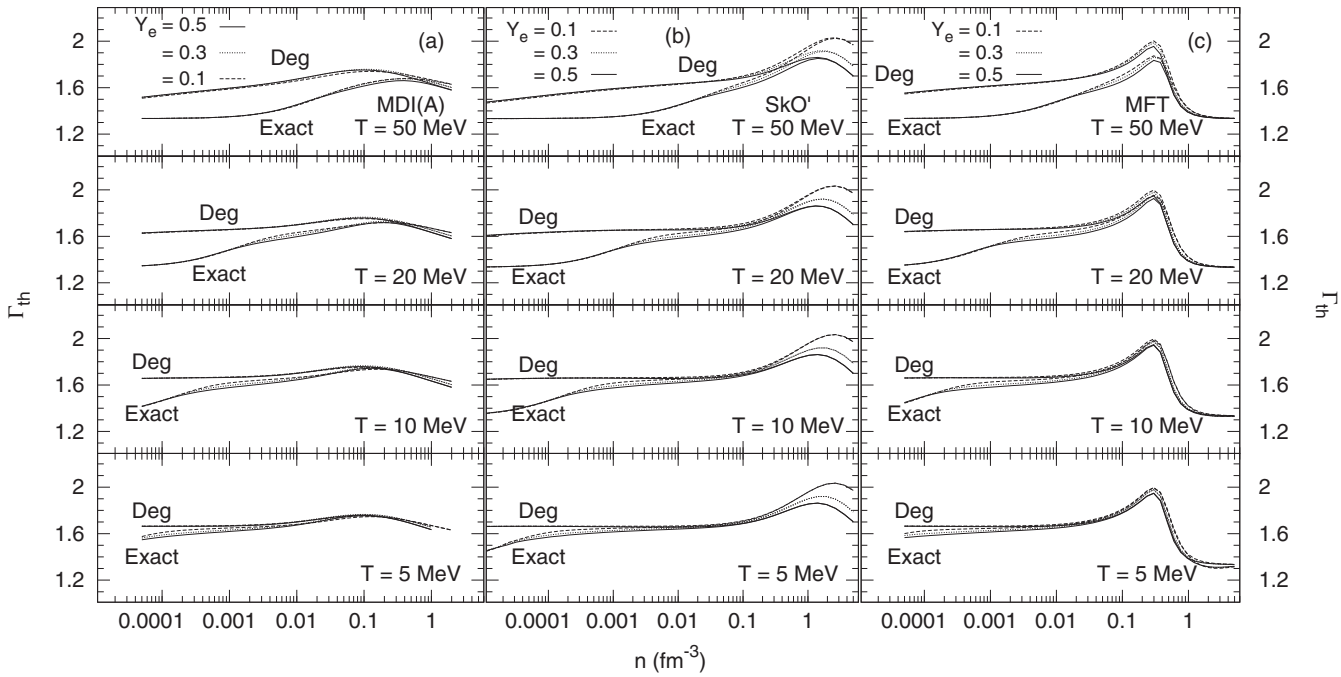

FIG. 29. Same as Fig. 25, but with the inclusion of leptons and photons.

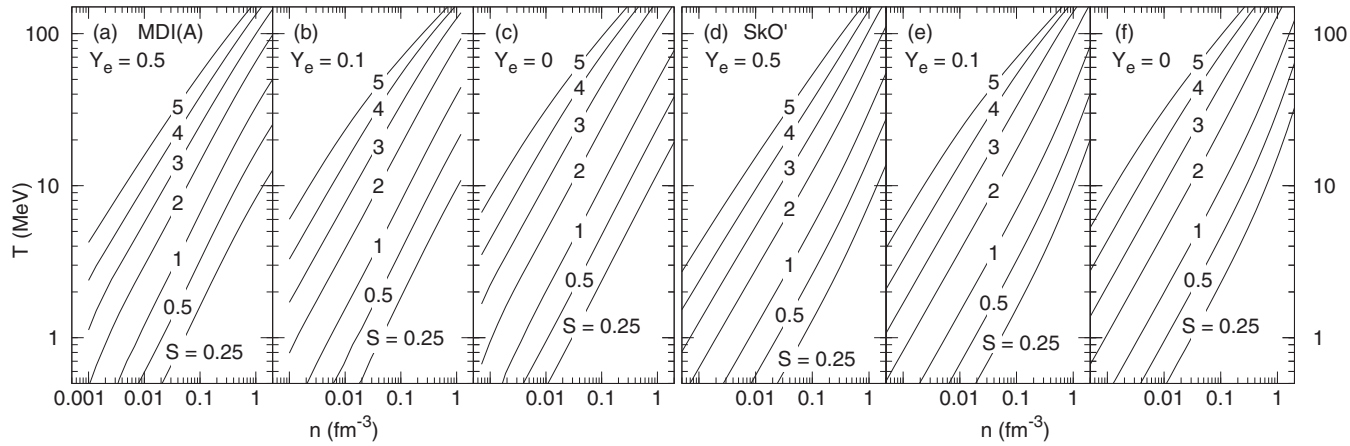

FIG. 30. Isentropes for the MDI(A) and SkO′ models for matter with nucleons, leptons, and photons.

where $C(n)$ is a density-dependent factor. The T^2 term cannot be ignored at this level of approximation because it is of the same order in T as the thermal pressure, $P_{\rm th}$. We circumvent this problem by turning to Eq. (19) and write the adiabatic index as

$$\Gamma_S = \frac{n}{P_0+P_{\rm th}}\left\{\left.\frac{\partial(P_0+P_{\rm th})}{\partial n}\right|_T + \frac{T}{n^2C_V}\left[\left.\frac{\partial(P_0+P_{\rm th})}{\partial T}\right|_n\right]^2\right\}$$
$$= \frac{n}{P_0+P_{\rm th}}\left[\frac{K}{9}+\left.\frac{\partial P_{\rm th}}{\partial n}\right|_T + \frac{T}{n^2C_V}\left(\left.\frac{\partial P_{\rm th}}{\partial T}\right|_n\right)^2\right], \quad (83)$$

where P_0 and K are the cold pressure and incompressibility, respectively, the baryonic components of which are listed in Appendix A.

Under degenerate conditions (when contributions from photons are not significant), $P_{\rm th}$ can also be expressed in terms of S (to leading order) as [28,71]

$$P_{\rm th} = \frac{nS^2}{6}\frac{\sum_i a_i Y_i Q_i}{\left(\sum_i a_i Y_i\right)^2}, \quad i = n,p,e, \quad (84)$$

which allows Γ_S to be calculated in a relatively simple manner and provides a check on results from Eq. (83).

When nondegenerate conditions prevail, analytical expressions for $P_{\rm th}$, S, C_V, $(\partial P/\partial T)|_n$, and $(\partial P/\partial n)|_T$ in Eqs. (160), (161), (168), (170), and (171) of Ref. [71] are useful and are employed here. In the semidegenerate region, numerical calculations are unavoidable.

Results at zero temperature

As Γ_S receives significant contributions from the zero-temperature pressure and its variation with density, we begin our analysis by examining $\Gamma_{S=0}$, which highlights the role of contributions from electrons. Figure 31 shows $\Gamma_{S=0}$ at select values of Y_e for the two models employed here. The dashed curves in this figure are for nucleons only, whereas the solid curves include the contributions from leptons. Noteworthy features of the results for nucleons are (i) they diverge at values of n for those $Y_p = Y_e$ for which the pressure vanishes, (ii) they are negative in some regions of subsaturation densities, indicating mechanical instability, and (iii) they approach constant values for asymptotically low and high densities. The inclusion of charge-balancing electrons renders $\Gamma_{S=0}$ to (i) be positive for all n, thereby restoring mechanical stability, (ii) exhibit a gradual variation from a low to high value with the largest variation occurring at subsaturation densities, and (iii) approach constant values for asymptotically low and high densities. These features can be quantitatively understood by examining the nucleon and lepton pressures as functions of density (see Fig. 32), as the folldue analysis shows.

At zero temperature (entropy), the pressure of relativistic leptons (electrons) can be written as

$$P_l = \frac{\hbar c}{4}n_0(3\pi^2 n_0)^{1/3}Y_e^{4/3}\left(\frac{n}{n_0}\right)^{4/3}. \quad (85)$$

Thus, the adiabatic index of matter with baryons and leptons takes the form

$$\Gamma_{S=0} = \left(\frac{4}{3}+\frac{n}{P_l}\frac{dP_b}{dn}\right)\left(1+\frac{P_b}{P_l}\right)^{-1}, \quad (86)$$

where use of $dP_l/dn = (4/3)P_l$ has been made. For n not too far from n_0, the pressure of baryons is well approximated by

$$P_b \simeq \frac{K_0 n_0}{9}u^2(u-1) + n_0(1-2x)^2u^2\frac{dS_2}{du}, \quad (87)$$

where $u = n/n_0$. These relations allow us to gain an analytical understanding of the magnitude of $\Gamma_{S=0}$ in terms of quantities accessible to nuclear experiments. For SNM, $P_b = 0$ at $u = 1$ so that $\Gamma_{S=0}$ takes the simple form

$$\Gamma_{S=0}(u=1) = \frac{4}{3}+\frac{(K_0/9)}{(P_l/n_0)}. \quad (88)$$

With $P_l = 5.26\ {\rm MeV\,fm^{-3}}$ and values of K_0 and n_0 from Table VI at $u = 1$, we obtain $\Gamma_{S=0} = 2.12(2.09)$ for the MDI(A)[SkO′] model, in very good agreement with the exact results in Fig. 31.

The density at which mechanical instability of cold baryons-only matter (often referred to as the spinodal instability) sets in is determined by $dP_b/dn = 0$. In this case,

$$\Gamma_{S=0}^{\rm (sp)} = \frac{4}{3}\left(1+\frac{P_b}{P_l}\right)^{-1}, \quad (89)$$

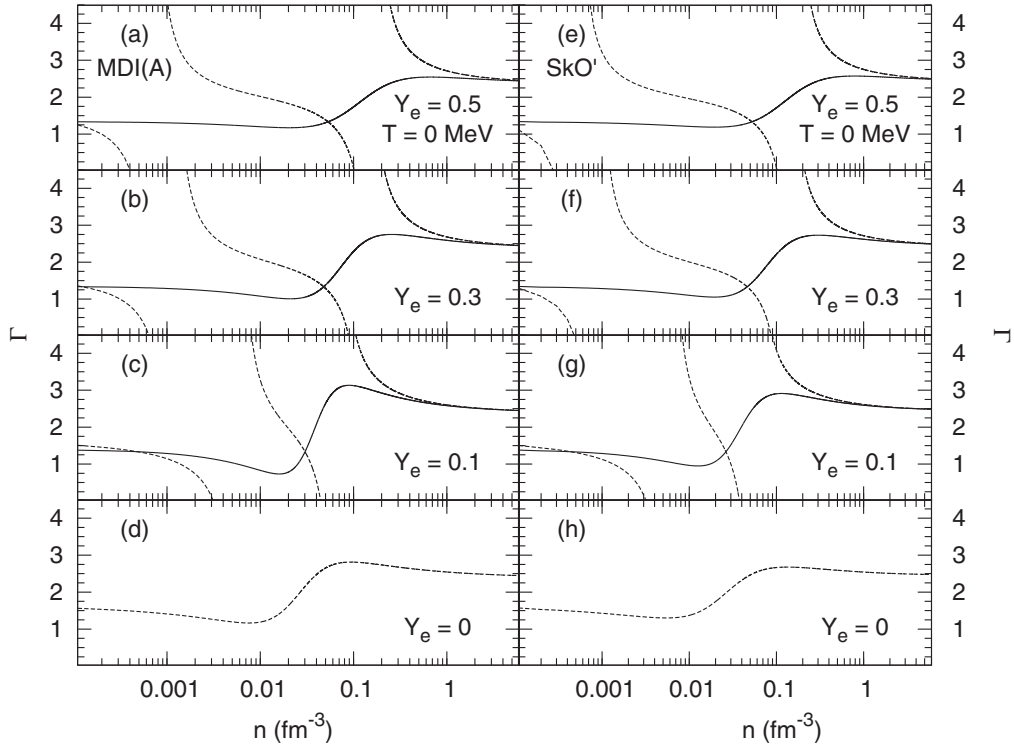

FIG. 31. The zero-temperature adiabatic index $\Gamma_{S=0}$ for the MDI(A) and SkO′ models at at the indicated proton fractions. Dashed curves include only nucleons, while solid lines include nucleons and leptons.

where the superscript (sp) stands for spinodal. Figure 32 shows the baryon and lepton pressures vs density from which the density regions in which mechanical or spinodal instability occurs for baryons-only matter for the two models can be ascertained. For SNM, Eq. (87) implies that $u_{(\mathrm{sp})} = 2/3$, in good agreement with the exact results for both models. From Eqs. (85) and (87), the leptonic and baryonic pressures at $u_{(\mathrm{sp})}$ are

$$P_l(u_{(\mathrm{sp})}) = 3.06\ \mathrm{MeV\,fm^{-3}},$$
$$P_b(u_{(\mathrm{sp})}) = -(4/243)K_0 n_0, \tag{90}$$

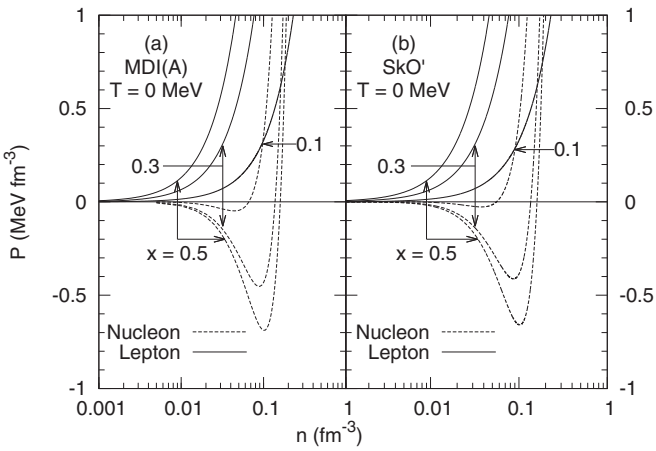

FIG. 32. Zero-temperature nucleon (dashed curves) and lepton (solid curves) pressures at the indicated proton fractions.

which yield $\Gamma^{(\mathrm{sp})}_{S=0} \simeq 1.67(1.65)$ for the MDI(A)[SkO′] model, in good accord with the exact results.

Equation (87) further implies that the density at which the derivative of the baryonic pressure, dP_b/du is maximum occurs at $u = 1/3$. At this density,

$$P_b(u = 1/3) = -(2/243)K_0 n_0,$$
$$P_l(u = 1/3) = 1.22\ \mathrm{MeV\,fm^{-3}}. \tag{91}$$

The corresponding expression for $\Gamma_{S=0}$ is

$$\Gamma_{S=0}(u = 1/3) = \left(\frac{4}{3} - \frac{1}{81}\frac{K_0 n_0}{P_l}\right)\left(1 - \frac{2}{243}\frac{K_0 n_0}{P_l}\right)^{-1}, \tag{92}$$

which yields a numerical value of $\simeq$1.28 for both the MDI(A) and SkO′ models. Note that $u = 1/3$ marks the density at which $\Gamma_{S=0}$ begins to rise for both models.

For matter with $Y_e = 0$ (PNM),

$$\frac{dP_b}{dn} = \frac{K(n)}{9} + 2uS_2' + u^2 S_2'', \tag{93}$$

using which we can write

$$\Gamma_{S=0} = \left[\frac{K_0}{9}(u-1) + S_2'\right]^{-1}\left[\frac{K_0}{9}(3u-2) + 2S_2' + uS_2''\right], \tag{94}$$

where the primes above denote derivatives with respect to u. The relation above highlights the roles of the first and second derivatives of the symmetry energy $S_2(n)$ at subsaturation

densities of SNM. For the special case of PNM at $u = 1$, the adiabatic index therefore becomes

$$\Gamma_{S=0}(u=1) = 2 + \frac{1}{3}\frac{K_0 + K_v}{L_v}. \quad (95)$$

Utilizing the values of K_0, K_v, and L_v in Table VI, we obtain $\Gamma_{S=0}(u=1) = 2.82(2.69)$ for the MDI(A)[SkO′] model, in excellent agreement with the exact results of 2.77 and 2.67, respectively.

For PNM at $u = 2/3$, $\Gamma_{S=0}$ simplifies to

$$\Gamma_{S=0}(u=2/3) = 2\left(1 - \frac{1}{27}\frac{K_0}{S_2'}\right)^{-1}\left(1 + \frac{1}{3}\frac{S_2''}{S_2'}\right), \quad (96)$$

where the derivatives above are evaluated at $u = 2/3$. The values of S_2' and S_2'' at $u = 2/3$ are $24.93(-12.15)$ and $26.48(-12.9)$ for the MDI(A) [SkO′], respectively. The corresponding values of $\Gamma_{S=0}(u=2/3)$ are 2.56 and 2.43 for the two models, which match closely with results of exact numerical calculations that yield 2.81 and 2.67, respectively. The differences from the exact results can be attributed to terms involving S_4 and its derivatives.

For values $0 < Y_e < 0.5$, an analysis similar to that presented above can be performed using Eq. (87). The density at which the spinodal instability sets in, determined by solving

$$(3u-2) + (1-2x)^2\left(\frac{18S_2'}{K_0} + \frac{9uS_2''}{K_0}\right) = 0, \quad (97)$$

steadily shifts to lower values of u as x decreases toward 0. Corrections due to the skewness in $E(n,x)$ and contributions from $S_4(n,x)$, etc., are small and do not affect the qualitative behaviors. As for $Y_e = 0.5$, the contribution from electrons to the total pressure entirely removes the mechanical (spinodal) instability present in baryons-only matter for all Y_e as also confirmed by the exact numerical results.

At asymptotically low densities and for $Y_e \neq 0$, $\Gamma_{S=0}$ approaches 4/3, the value characteristic for relativistic electrons. For PNM, the corresponding value is 5/3, as expected for nonrelativistic neutrons. For asymptotically high densities and for all Y_e, $\Gamma_{S=0}$ is controlled by a combination of the highest powers of density in the expression for the pressure of baryons; both models yield the value of $\simeq$2.5.

Results for finite entropies

In Fig. 33, $\Gamma_{S=0}$ and $\Gamma_{S=1}$ for matter with baryons, leptons, and photons are contrasted for several values of Y_e. A characteristic feature to note is that $\Gamma_{S=1} < \Gamma_{S=0}$ for densities beyond a certain Y_e-dependent density, whereas the opposite is the case below that density for each Y_e. The densities at which $\Gamma_{S=1} = \Gamma_{S=0}$ occurs at subsaturation densities and ranges from $\sim$0.02 to 0.1 fm^{-3} for Y_e in the range 0–0.5. The approach to the corresponding low- and high-density asymptotic values also depends on Y_e. The largest differences between the results of $S = 0$ and $S = 1$ are for PNM, the least differences being those for SNM.

As $S = 1$ represents matter that is degenerate for all but the very low densities, the ingredients that cause the behaviors in Fig. 33 can be identified by utilizing the results of FLT. Here we provide relations applicable to the cases of SNM and PNM. Those for intermediate Y_e′s are straightforward to develop, albeit lengthy. We start from

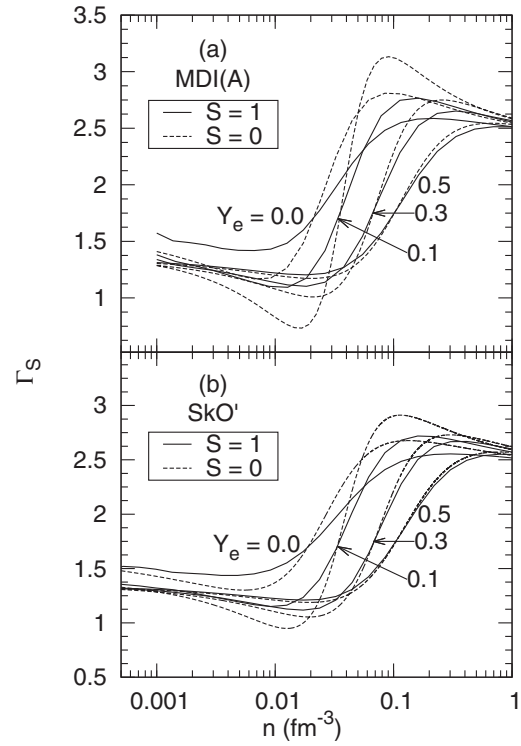

FIG. 33. Adiabatic index at fixed entropy for the SkO′ and MDI(A) models. Results are from Eqs. (86) and (98).

$$\Gamma_S = \left[\frac{n}{P_0 + P_{\rm th}}\frac{d}{dn}(P_0 + P_{\rm th})\Big|_S\right], \quad (98)$$

with $P_0 = P_{b0} + P_{l0}$. The leptonic pressure and its derivative at zero temperature (entropy), P_{l0} and dP_{l0}/dn, are obtained from Eq. (85). The cold baryonic pressure P_{b0} is that from an appropriate model for baryons [MDI(A) or SkO′ in this paper] and its derivative $dP_{b0}/dn = K(n)/9$. In the degenerate limit of SNM in which $p_{F_b} = p_{F_e} = (3\pi^2 n/2)^{1/3}$, the thermal pressure and its derivative are

$$P_{\rm th} = \frac{S^2}{6}n\left(a_b Q_b + \frac{a_e}{4}\right)\left(a_b + \frac{a_e}{2}\right)^{-2},$$
$$\frac{dP_{\rm th}}{dn} = \frac{P_{\rm th}}{n}\left[1 + \frac{4}{3}\left(a_b Q_b + \frac{a_e}{4}\right)\left(a_b + \frac{a_e}{2}\right)^{-1} + \left(a_b n\frac{dQ_b}{dn} - \frac{2}{3}a_b Q_b^2 - \frac{a_e}{12}\right)\left(a_b Q_b + \frac{a_e}{4}\right)^{-1}\right]. \quad (99)$$

The quantities $a_b = \pi^2 m_b^*/(2p_{F_b}^2)$ and $a_e \simeq \pi^2/(2p_{F_e})$ are the level density parameters of the baryons and relativistic electrons, respectively. The quantity Q_b is as in Eq. (62), and for the SkO′ model,

$$Q_b = 1 + \frac{3}{2}\left(1 - \frac{m_b^*}{m}\right); \quad n\frac{dQ_b}{dn} = \frac{3}{2}\frac{m_b^*}{m}\left(1 - \frac{m_b^*}{m}\right), \quad (100)$$

which exemplifies the role of the effective masses in determining $P_{\rm th}$. Also, use of $Q_e \simeq 1/2$ has been made in obtaining Eq. (99). Using this equation, one can calculate Γ_S for SNM.

Relations appropriate for PNM are obtained simply by setting $a_e = 0$ in Eq. (99) with the result

$$P_{\rm th} = \frac{S^2}{6}\left(\frac{nQ_b}{a_b}\right),$$
$$\frac{dP_{\rm th}}{dn} = \frac{P_{\rm th}}{n}\left(1 + \frac{2}{3}Q + \frac{n}{Q_b}\frac{dQ_b}{dn}\right). \quad (101)$$

Consequently, the adiabatic index for PNM becomes

$$\Gamma_s = \frac{n}{P_0 + P_{\rm th}}\left[\frac{K}{9} + \frac{S^2}{6a}5\left(\frac{4}{3} - \frac{m_b^*}{m}\right)\right] \quad (102)$$

for the SkO′ model, which exhibits the role of the effective mass in determining the thermal component for finite S. The result for the MDI(A) model is straightforward to obtain, but is somewhat more lengthy due to its lengthy expression for the baryon effective mass. We have verified that the degenerate limit result for Γ_s accurately reproduces the exact results for all values of Y_e shown in Fig. 33.

Based on a mean-field theoretical model, Shen *et al.* [3] presented results for $\Gamma_{S=1}$ for various Y_e′s including inhomogeneous phases at subsaturation densities and found that it rises abruptly at the transition from nonuniform to uniform matter. In the region of densities for which an appropriate comparison can be made (i.e., the homogeneous phase), our results agree semiquantitatively with those of Ref. [3], differences being attributable to the different model parameters used.

Figure 34 shows the effect of increasing S for $Y_e = 0.5$. Also shown are results from the degenerate and nondegenerate limit expressions discussed above. The remarkable feature of the results shown is that the finite and zero entropy adiabatic indices are equal at nearly the same density, $n_\times \simeq 0.08$–0.09 fm^{-3}, for a wide range of entropies. For a fixed Y_e, the intersection density $n_\times$ can be determined by setting $\Gamma_{S=0} = \Gamma_S$, which can be rearranged to

$$\frac{1}{P_0}\frac{dP_0}{dn} = \left(\frac{1}{P_{\rm th}}\frac{dP_{\rm th}}{dn}\right)\Bigg|_S. \quad (103)$$

Note that in the degenerate limit, the right-hand side becomes independent of S [see the relations in Eq. (99)], which explains the near independence with S of $n_\times$, which is mainly determined by the density-dependent terms on the left-hand side and a_b, a_e, and Q_b on the right-hand side. Insofar as the pressure can be expressed as of function of Y_i′s and to higher orders in S, a mild dependence of $n_\times$ on S may be expected. Not surprisingly, the nondegenerate approximation reproduces the exact results for Γ_S vs n better than the degenerate approximation with increasing values of S.

The logarithmic derivative $d\ln P_0/d\ln n$ exhibits its largest variation at subsaturation densities (see Fig. 32), whereas $(d\ln P_{\rm th}/d\ln n)|_S$ remains relatively flat (with values that decrease slightly from $\sim 5/3$ with increasing S) around the intersection density $n_\times$. In addition, $d\ln P_0/d\ln n > (d\ln P_{\rm th}/d\ln n)|_S$ for $n > n_\times$, but the reverse trend prevails for $n < n_\times$. These general features for all Y_e′s make $\Gamma_S < \Gamma_{S=0}$ for densities larger than $n_\times$ and $\Gamma_S \geqslant \Gamma_{S=0}$ for densities lower.

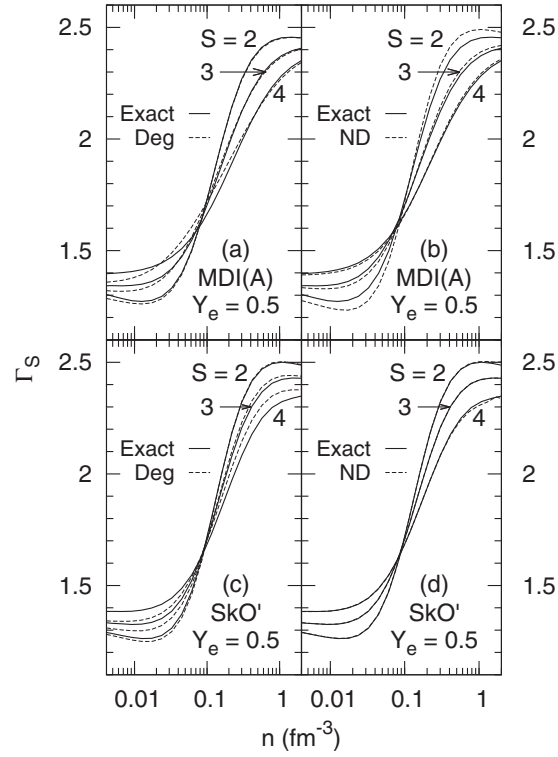

FIG. 34. Adiabatic index at fixed entropy from the SkO′ and MDI(A) models for SNM using Eq. (98). Results for the degenerate (left) and nondegenerate (right) limits are from Eqs. (98) and (99), respectively.

The degenerate and nondegenerate approximations to Γ_S are compared with the exact numerical results in Fig. 35 for $S = 2$, 3, and 4. For both models, and for both Y_e′s shown, the degenerate approximation reproduces the exact results only for $S = 2$ at supranuclear densities. As high temperatures are required at these densities for S exceeding 2, the nondegenerate approximation fares better, being indistinguishable from the exact results.

In Fig. 36, we show the contributions of nucleons, leptons, and photons for fixed entropies $S = 1$ and 4. For both proton fractions shown, the dominant contributions are from nucleons except at very high densities when contributions from leptons begin to become equally important. The density-independent contributions from photons are significant only for large values of S.

C. Speed of sound

A quantity closely related to Γ_S is the adiabatic speed of sound c_s given by

$$\left(\frac{c_s}{c}\right)^2 = \frac{dP}{d\epsilon}\Bigg|_{S,Y_e}, \quad (104)$$

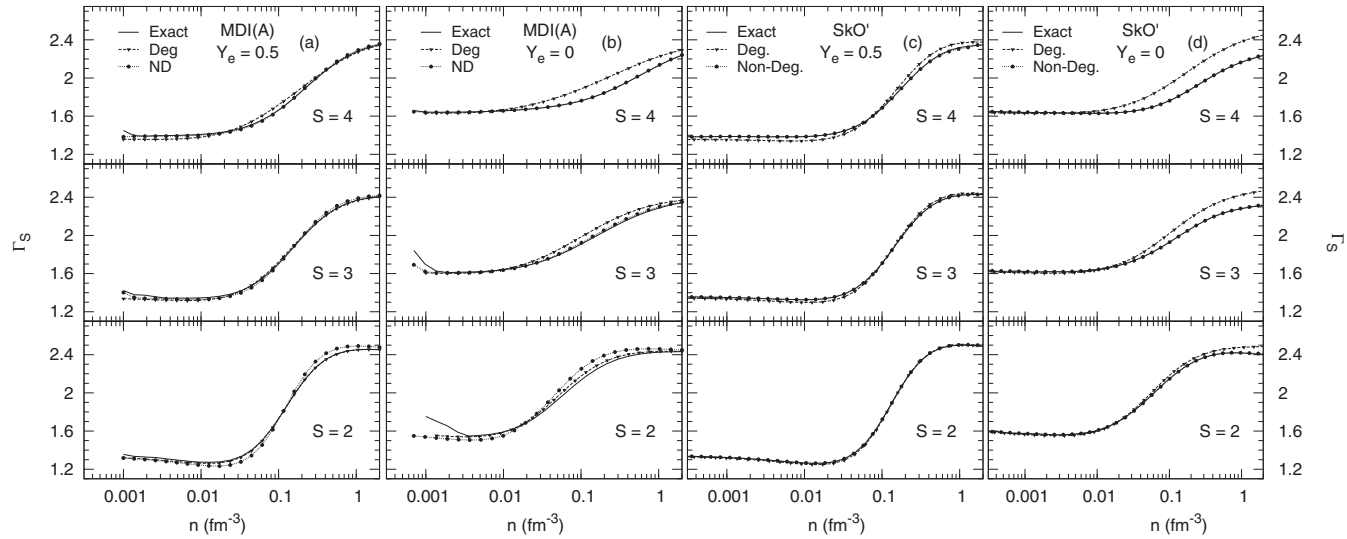

FIG. 35. Adiabatic index at constant entropy for the SkO′ and MDI(A) models using Eqs. (98) and (99). Results for SNM (a),(c) and for PNM (b),(d) are shown along with their limiting cases.

where c is the speed of light. The energy density ϵ above is inclusive of the rest-mass density; in relativistic approaches this is so by default, but in nonrelativistic ones one must write $\epsilon = \varepsilon + mn$, where the first term here is the internal energy density.

Equation (104) can be expressed in terms of derivatives of the density:

$$\left(\frac{c_s}{c}\right)^2 = \left.\frac{dP}{dn}\right|_{S,Y_e} \left(\left.\frac{d\epsilon}{dn}\right|_{S,Y_e}\right)^{-1} \tag{105}$$

$$= \frac{\left.\frac{dP}{dn}\right|_{S,Y_e}}{E + m + n\left.\frac{dE}{dn}\right|_{S,Y_e}}. \tag{106}$$

Then by taking advantage of the total differential of the energy per particle,

$$dE = TdS + \frac{P}{n^2}dn + (\mu_p + \mu_e - \mu_n)dY_e, \tag{107}$$

we transform Eq. (106) to

$$\left(\frac{c_s}{c}\right)^2 = \left.\frac{dP}{dn}\right|_{S,Y_e} \frac{1}{E + m + \frac{P}{n}} = \Gamma_S \frac{P}{h + mn}, \tag{108}$$

thereby making the connection between c_s and Γ_S explicit. Here, $h = \varepsilon + P$ is the enthalpy density. Equation (108) generalizes the definition of the squared speed of sound to finite entropy. This result can also be derived from a time-dependent analysis of traveling sound waves in a medium (see, e.g., [99,100]). Note that Eq. (108) defines c_s in terms of previously calculated quantities and, furthermore, allows one to write c_s in the degenerate limit as an explicit function of the entropy.

Results for $(c_s/c)^2$ vs n for the two models are shown in Fig. 37 for values of S up to 4. Contributions from photons are straightforwardly included in Γ_S, P, and h of Eq. (108). Finite entropy contributions to c_s^2 depend on the density and are positive up to some high density beyond which the trend is reversed.

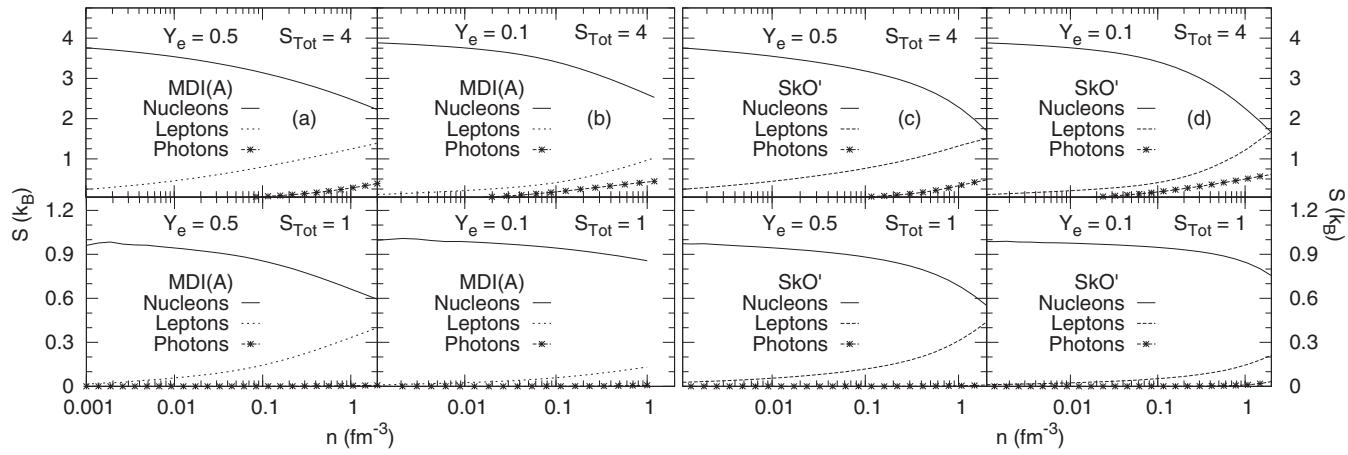

FIG. 36. Contributions from nucleons, leptons, and photons to the total entropy at the indicated proton fractions for the MDI(A) and SkO′ models.

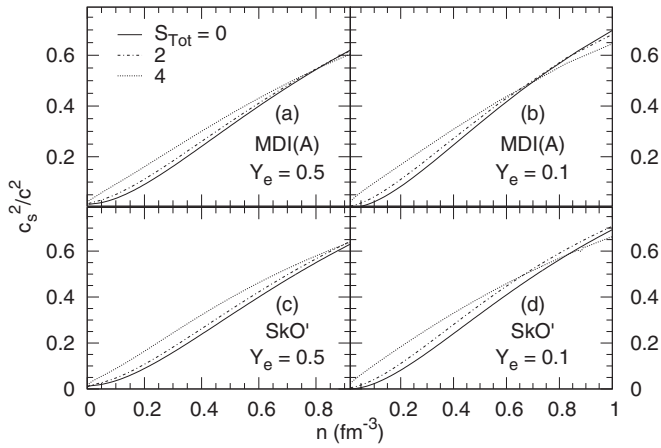

FIG. 37. Squared sound speed vs density for various entropy per baryon from Eq. (108).

VII. SUMMARY AND CONCLUSION

In this work, we have sought answers to the folldue questions. (1) Are EOSs based on finite range interactions that describe the observed collective flow in 0.5–2 GeV/A heavy-ion collisions (HICs) able to account for the largest of the recently well-measured neutron star masses $\simeq 2M_\odot$? (2) How do the thermal properties of such EOSs compare with those of zero range Skyrme models? (3) What are the predictions for $\Gamma_{\rm th}$ and Γ_S in finite and zero range models, and how do they differ from those currently used in simulations of PNS and mergers of compact binary stars?

To account for the collective flow observables in HICs, density and momentum-dependent mean fields that match optical-model potential fits to nucleon-nucleus scattering data are required [14,16–20]. Such mean fields are also the result of microscopic many-body calculations of dense nucleonic matter [81,82]. A characteristic feature of these mean fields is that for large momenta they saturate, unlike those of zero range Skyrme models, which rise quadratically with momentum (thereby yielding flow observables that are too large compared with data). To describe HICs, features of microscopic calculations have been successfully parametrized in schematic models using, e.g., finite range Yukawa-type forces [14,18,25]. In this work, we have adapted the MDI(0) model of Das *et al.* [25], in which the mean field is both isospin- and momentum-dependent to study both the structural aspects of neutron stars and the thermal properties of isospin-asymmetric matter. Our principal findings and conclusions are summarized below.

The MDI(0) model yields a neutron star maximum mass of $1.88M_\odot$, which falls slightly below the central value of the largest well-measured mass of $2.01 \pm 0.04M_\odot$. The radius of the $1.4M_\odot$ star is 11.27 km, to be compared with 11.5 ± 0.7 km recommended in Refs. [32–34]. To bring the maximum mass closer to the observed value, we devised a revised parametrization labeled MDI(A) that gave $\mathrm{M_{max}} = 1.97M_\odot$ and a radius of 11.58 km for the $1.4M_\odot$ star. At the edges of the 1σ errors of the empirical properties K_0, L_v, and K_v at the nuclear equilibrium density [with attendant small changes in the strength and range parameters of MDI(A)], results obtained were $M_{\rm max} = 2.15M_\odot$ and a radius of 12.13 km for the $1.4M_\odot$ star. The conclusion from these results is that a momentum-dependent EOS that reproduces heavy-ion flow data is well able to yield neutron stars in excess of $2M_\odot$.

Our study of thermal effects were performed for the MDI(A) model and the zero range Skyrme model called SkO′ to provide contrasts. The two models give nearly identical results for the EOS at $T = 0$ for both nuclear matter and PNM at all densities. Consequently, bulk properties accessible in experiments involving nuclei are similar for the two models as are their neutron star attributes. However, the momentum dependencies of their mean-field potentials are distinctly different, particularly at large momenta. The MDI(A) potential saturates logarithmically at high momenta, whereas that of SkO′ rises quadratically with momentum as in all Skyrme models. These differences are reflected in their effective masses, both in their magnitudes and density dependencies. The influence of their differing effective masses on the thermal components of energies, pressures, chemical potentials, and the specific heats at constant volume (C_V) and pressure (C_P) were explored in detail for both SNM and PNM. Analytical formulas for the thermal components for all proton fractions from 0 to 0.5 in the degenerate and nondegenerate limits were derived and presented. These formulas shed considerable light on the origin of the differences between the results of the two models.

The isospin splitting of the effective masses in the MDI(A) and SkO′ models is similar in that $m_n^* > m_p^*$ in neutron-rich matter for all densities. Such is not the case in many Skyrme models (in which $m_n^* < m_p^*$ for neutron-rich matter), which have been successful in predicting the ground-state properties and collective excitations of nuclei. This curious feature led us to establish relations involving the strength and range parameters of these models in which $m_n^* > m_p^*$, as found in microscopic calculations of dense matter [85–87].

The conclusion that emerges from comparing the exact numerical results of the MDI(A) and SkO′ models is that the agreement or disagreement depends on the specific thermal variable in question, as well as the values of (n,x,T). Thermal properties that depend on the density derivatives of m^*s exhibit the greatest degree of disagreement between the two models. For example, at $T = 20$ MeV the thermal energies of SNM begin to differ for $n > n_0$, whereas they do so for $n < 2n_0$ at $T = 50$ MeV. For PNM, there is good agreement for all densities at $T = 20$ MeV, but not so for $n > n_0$ at $T = 50$ MeV. The thermal pressures, which receive contributions from density derivatives of m^*s, begin to deviate from each other for $n > n_0$ for both $x = 0$ and $x = 0.5$ at $T = 20$ MeV, whereas they do so for $n > 2n_0$ at $T = 50$ MeV. Notably, the thermal pressure of MDI(A) saturates at high density, whereas that of SkO′ increases parabolically. Similar dependencies on (n,x,T), albeit in different regimes of (n,x), are seen for the thermal chemical potentials, but to a lesser degree for the entropy per baryon.

The influence of finite range interactions is particularly evident when one compares C_V and C_P with those of the SkO′ model. Significant differences are manifest in C_V for wide ranges of n. A momentum structure other than p^2 in the single-particle potential introduces an implicit temperature dependence in the spectrum, which causes the C_V of MDI(A) to exceed the classical value of $3/2k_B$ at intermediate

densities. Likewise, departures in C_P also depend on the values of (n,x,T).

Given the vast number of Skyrme parametrizations in the literature, many of which are able to successfully predict ground-state and excitation properties of nuclei, it is quite possible that their thermal properties (exceptions being response functions such as specific heats, susceptibilities, etc.) can be made to resemble those of models with finite range interactions. However, their inability to describe heavy-ion data satisfactorily would remain due to the quadratically rising momentum dependence of their mean-field potentials.

Astrophysical simulations of PNSs and binary mergers of compact stars are also sensitive to thermal effects in widely varying regions of n, Y_e, and T. We therefore conducted an in-depth analysis of $\Gamma_{\rm th}$, Γ_S, and the speed of sound c_s (a guide for the rapidity with which hydrodynamic evolution proceeds) of hot and dense matter containing nucleons, leptons, and photons.

We find that a constant value for $\Gamma_{\rm th}$ (characteristic of ideal gases) often used in simulations is not supported by results of either potential or MFT models. Our results indicate a weak dependence of $\Gamma_{\rm th}$ on T and Y_e in all models, but a significant dependence on baryon density. The greatest discrepancy from a constant value extends from subsaturation densities to a few times the equilibrium density of symmetric matter. The saturation of the MDI(A) mean field at high momenta leads to a noticeably weaker density dependence of $\Gamma_{\rm th}$ relative to those of SkO′ and MFT models. We expect that similar features will be present in any model in which the nuclear mean field saturates appropriately regardless of its specific functional form.

There is little to separate MDI(A) and SkO′ in their respective Γ_S and by extension c_s. This is not very surprising because Γ_S is stripped of the leading contributions from both S and m^*. What remains is a weak dependence on isospin content, but it can be attributed to the choice of parametrization and not to the different natures of the single-particle potentials of the two models. For example, Γ_S for MDI(A) varies more strongly with changing proton fraction x compared to SkO′, and as such it mimics the behavior of the m^*s in MDI(A) relative to that of SkO′. Nevertheless, a parametrization with less splitting for curves of $m^{*\prime}$s corresponding to different x can easily be devised while still retaining a saturating mean field.

Our focus here was on the homogeneous phase of matter results of which provide a benchmark against which effects of inhomogeneous phases known to exist at subsaturation densities and low entropies can be assessed. Whether models with finite range interactions would yield thermal properties of such phases that differ significantly from those of zero range models is unexplored and is a subject for future study.

Our present study has highlighted the influence of nucleon effective masses, particularly their isospin and density dependencies, on the thermal properties of baryons. Equally important is the role of leptons which serve to remove the mechanical (or spinodal) instability of baryons-only matter at subsaturation densities. We find that substantial variations in $\Gamma_{\rm th}$ and Γ_S begin to occur at subsaturation densities before asymptotic values at supra-nuclear densities are reached. Consequently, laboratory experiments and theoretical studies involving neutron-rich matter can pin down these quantities.

ACKNOWLEDGMENT

This work was supported by the US DOE Grants No. DE-FG02-93ER-40756 and No. DE-FG02-87ER-40317.

APPENDIX A: MDI-MODEL PROPERTIES AT $T = 0$

Here we use the decomposition of the MDI Hamiltonian density as $\mathcal{H} = \mathcal{H}_k + \mathcal{H}_d + \mathcal{H}_m$ to isolate contributions from kinetic sources and density- and momentum-dependent interactions to the quantities of interest.

1. Pressure P

$$P = n\frac{\partial \mathcal{H}}{\partial n} - \mathcal{H}, \tag{A1}$$

$$\frac{\partial \mathcal{H}}{\partial n} = \frac{\partial \mathcal{H}_k}{\partial n} + \frac{\partial \mathcal{H}_d}{\partial n} + \frac{\partial \mathcal{H}_m}{\partial n}, \tag{A2}$$

$$\frac{\partial \mathcal{H}_k}{\partial n} = \frac{5}{3n}\mathcal{H}_k, \tag{A3}$$

$$\frac{\partial \mathcal{H}_d}{\partial n} = A_1\frac{n}{n_0} + A_2\frac{n}{n_0}(1-2x)^2 + B\left(\frac{n}{n_0}\right)^{\sigma}[1 - y(1-2x)^2], \tag{A4}$$

$$\frac{\partial \mathcal{H}_m}{\partial n} = \frac{C_l}{n_0}\left(\frac{p_{Fn}}{3n}\frac{\partial I_{nn}}{\partial p_{Fn}} + \frac{p_{Fp}}{3n}\frac{\partial I_{pp}}{\partial p_{Fp}}\right) + \frac{2C_u}{n_0}\left(\frac{p_{Fn}}{3n}\frac{\partial I_{np}}{\partial p_{Fn}} + \frac{p_{Fp}}{3n}\frac{\partial I_{np}}{\partial p_{Fp}}\right), \tag{A5}$$

$$\frac{\partial I_{np}}{\partial p_{Fi}} = \frac{8\pi^2\Lambda^2}{(2\pi\hbar)^6}\left\{4p_{Fi}^2 p_{Fj} + 4\Lambda p_{Fi}^2 \times\left[\arctan\left(\frac{p_{Fi}-p_{Fj}}{\Lambda}\right) - \arctan\left(\frac{p_{Fi}+p_{Fj}}{\Lambda}\right)\right] + p_{Fi}\left(\Lambda^2 + p_{Fj}^2 - p_{Fi}^2\right)\ln\left[\frac{(p_{Fi}+p_{Fj})^2+\Lambda^2}{(p_{Fi}-p_{Fj})^2+\Lambda^2}\right]\right\}. \quad \text{Here} \quad i \neq j. \tag{A6}$$

2. Chemical potentials μ_i

$$\mu_i = \frac{\partial \mathcal{H}}{\partial n_i} = \frac{\partial \mathcal{H}_k}{\partial n_i} + \frac{\partial \mathcal{H}_d}{\partial n_i} + \frac{\partial \mathcal{H}_m}{\partial n_i}, \tag{A7}$$

$$\frac{\partial \mathcal{H}_k}{\partial n_i} = \frac{1}{2m}p_{Fi}^2, \tag{A8}$$

$$\frac{\partial \mathcal{H}_d}{\partial n_i} = A_1\frac{n}{n_0} \pm A_2\frac{n}{n_0}(1-2x) + B\left(\frac{n}{n_0}\right)^{\sigma} \times\left\{1 - \frac{y(\sigma-1)}{\sigma+1}(1-2x)^2\left[1 \pm \frac{2}{(\sigma-1)(1-2x)}\right]\right\} \quad + \text{for neutrons, } - \text{for protons,} \tag{A9}$$

$$\frac{\partial \mathcal{H}_m}{\partial n_i} = \frac{C_l}{n_0}\frac{p_{Fi}}{3n_i}\frac{\partial I_{ii}}{\partial p_{Fi}} + \frac{2C_u}{n_0}\frac{p_{Fi}}{3n_i}\frac{\partial I_{np}}{\partial p_{Fi}}. \tag{A10}$$

3. Single-particle potentials U_i

$$U_i(n_i,n_j,p_i) = A_1\frac{n}{n_0} \pm A_2\frac{n}{n_0}(1-2x) + B\left(\frac{n}{n_0}\right)^{\sigma}\left\{1-\frac{y(\sigma-1)}{\sigma+1}(1-2x)^2\left[1\pm\frac{2}{(\sigma-1)(1-2x)}\right]\right\}$$
$$+\frac{2C_l}{n_0}R_{ii}(n_i,p_i)+\frac{2C_u}{n_0}R_{ij}(n_j,p_i);\quad i\neq j\quad +\text{for neutrons, } -\text{for protons,} \tag{A11}$$

$$R_{ii}(n_i,p_i) = \frac{\Lambda^3}{4\pi^2\hbar^3}\left\{\frac{2p_{Fi}}{\Lambda}-2\left[\arctan\left(\frac{p_i+p_{Fi}}{\Lambda}\right)-\arctan\left(\frac{p_i-p_{Fi}}{\Lambda}\right)\right]+\frac{\left(\Lambda^2+p_{Fi}^2-p_i^2\right)}{2\Lambda p_i}\ln\left[\frac{(p_i+p_{Fi})^2+\Lambda^2}{(p_i-p_{Fi})^2+\Lambda^2}\right]\right\}, \tag{A12}$$

$$R_{ij}(n_j,p_i) = \frac{\Lambda^3}{4\pi^2\hbar^3}\left\{\frac{2p_{Fj}}{\Lambda}-2\left[\arctan\left(\frac{p_i+p_{Fj}}{\Lambda}\right)-\arctan\left(\frac{p_i-p_{Fj}}{\Lambda}\right)\right]+\frac{\left(\Lambda^2+p_{Fj}^2-p_i^2\right)}{2\Lambda p_i}\ln\left[\frac{(p_i+p_{Fj})^2+\Lambda^2}{(p_i-p_{Fj})^2+\Lambda^2}\right]\right\},$$
$$\text{for } i\neq j. \tag{A13}$$

4. Derivatives of the effective masses dm_i^*/dn_i

$$\frac{\partial m_i^*}{\partial n_i} = \frac{p_{Fi}}{3n_i}\left(-m_i^{*2}\right)\left(\frac{2C_l}{n_0}G_{ii}+\frac{2C_u}{n_0}G_{1,ij}\right);\quad i\neq j, \tag{A14}$$

$$\frac{\partial m_i^*}{\partial n_j} = \frac{p_{Fj}}{3n_j}\left(-m_i^{*2}\right)\frac{2C_u}{n_0}G_{2,ij};\quad i\neq j, \tag{A15}$$

$$\frac{\partial m_i^*}{\partial n} = (1-x)\frac{\partial m_i^*}{\partial n_n}+x\frac{\partial m_i^*}{\partial n_p}, \tag{A16}$$

$$G_{ii} = \frac{\Lambda^2}{2\pi^2\hbar^3}\left[\frac{-3}{p_{Fi}^2}+\frac{4}{4p_{Fi}^2+\Lambda^2}+\frac{2p_{Fi}^2+3\Lambda^2}{4p_{Fi}^4}\ln\left(1+\frac{4p_{Fi}^2}{\Lambda^2}\right)\right], \tag{A17}$$

$$G_{1,ij} = \frac{\Lambda^2}{2\pi^2\hbar^3}\left\{\frac{-p_{Fj}[p_{Fi}^4+4p_{Fi}^2\left(\Lambda^2-p_{Fj}^2\right)+3\left(\Lambda^2+p_{Fj}^2\right)^2]}{p_{Fi}^3[(p_{Fi}+p_{Fj})^2+\Lambda^2][(p_{Fi}-p_{Fj})^2+\Lambda^2]}+\frac{3\left(\Lambda^2+p_{Fj}^2\right)+p_{Fi}^2}{4p_{Fi}^4}\ln\left[\frac{(p_{Fi}+p_{Fj})^2+\Lambda^2}{(p_{Fi}-p_{Fj})^2+\Lambda^2}\right]\right\}, \tag{A18}$$

$$G_{2,ij} = \frac{\Lambda^2}{2\pi^2\hbar^3}\left\{\frac{2p_{Fj}^2\left(-p_{Fi}^2+\Lambda^2+p_{Fj}^2\right)}{p_{Fi}^2[(p_{Fi}+p_{Fj})^2+\Lambda^2][(p_{Fi}-p_{Fj})^2+\Lambda^2]}-\frac{p_{Fj}}{2p_{Fi}^3}\ln\left[\frac{(p_{Fi}+p_{Fj})^2+\Lambda^2}{(p_{Fi}-p_{Fj})^2+\Lambda^2}\right]\right\}. \tag{A19}$$

In the last two expressions, $i\neq j$.

APPENDIX B: MDI MODELS IN THE NONDEGENERATE LIMIT

The method to tackle the small degeneracy ($z\ll 1$) case is based primarily on two elements, the first of which is the assumption that in the nondegenerate (ND) limit the system is sufficiently dilute such that $R(p)$ in $\epsilon(p)$ depends weakly on momentum p and therefore the location p_0 of the peak of a given thermodynamic integrand is the same as that of a free gas,

$$\left.\frac{d}{dp}\left(\frac{p^\alpha}{1+z^{-1}e^{\frac{p^2}{2mT}}}\right)\right|_{p=p_0}=0 \tag{B1}$$

$$\Rightarrow p_0 \xrightarrow{z\ll 1} (\alpha mT)^{1/2}\left[1+\frac{1}{2e^{\alpha/2}}z-\frac{(1+2\alpha)}{8e^{\alpha}}z^2+\cdots\right]. \tag{B2}$$

The second element of the method is the happenstance that the Taylor series expansion about $z=0$ of the state functions results in integrals of the form

$$I=\int dpg(p)e^{-\beta f(p)}, \tag{B3}$$

which are amenable to estimation via the saddle-point approximation [101],

$$I \simeq \frac{\sqrt{2\pi}g_0e^{-\beta f_0}}{\sqrt{\beta f_0''}}\left[1+\beta^{-1}\left(\frac{5}{24}\frac{f_0'''^2}{f_0''^3}-\frac{1}{8}\frac{f_0^{iv2}}{f_0''^2}+\frac{g_0''}{2g_0f_0''}-\frac{g_0'f_0'''}{2g_0f_0''^2}\right)+O(\beta^{-2})\right], \tag{B4}$$

where the primes denote differentiation with respect to p and the subscripts 0 evaluation at $p=p_0$. The dummy variable β—set equal to 1 at the end of the calculation—keeps track of the order of the asymptotic expansion.

From Eq. (B4) it is clear that

$$\int dp e^{-\beta f(p)} \simeq \frac{\sqrt{2\pi} e^{-\beta f_0}}{\sqrt{\beta f_0''}}\left[1+\beta^{-1}\left(\frac{5}{24}\frac{f_0'''^2}{f_0''^3}-\frac{1}{8}\frac{f_0^{iv2}}{f_0''^2}\right)+O(\beta^{-2})\right]. \tag{B5}$$

Thus, to $O(\beta^{-1})$ in asymptotics, we can write

$$I \simeq g_0\left[1+\beta^{-1}\left(\frac{g_0''}{2g_0 f_0''}-\frac{g_0' f_0'''}{2g_0 f_0''^2}\right)\right]\int dp e^{-\beta f(p)}, \tag{B6}$$

which is convenient for our purposes because, as shown subsequently, the integral in Eq. (B6) can be evaluated exactly. Henceforth, we make use of

$$G_0 \equiv g_0\left(1+\frac{g_0''}{2g_0 f_0''}-\frac{g_0' f_0'''}{2g_0 f_0''^2}\right). \tag{B7}$$

We must note a caveat with regards to the use of the saddle-point approximation in the ND limit: High temperatures spread the integrands over a wider range and thus incur more error in the approximation. This is not a problem for the temperatures relevant to supernovae and compact objects ($T \leqslant 50$ MeV) but, nevertheless, the method cannot be expected to work for arbitrarily high temperatures. Such broadening can often be eliminated by a suitable variable change. However, no systematic way exists for finding the appropriate transformation.

In what follows, we demonstrate the method for a single-component gas for the sake of simplicity. Generalization to multicomponent gases is straightforward. We begin with $R(p)$ given by

$$R(p) = \frac{2C}{n_0}\frac{2}{(2\pi\hbar)^3}\int d^3p' \frac{1}{1+\left(\frac{\vec{p}-\vec{p}'}{\Lambda}\right)^2} f_p', \tag{B8}$$

where $C = C_l$ for PNM and $C = C_l + C_u$ for SNM. Performing the angular integrals leads to

$$R(p) = \frac{C}{2n_0}\frac{\Lambda^2}{\pi^2\hbar^3}\frac{1}{p}\int dp' p'^2 \ln\left[\frac{\Lambda^2+(p+p')^2}{\Lambda^2+(p-p')^2}\right]^{1/p'} f_p'. \tag{B9}$$

The assumption of weak dependence on p' allows us to treat $\ln[\cdots]^{1/p'}$ as constant evaluated at $p_{0R} = (2mT)^{1/2}$ [where only the leading term of Eq. (B2) is kept] and take it out of the integral:

$$R(p) = \frac{C}{2n_0}\frac{\Lambda^2}{p}\ln\left[\frac{\Lambda^2+(p+p_{0R})^2}{\Lambda^2+(p-p_{0R})^2}\right]^{\frac{1}{p_{0R}}}\frac{1}{\pi^2\hbar^3}\int dp' p'^2 f_p'. \tag{B10}$$

Thus, here we effectively keep only the first term in the saddle-point approximation. This, as well as the truncated p_{0R}, induce little error because in the ND limit $R(p)$ is itself a small correction to the spectrum.

Noting that

$$n = \frac{g}{2\pi^2\hbar^3}\int dp p^2 f_p, \tag{B11}$$

where g is the degeneracy factor, we write $R(p)$ as

$$R(p) = \frac{C}{n_0}\frac{\Lambda^2}{pp_{0R}}\ln\left[\frac{\Lambda^2+(p+p_{0R})^2}{\Lambda^2+(p-p_{0R})^2}\right]\frac{n}{g}. \tag{B12}$$

In the next step, we expand Eq. (B11) in a Taylor series about $z = 0$:

$$n \simeq \frac{g}{2\pi^2\hbar^3}\left[z\int dp p^2 e^{-\frac{p^2}{2mT}-\frac{R(p)}{T}} - z^2\int dp p^2 e^{-\frac{p^2}{mT}-\frac{2R(p)}{T}}+\cdots\right] \tag{B13}$$

$$= \frac{g}{2\pi^2\hbar^3}\left[z\int dp e^{-\frac{R(p)}{T}} e^{-\frac{p^2}{2mT}+2\ln p} - z^2\int dp e^{-\frac{2R(p)}{T}} e^{-\frac{p^2}{mT}+2\ln p}+\cdots\right], \tag{B14}$$

where terms in the single-particle energy spectrum that depend only on the density have been absorbed in z. For the first integral we identify

$$g_{n1}(p) = e^{-R/T}, \quad f_{n1}(p) = \frac{p^2}{2mT} - 2\ln p, \quad p_{n1} = (2mT)^{1/2}, \tag{B15}$$

and for the second

$$g_{n2}(p) = e^{-2R/T}, \quad f_{n2}(p) = \frac{p^2}{mT} - 2\ln p, \quad p_{n2} = (mT)^{1/2}. \tag{B16}$$

Therefore,

$$n \simeq \frac{g}{2\pi^2\hbar^3}\left(zG_{n1}\int dp e^{-\frac{p^2}{2mT}+2\ln p} - z^2 G_{n2}\int dp e^{-\frac{p^2}{mT}+2\ln p}\right) \tag{B17}$$

$$= zgG_{n1}n_Q - \frac{z^2}{2^{3/2}}gG_{n2}n_Q, \tag{B18}$$

where G_{n1}, G_{n2} are given by Eq. (B7) and $n_Q = (mT/2\pi\hbar^2)^{3/2}$ is the quantum concentration.

By perturbative inversion of Eq. (B18) to second order in n/n_Q we obtain

$$z = \frac{n}{G_{n1}gn_Q} + \frac{1}{2^{3/2}}\left(\frac{n}{G_{n1}gn_Q}\right)^2\frac{G_{n2}}{G_{n1}}. \tag{B19}$$

The chemical potential μ is related to z according to

$$\mu = T\ln z + u(n), \tag{B20}$$

where $u(n)$ are the terms in the single-particle potential which depend only on the density.

We now turn our attention to the kinetic energy density:

$$\tau = \frac{g}{2\pi^2\hbar^3}\int dp p^4 f_p \tag{B21}$$

$$\xrightarrow{z\ll 1} \frac{g}{2\pi^2\hbar^3}\left[z\int dp e^{-\frac{R(p)}{T}} e^{-\frac{p^2}{2mT}+4\ln p} - z^2\int dp e^{-\frac{2R(p)}{T}} e^{-\frac{p^2}{mT}+4\ln p}+\cdots\right]. \tag{B22}$$

With the identification

$$g_{\tau 1}(p) = e^{-R/T}, \quad f_{\tau 1}(p) = \frac{p^2}{2mT} - 4\ln p,$$
$$p_{\tau 1} = (4mT)^{1/2}, \tag{B23}$$
$$g_{\tau 2}(p) = e^{-2R/T}, \quad f_{\tau 2}(p) = \frac{p^2}{mT} - 4\ln p,$$
$$p_{\tau 2} = (2mT)^{1/2}, \tag{B24}$$

we obtain

$$\tau = 3mTG_{\tau 1} g n_Q \left(z - \frac{z^2}{2^{5/2}} \frac{G_{\tau 2}}{G_{\tau 1}}\right) \tag{B25}$$
$$= 3mTn \frac{G_{\tau 1}}{G_{n1}} \left[1 + \frac{1}{2^{3/2}} \left(\frac{n}{G_{n1} g n_Q}\right) \left(\frac{G_{n2}}{G_{n1}} - \frac{G_{\tau 2}}{2G_{\tau 1}}\right)\right]. \tag{B26}$$

The starting point for the calculation of the potential energy density is

$$V = \frac{C}{n_0} \frac{2g}{(2\pi\hbar)^6} \int d^3p d^3p' \frac{f_p f'_p}{1 + \left(\frac{\vec{p}-\vec{p}'}{\Lambda}\right)^2}, \tag{B27}$$

where the factor $2g$ would have been g^2 if C_l was equal to C_u. Invoking the definition of $R(p)$ [Eq. (B8)], we recast Eq. (B27) as

$$V = \frac{g}{4\pi^2\hbar^3} \int dp p^2 f_p R(p) = G_V \frac{n}{2}. \tag{B28}$$

The functions pertaining to the saddle-point calculation of G_V are

$$g_V(p) = R(p), \quad f_V(p) = \frac{p^2}{2mT} - 2\ln p, \quad p_V = (2mT)^{1/2}. \tag{B29}$$

Strictly speaking, one should use $f_V = -\ln(p^2 f_p)$ and p_V as in Eq. (B2), although at the expense of simplicity.

With complete expressions for τ and V, the total energy density is acquired from

$$\varepsilon = \frac{\tau}{2m} + \mathcal{H}_d + V, \tag{B30}$$

where $\mathcal{H}_d$ is given by Eq. (24).

The entropy density in this scheme is obtained from Eq. (14) which, upon Taylor expansion about $z = 0$, yields

$$s = \frac{-g}{2\pi^2\hbar^3} \int dp p^2 \left[z e^{-\frac{p^2}{2mT} - \frac{R}{T}} \left(-1 - \frac{p^2}{2mT} - \frac{R}{T} + \ln z\right) - z^2 e^{-\frac{p^2}{mT} - \frac{2R}{T}} \left(-\frac{1}{2} - \frac{p^2}{2mT} - \frac{R}{T} + \ln z\right)\right] \tag{B31}$$
$$= \frac{\tau}{2mT} + \frac{2V}{T} - n\ln z + \frac{g}{2\pi^2\hbar^3} \left(z \int dp e^{-\frac{R}{T}} e^{-\frac{p^2}{2mT} + 2\ln p} - \frac{z^2}{2} \int dp e^{-\frac{2R}{T}} e^{-\frac{p^2}{mT} + 2\ln p}\right) \tag{B32}$$
$$= \frac{\tau}{2mT} + \frac{2V}{T} - n\ln z + zgG_{n1} n_Q - \frac{z^2}{2^{5/2}} g G_{n2} n_Q \tag{B33}$$
$$= \frac{\tau}{2mT} + \frac{2V}{T} - n\ln z + n\left[1 + \frac{n}{2^{5/2}} \left(\frac{n}{G_{n1} g n_Q}\right) \frac{G_{n2}}{G_{n1}}\right]. \tag{B34}$$

The pressure is given by the thermodynamic identity

$$P = -\varepsilon + Ts + \mu n \tag{B35}$$

and the specific heats by

$$C_V = \frac{1}{n} \frac{\partial \varepsilon}{\partial T}\bigg|_n, \tag{B36}$$
$$C_P = C_V + \frac{T}{n^2} \frac{\left(\frac{\partial P}{\partial T}\big|_n\right)^2}{\frac{\partial P}{\partial n}\big|_T}. \tag{B37}$$

We point out that, besides the usual practice of going to higher powers of z in n and τ, the accuracy of this procedure can be improved by calculating $R(p)$ to $O(\beta^{-1})$ in the saddle-point approximation and by using a beyond-leading-order p_V in the determination of V.

APPENDIX C: SPECIFIC HEATS

1. Finite range models

The main difficulty in calculating C_V and C_P in the MDI model arises from the quantity $R(p)$, which is both density- and momentum-dependent. Hence, it cannot be absorbed in the chemical potential. To make this statement explicit, consider the spectrum of a single species in the MDI model,

$$\epsilon_p = \frac{p^2}{2m} + U(n,p) = \frac{p^2}{2m} + R(p) + u(n), \tag{C1}$$

where

$$R(p) = \frac{C}{n_0} \frac{\Lambda^2}{2\pi^2\hbar^3} \frac{1}{p} \int dp' p' \ln\left[\frac{\Lambda^2 + (p+p')^2}{\Lambda^2 + (p-p')^2}\right] f', \tag{C2}$$
$$C = \begin{cases} C_l & \text{for PNM,} \\ C_l + C_u & \text{for SNM,} \end{cases} \tag{C3}$$
$$u(n) = \begin{cases} \frac{(A_1+A_2)}{n_0} n + \frac{B(1-y)}{n_0^\sigma} n^\sigma & \text{for PNM,} \\ \frac{A_1}{n_0} n + \frac{B}{n_0^\sigma} n^\sigma & \text{for SNM.} \end{cases} \tag{C4}$$

The last term in Eq. (C1) has no momentum dependence and can be subsumed in the chemical potential for purposes of integrating over momentum. However, $R(p)$ cannot be treated the same way and so the "reduced" spectrum

$$\varepsilon_p = \frac{p^2}{2m} + R(p) \tag{C5}$$

is implicitly density-dependent, causing complications when one attempts to take derivatives with respect to μ and T because now the Fermi-Dirac distribution is

$$f = \frac{1}{1 + \exp\left[\frac{\frac{p^2}{2m} + R(p,\mu,T) - \mu}{T}\right]}, \tag{C6}$$

and, therefore,

$$\left.\frac{\partial f}{\partial \mu}\right|_T = \left.\frac{\partial f}{\partial \mu}\right|_{R,T} + \left.\frac{\partial f}{\partial R}\right|_{\mu,T}\left.\frac{\partial R}{\partial \mu}\right|_T \tag{C7}$$

$$= \frac{1}{T} f(1-f)\left(1 - \left.\frac{\partial R}{\partial \mu}\right|_T\right), \tag{C8}$$

$$\left.\frac{\partial f}{\partial T}\right|_\mu = \left.\frac{\partial f}{\partial T}\right|_{R,\mu} + \left.\frac{\partial f}{\partial R}\right|_{\mu,T}\left.\frac{\partial R}{\partial T}\right|_\mu \tag{C9}$$

$$= \frac{1}{T} f(1-f)\left[\ln\left(\frac{1-f}{f}\right) - \left.\frac{\partial R}{\partial T}\right|_\mu\right]. \tag{C10}$$

We obtain $\partial R/\partial\mu|_T$ and $\partial R/\partial T|_\mu$ by taking derivatives of Eq. (C2) with respect to the appropriate variables:

$$\left.\frac{\partial R}{\partial \mu}\right|_T = \frac{C}{n_0}\frac{\Lambda^2}{2\pi^2\hbar^3}\frac{1}{Tp}\int dp' p' \ln\left[\frac{\Lambda^2+(p+p')^2}{\Lambda^2+(p-p')^2}\right] \times f'(1-f')\left(1 - \left.\frac{\partial R'}{\partial \mu}\right|_T\right), \tag{C11}$$

$$\left.\frac{\partial R}{\partial T}\right|_\mu = \frac{C}{n_0}\frac{\Lambda^2}{2\pi^2\hbar^3}\frac{1}{Tp}\int dp' p' \ln\left[\frac{\Lambda^2+(p+p')^2}{\Lambda^2+(p-p')^2}\right] \times f'(1-f')\left[\ln\left(\frac{1-f'}{f'}\right) - \left.\frac{\partial R'}{\partial T}\right|_\mu\right], \tag{C12}$$

where Eqs. (C8)–(C10) have been used for $\partial f/\partial\mu|_T$ and $\partial f/\partial T|_\mu$.

Because $\partial R'/\partial\mu|_T$ and $\partial R'/\partial T|_\mu$ are momentum dependent, they cannot be taken out of the integrals. We must therefore solve Eqs. (C11) and (C12) self-consistently in a manner similar to the one used to compute R itself.

Equations (C8)–(C12) are the necessary ingredients for calculating the derivatives (with respect to μ and T) of the kinetic energy density τ and the number density n:

$$\left.\frac{\partial n}{\partial \mu}\right|_T = \frac{g}{2\pi^2\hbar^3}\int dp p^2 \left.\frac{\partial f}{\partial \mu}\right|_T, \tag{C13}$$

$$\left.\frac{\partial n}{\partial T}\right|_\mu = \frac{g}{2\pi^2\hbar^3}\int dp p^2 \left.\frac{\partial f}{\partial T}\right|_\mu, \tag{C14}$$

$$\left.\frac{\partial \tau}{\partial \mu}\right|_T = \frac{g}{2\pi^2\hbar^3}\int dp p^4 \left.\frac{\partial f}{\partial \mu}\right|_T, \tag{C15}$$

$$\left.\frac{\partial \tau}{\partial T}\right|_\mu = \frac{g}{2\pi^2\hbar^3}\int dp p^4 \left.\frac{\partial f}{\partial T}\right|_\mu. \tag{C16}$$

Here $\partial f/\partial\mu|_T$ and $\partial f/\partial T|_\mu$ are given by Eqs. (C8)–(C10) in which $\partial R/\partial\mu|_T$ and $\partial R/\partial T|_\mu$ are the self-consistent solutions of Eqs. (C11) and (C12). We also define the double integrals (pertaining to the finite range terms of MDI)

$$I_1 \equiv \frac{g}{8\pi^4\hbar^6}\iint dp dp' pp' \ln\left[\frac{\Lambda^2+(p+p')^2}{\Lambda^2+(p-p')^2}\right] ff', \tag{C17}$$

$$I_2 \equiv \frac{g}{\pi^4\hbar^6}\iint dp dp' p^2 p'^2 \times \frac{(\Lambda^2 - p^2 + p'^2)}{[\Lambda^2+(p+p')^2][\Lambda^2+(p-p')^2]} ff', \tag{C18}$$

for the derivatives of which similar considerations hold:

$$\left.\frac{\partial I_1}{\partial \mu}\right|_T = \frac{g}{4\pi^4\hbar^6}\iint dp dp' pp' \times \ln\left[\frac{\Lambda^2+(p+p')^2}{\Lambda^2+(p-p')^2}\right] f' \left.\frac{\partial f}{\partial \mu}\right|_T, \tag{C19}$$

$$\left.\frac{\partial I_1}{\partial T}\right|_\mu = \frac{g}{4\pi^4\hbar^6}\iint dp dp' pp' \times \ln\left[\frac{\Lambda^2+(p+p')^2}{\Lambda^2+(p-p')^2}\right] f' \left.\frac{\partial f}{\partial T}\right|_\mu, \tag{C20}$$

$$\left.\frac{\partial I_2}{\partial \mu}\right|_T = \frac{2g}{\pi^4\hbar^6}\iint dp dp' p^2 p'^2 \times \frac{(\Lambda^2 - p^2 + p'^2)}{[\Lambda^2+(p+p')^2][\Lambda^2+(p-p')^2]} f' \left.\frac{\partial f}{\partial \mu}\right|_T, \tag{C21}$$

$$\left.\frac{\partial I_2}{\partial T}\right|_\mu = \frac{2g}{\pi^4\hbar^6}\iint dp dp' p^2 p'^2 \times \frac{(\Lambda^2 - p^2 + p'^2)}{[\Lambda^2+(p+p')^2][\Lambda^2+(p-p')^2]} f' \left.\frac{\partial f}{\partial T}\right|_\mu. \tag{C22}$$

Note that a factor of 2 is gained in Eqs. (C19)–(C22) due to the interchangeability of f and f'.

For the specific heat at constant volume, we use

$$C_V = \left.\frac{\partial E}{\partial T}\right|_n = \frac{1}{n}\left.\frac{\partial \varepsilon}{\partial T}\right|_\mu \tag{C23}$$

$$= \frac{1}{n}\left(\left.\frac{\partial \varepsilon}{\partial T}\right|_\mu - \frac{\left.\frac{\partial \varepsilon}{\partial \mu}\right|_T \left.\frac{\partial n}{\partial T}\right|_\mu}{\left.\frac{\partial n}{\partial \mu}\right|_T}\right). \tag{C24}$$

With the aid of Eqs. (C4) and (C17), the energy density of MDI can be expressed as

$$\varepsilon = \frac{1}{2m}\tau + \int u(n) dn + \frac{C\Lambda^2}{n_0} I_1 \tag{C25}$$

and, therefore, its derivatives with respect to μ and T are given by

$$\left.\frac{\partial \varepsilon}{\partial \mu}\right|_T = \frac{1}{2m}\left.\frac{\partial \tau}{\partial \mu}\right|_T + u(n)\left.\frac{\partial n}{\partial \mu}\right|_T + \frac{C\Lambda^2}{n_0}\left.\frac{\partial I_1}{\partial \mu}\right|_T, \tag{C26}$$

$$\left.\frac{\partial \varepsilon}{\partial T}\right|_\mu = \frac{1}{2m}\left.\frac{\partial \tau}{\partial T}\right|_\mu + u(n)\left.\frac{\partial n}{\partial T}\right|_\mu + \frac{C\Lambda^2}{n_0}\left.\frac{\partial I_1}{\partial T}\right|_\mu, \tag{C27}$$

where Eqs. (C13)–(C16) and (C19) and (C20) are to be utilized. These relations provide a cross check of evaluating C_V in Eq. (C24) directly through appropriate tabulations of the ND expression for ϵ (see Appendix B) as a function of μ and T.

The specific heat at constant pressure is obtained from

$$C_P = C_V + \frac{T}{n^2}\frac{\left(\left.\frac{\partial P}{\partial T}\right|_n\right)^2}{\left.\frac{\partial P}{\partial n}\right|_T}, \tag{C28}$$

where [by means of a Jacobi transformation from (n,T) to (μ,T)]

$$\left.\frac{\partial P}{\partial T}\right|_n = \left.\frac{\partial P}{\partial T}\right|_\mu - \frac{\left.\frac{\partial P}{\partial \mu}\right|_T \left.\frac{\partial n}{\partial T}\right|_\mu}{\left.\frac{\partial n}{\partial \mu}\right|_T}, \tag{C29}$$

$$\left.\frac{\partial P}{\partial n}\right|_T = \frac{\left.\frac{\partial P}{\partial \mu}\right|_T}{\left.\frac{\partial n}{\partial \mu}\right|_T}. \tag{C30}$$

Starting from Eq. (17) and observing that

$$\frac{\partial U(n,p)}{\partial p} = \frac{\partial R}{\partial p} \tag{C31}$$

$$= -\frac{R}{p} + \frac{2C}{n_0}\frac{\Lambda^2}{\pi^2\hbar^3}\frac{1}{p}\int dp' p'^2 \times \frac{(\Lambda^2 - p^2 + p'^2)}{[\Lambda^2 + (p+p')^2][\Lambda^2 + (p-p')^2]} f', \tag{C32}$$

we can write the pressure as

$$P = \frac{1}{3m}\tau + \int u(n)dn + \frac{C\Lambda^2}{3n_0} I_1 + \frac{C\Lambda^2}{3n_0} I_2. \tag{C33}$$

Hence,

$$\left.\frac{\partial P}{\partial \mu}\right|_T = \frac{1}{3m}\left.\frac{\partial \tau}{\partial \mu}\right|_T + u(n)\left.\frac{\partial n}{\partial \mu}\right|_T + \frac{C\Lambda^2}{3n_0}\left.\frac{\partial I_1}{\partial \mu}\right|_T + \frac{C\Lambda^2}{3n_0}\left.\frac{\partial I_2}{\partial \mu}\right|_T, \tag{C34}$$

$$\left.\frac{\partial P}{\partial T}\right|_\mu = \frac{1}{3m}\left.\frac{\partial \tau}{\partial T}\right|_\mu + u(n)\left.\frac{\partial n}{\partial T}\right|_\mu + \frac{C\Lambda^2}{3n_0}\left.\frac{\partial I_1}{\partial T}\right|_\mu + \frac{C\Lambda^2}{3n_0}\left.\frac{\partial I_2}{\partial T}\right|_\mu. \tag{C35}$$

As with C_V, the derivatives above provide an alternate means to check the evaluation of C_P in Eq. (C28) directly through tabulations of the relevant quantities as functions of μ and T.

2. Zero range models

For a single-species Skyrme model with the spectrum

$$\epsilon_p = \frac{p^2}{2m} + Anp^2 + \frac{\partial \mathcal{H}_d}{\partial n}, \tag{C36}$$

we have

$$\left.\frac{\partial f}{\partial \mu}\right|_T = \frac{1}{T} f(1-f)\left(1 - Ap^2 \left.\frac{\partial n}{\partial \mu}\right|_T\right), \tag{C37}$$

$$\left.\frac{\partial f}{\partial T}\right|_\mu = \frac{1}{T} f(1-f)\left[\ln\left(\frac{1-f}{f}\right) - Ap^2 \left.\frac{\partial n}{\partial T}\right|_\mu\right], \tag{C38}$$

and thus

$$\left.\frac{\partial n}{\partial \mu}\right|_T = \frac{g}{2\pi^2\hbar^3}\int dp p^2 \frac{1}{T} f(1-f)\left(1 - Ap^2 \left.\frac{\partial n}{\partial \mu}\right|_T\right), \tag{C39}$$

$$\left.\frac{\partial n}{\partial T}\right|_\mu = \frac{g}{2\pi^2\hbar^3}\int dp p^2 \frac{1}{T} f(1-f) \times\left[\ln\left(\frac{1-f}{f}\right) - Ap^2 \left.\frac{\partial n}{\partial T}\right|_\mu\right]. \tag{C40}$$

Collecting $\partial n/\partial\mu|_T$ and $\partial n/\partial T|_\mu$ to the left-hand side,

$$\left.\frac{\partial n}{\partial \mu}\right|_T = \frac{\frac{g}{2\pi^2\hbar^3}\frac{1}{T}\int dp p^2 f(1-f)}{1 + \frac{gA}{2\pi^2\hbar^3}\frac{1}{T}\int dp p^4 f(1-f)}, \tag{C41}$$

$$\left.\frac{\partial n}{\partial T}\right|_\mu = \frac{\frac{g}{2\pi^2\hbar^3}\frac{1}{T}\int dp p^2 f(1-f)\ln\left(\frac{1-f}{f}\right)}{1 + \frac{gA}{2\pi^2\hbar^3}\frac{1}{T}\int dp p^4 f(1-f)}. \tag{C42}$$

With the μ and T derivatives of f and n completely determined, the same can be done for τ and consequently for ε, P, and the specific heats. The results are identical to those obtained using the method we used in Ref. [71].

[1] J. M. Lattimer and F. D. Swesty, Nucl. Phys. A **535**, 331 (1991).
[2] H. Shen, H. Toki, K. Oyamatsu, and K. Sumiyoshi, Nucl. Phys. A **637**, 435 (1998).
[3] G. Shen, C. J. Horowitz, and S. Teige, Phys. Rev. C **83**, 035802 (2011).
[4] G. Shen, C. J. Horowitz, and E. O'Connor, Phys. Rev. C **83**, 065808 (2011).
[5] A. W. Steiner, M. Hempel, and T. Fischer, Astrophys. J. **774**, 17 (2013).
[6] M. Hempel and J. Schaffner-Bielich, Nucl. Phys. A **837**, 210 (2010).
[7] F. D. Swesty, J. M. Lattimer, and E. S. Myra, Astrophys. J. **425**, 195 (1994).
[8] E. O'Connor and C. D. Ott, Astrophys. J. **730**, 70 (2011).
[9] K. Sumiyoshi, S. Yamada, and H. Suzuki, Astrophys. J. **667**, 382 (2007).
[10] M. Hempel, T. Fischer, J. Schaffner-Bielich, and M. Liebendörfer, Astrophys. J. **748**, 70 (2012).
[11] G. F. Bertsch and S. Das Gupta, Phys. Rep. **160**, 189 (1988).
[12] P. Danielewicz and G. Odyniec, Phys. Lett. B **157**, 146 (1985).
[13] H. A. Gustafsson *et al.*, Phys. Rev. Lett. **52**, 1590 (1984).
[14] G. M. Welke, M. Prakash, T. T. S. Kuo, S. Das Gupta, and C. Gale, Phys. Rev. C **38**, 2101 (1988).
[15] P. J. Siemens and J. O. Rasmussen, Phys. Rev. Lett. **42**, 880 (1979).
[16] C. Gale, G. Bertsch, and S. Das Gupta, Phys. Rev. C **35**, 1666 (1987).
[17] M. Prakash, T. T. S. Kuo, and S. Das Gupta, Phys. Rev. C **37**, 2253 (1988).
[18] C. Gale, G. M. Welke, M. Prakash, S. J. Lee, and S. Das Gupta, Phys. Rev. C **41**, 1545 (1990).
[19] P. Danielewicz, Nucl. Phys. A **673**, 375 (2000).
[20] P. Danielewicz, Acta Phys. Pol. B **33**, 45 (2002).
[21] D. H. Youngblood, H. L. Clark, and Y.-W. Lui, Phys. Rev. Lett. **82**, 691 (1999).

[22] U. Garg, Nucl. Phys. A **731**, 3 (2004).
[23] G. Colò, N. V. Giai, J. Meyer, K. Bennaceur, and P. Bonche, Phys. Rev. C **70**, 024307 (2004).
[24] P. Danielewicz, R. Lacey, and W. G. Lynch, Science **298**, 1592 (2002).
[25] C. B. Das, S. Das Gupta, and C. Gale, and B.-A. Li, Phys. Rev. C **67**, 034611 (2003).
[26] H.-Y. Kong, Y. Xia, L.-W. Chen, B.-A. Li, and Y.-G. Ma, Phys. Rev. C **91**, 047601 (2015).
[27] B.-A. Li, C. B. Das, S. Das Gupta, and C. Gale, Nucl. Phys. A **735**, 563 (2004).
[28] M. Prakash, I. Bombaci, M. Prakash, P. J. Ellis, and J. M. Lattimer, Phys. Rep. **280**, 1 (1997).
[29] P. B. Demorest, T. Pennucci, S. M. Ransom, M. S. E. Roberts, and J. W. T. Hessels, Nature (London) **467**, 1081 (2010).
[30] J. Antoniadis *et al.*, Science **340**, 6131 (2013).
[31] J. M. Lattimer and M. Prakash, in *From Nuclei to Neutron Stars* (World Scientific, Singapore, 2011), p. 275.
[32] A. W. Steiner, J. M. Lattimer, and E. F. Brown, Astrophys. J. **722**, 33 (2010).
[33] A. W. Steiner, J. M. Lattimer, and E. F. Brown, Astrophys. J. Lett. **765**, L5 (2013).
[34] J. M. Lattimer, Annu. Rev. Nucl. Part. Sci. **62**, 488 (2012).
[35] M. Jaminon, C. Mahaux, and P. Rochus, Nucl. Phys. A **365**, 371 (1981).
[36] T. L. Ainsworth, E. Baron, G. E. Brown, J. Cooperstein, and M. Prakash, Nucl. Phys. A **464**, 740 (1987).
[37] S. Hama, B. C. Clark, E. D. Cooper, H. S. Sherif, and R. L. Mercer, Phys. Rev. C **41**, 2737 (1990).
[38] E. D. Cooper, S. Hama, B. C. Clark, and R. L. Mercer, Phys. Rev. C **47**, 297 (1993).
[39] J. Decharge and D. Gogny, Phys. Rev. C **21**, 1568 (1980).
[40] T. Gaitanos and M. Kaskulov, Nucl. Phys. A **899**, 33 (2013).
[41] X. Zhang and M. Prakash (unpublished).
[42] P.-G. Reinhard, D. J. Dean, W. Nazarewicz, J. Dobaczewski, J. A. Maruhn, and M. R. Strayer, Phys. Rev. C **60**, 014316 (1999).
[43] W. Zuo, U. Lombardo, H.-J. Schulze, and Z. H. Li, Phys. Rev. C **74**, 014317 (2006).
[44] P. Gögelein, E. N. E. van Dalen, K. Gad, K. S. A. Hassaneen, and H. Müther, Phys. Rev. C **79**, 024308 (2009).
[45] B.-A. Li and X. Han, Phys. Lett. B **727**, 276 (2013).
[46] S. Chakraborty, B. Sahoo, and S. Sahoo, Phys. At. Nucl. **78**, 43 (2015).
[47] N. Vinh Mau and D. Vautherin, Nucl. Phys. A **445**, 245 (1985).
[48] T. von Egidy and D. Bucurescu, Phys. Rev. C **72**, 044311 (2005).
[49] J. W. Negele and K. Yazaki, Phys. Rev. Lett. **47**, 71 (1981).
[50] S. Fantoni, B. L. Friman, and V. R. Pandharipande, Phys. Lett. B **104**, 89 (1981).
[51] M. Prakash, J. Wambach, and Z. Ma, Phys. Lett. B **128**, 141 (1983).
[52] C. Mahaux, P. F. Bortignon, R. A. Broglia, and C. H. Dasso, Phys. Rep. **120**, 1 (1985).
[53] C. Mahaux and R. Sartor, Adv. Nucl. Phys. **20**, 1 (1991).
[54] J. M. Lattimer and A. Burrows, Astrophys. J. **307**, 178 (1986).
[55] A. Burrows, Astrophys. J. **334**, 891 (1988).
[56] J. M. Lattimer and M. Prakash, Phys. Rep. **442**, 109 (2007).
[57] L. Baiotti, B. Giacomazzo, and L. Rezzolla, Phys. Rev. D **78**, 084033 (2008).
[58] L. Rezzolla, L. Baiotti, B. Giacomazzo, D. Link, and J. Font, Classical Quantum Gravity **27**, 114105 (2010).
[59] Y. Sekiguchi, K. Kiuchi, K. Kyutoku, and M. Shibata, Phys. Rev. Lett. **107**, 051102 (2011).
[60] C. Cardall, M. Prakash, and J. M. Lattimer, Astrophys. J. **554**, 322 (2001).
[61] S. L. Shapiro, Astrophys. J. **544**, 397 (2000).
[62] I. A. Morrison, T. W. Baumgarte, and S. L. Shapiro, Astrophys. J. **610**, 941 (2004).
[63] J. D. Kaplan *et al.*, Astrophys. J. **790**, 19 (2014).
[64] H. Shen, H. Toki, K. Oyamatsu, and K. Sumiyoshi, Astrophys. J. **197**, 20 (2011).
[65] M. D. Duez, F. Foucart, L. E. Kidder, C. D. Ott, and S. A. Teukolsky, Classical Quantum Gravity **27**, 114106 (2010).
[66] M. B. Deaton *et al.*, Astrophys. J. **776**, 47 (2013).
[67] B.-A. Li, C. B. Das, S. Das Gupta, and C. Gale, Phys. Rev. C **69**, 011603 (2004).
[68] J. Xu, L.-W. Chen, and B.-A. Li, Phys. Rev. C **91**, 014611 (2015).
[69] L. Landau and E. M. Lifshitz, *Statistical Physics*, 3rd ed., Part 1 (Pergamon, New York, 1980), Vol. 5.
[70] T. H. R. Skyrme, Nucl. Phys. **9**, 615 (1959).
[71] C. Constantinou, B. Muccioli, M. Prakash, and J. M. Lattimer, Phys. Rev. C **89**, 065802 (2014).
[72] B. D. Day, Rev. Mod. Phys. **50**(3), 495 (1978).
[73] D. F. Jackson, Rep. Prog. Phys. **37**, 55 (1974).
[74] W. D. Myers and W. J. Swiatecki, Nucl. Phys. **81**, 1 (1966).
[75] W. D. Myers and W. J. Swiatecki, Nucl. Phys. A **601**, 141 (1996).
[76] S. Shlomo, V. M. Kolomietz, and G. Colo, Eur. Phys. J. A **30**, 23 (2006).
[77] O. Bohigas, A. M. Lane, and J. Martorell, Phys. Rep. **51**, 267 (1979).
[78] H. Krivine, J. Treiner, and O. Bohigas, Nucl. Phys. A **336**, 155 (1980).
[79] J. M. Lattimer and Y. Lim, Astrophys. J. **771**, 51 (2013).
[80] M. B. Tsang *et al.*, Phys. Rev. C **86**, 015803 (2012).
[81] R. B. Wiringa, Phys. Rev. C **38**, 2967 (1988).
[82] W. Zuo, I. Bombaci, and U. Lombardo, Euro. Phys. J. A **50**, 1 (2014).
[83] A. Akmal, V. R. Pandharipande, and D. G. Ravenhall, Phys. Rev. C **58**, 1804 (1998).
[84] A. Akmal and V. R. Pandharipande, Phys. Rev. C **56**, 2261 (1997).
[85] Z.-Y. Ma, J. Rong, B.-Q. Chen, Z.-Y. Zhu, and H.-Q. Song, Phys. Lett. B **604**, 170 (2004).
[86] E. N. E. van Dalen, C. Fuchs, and A. Faessler, Phys. Rev. C **72**, 065803 (2005).
[87] F. Sammarruca, W. Barredo, and P. Krastev, Phys. Rev. C **71**, 064306 (2005).
[88] M. Baldo, G. F. Burgio, H.-J. Schulze, and G. Taranto, Phys. Rev. C **89**, 048801 (2014).
[89] J. M. Lattimer, C. J. Pethick, M. Prakash, and P. Haensel, Phys. Rev. Lett. **66**, 2701 (1991).
[90] C. Constantinou, Ph.D. thesis, Stony Brook University, 2013.
[91] E. M. Lifshitz and L. P. Pitaevskii, *Statistical Physics*, Part 2 (Butterworth Heinemann, Oxford, UK, 1980).
[92] G. Baym and C. Pethick, *Landau Fermi-Liquid Theory* (Wiley Interscience, New York, 1991).

[93] K. Hotokezaka, K. Kiuchi, K. Kyutoku, T. Muranushi, Y.-i. Sekiguchi, M. Shibata, and K. Taniguchi, Phys. Rev. D **88**, 044026 (2013).
[94] A. Bauswein, H.-T. Janka, and R. Oeschin, Phys. Rev. D **82**, 084043 (2010).
[95] H.-T. Janka, T. Zweger, and R. Monchmeyer, Astron. Astrophys. **268**, 360 (1993).
[96] A. F. Foucart, M. B. Deaton, M. D. Duez, E. O'Connor, C. D. Ott, R. Haas, L. E. Kidder, H. P. Pfeiffer, M. A. Scheel, and B. Szilagyi, Phys. Rev. D **90**, 024026 (2014).
[97] M. Prakash, T. L. Ainsworth, J. P. Blaizot, and H. Wolter, in *Windsurfing the Fermi Sea*, edited by T. T. S. Kuo and J. Speth (Elsevier, Amsterdam, 1987), Vol. II, p. 357.
[98] S. M. Johns, P. J. Ellis, and J. M. Lattimer, Astrophys. J. **473**, 1020 (1996).
[99] S. Weinberg, Astrophys. J. **168**, 175 (1971).
[100] J. Guichelaar, Physica (Amsterdam) **74**, 330 (1974).
[101] R. Butler, *Saddlepoint Approximations with Applications* (Cambridge University Press, Cambridge, UK, 2007).